

Directional Small-Angle X-ray Scattering Computed Tomography

RECONSTRUCTION OF THE LOCAL DIFFERENTIAL CROSS SECTION

Florian Schaff

May 2017

Supervisor:
Prof. Dr. Franz Pfeiffer

External Supervisor:
Prof. Dr. Martin Bech

TECHNISCHE UNIVERSITÄT MÜNCHEN
Physik Department
Lehrstuhl für Biomedizinische Physik

Directional Small-Angle X-ray Scattering Computed Tomography –

RECONSTRUCTION OF THE LOCAL DIFFERENTIAL CROSS SECTION

Florian Peter Schaff

Vollständiger Abdruck der von der Fakultät für Physik der Technischen Universität München zur Erlangung des akademischen Grades eines

Doktors der Naturwissenschaften (Dr. rer. nat.)

genehmigten Dissertation.

Vorsitzender: apl. Prof. Dr. Norbert Kaiser

Prüfer der Dissertation: 1. Prof. Dr. Franz Pfeiffer
2. Prof. Dr. Hendrik Dietz
3. Prof. Dr. Christian Schroer
(nur schriftliche Beurteilung)

Die Dissertation wurde am 23.05.2017 bei der Technischen Universität München eingereicht und durch die Fakultät für Physik am 07.02.2018 angenommen.

Abstract

The macroscopic properties of many objects are based on their internal nano- and microstructure. Investigating the nano- and microstructures inside a macroscopic object, however, remains a significant challenge. Imaging methods that create a direct image of these structures, e.g. X-ray computed tomography or electron microscopy, are restricted to a small field of view. To overcome this limitation, imaging methods based on X-ray scattering have emerged at synchrotron facilities. This is done by recording the local X-ray scattering signal at different points of an object. Especially small-angle X-ray scattering is used to characterize the nano- and microstructure inside an object without the need for high resolution imaging. Similarly, small-angle scattering-based X-ray imaging can be realized at conventional X-ray sources in the form of X-ray dark-field imaging with a grating interferometer. In both these methods, structural information is not directly related to the spatial resolution of the imaging system, and the local microstructure can, hence, be characterized with a large field of view. Additionally, given that X-rays penetrate matter, computed tomography can be used to reconstruct local scattering information inside a three-dimensional object.

The present thesis deals with the tomographic reconstruction of directional scattering information. In particular, the focus here is to reconstruct three-dimensional scattering distributions, from which structural orientations can be derived. The topic is covered for small-angle X-ray scattering at a synchrotron, as well as laboratory-based dark-field imaging. The thesis is structured into two parts accordingly. Firstly, a method for the reconstruction of directional small-angle X-ray scattering is presented. Directional computed tomography based on dark-field imaging is treated in the second part of the thesis.

Zusammenfassung

Die makroskopischen Eigenschaften vieler Objekte basieren auf deren interner Nano- und Mikrostruktur. Die Untersuchung der Nano- und Mikrostruktur in einem makroskopischen Objekt bleibt jedoch eine große Herausforderung. Bildgebende Verfahren, die ein direktes Bild dieser Strukturen erzeugen, z.B. Röntgen-Computertomographie oder Elektronenmikroskopie, sind auf ein kleines Sichtfeld beschränkt. Um diese Einschränkung zu überwinden, wurden an Synchrotron-Einrichtungen bildgebende Methoden auf der Grundlage von Röntgenstreuung entwickelt. Hierzu wird das lokale Röntgenstreusignal an verschiedenen Positionen eines Objektes aufgenommen. Insbesondere die Methode der Röntgenkleinwinkelstreuung ermöglicht somit die Charakterisierung der Nano- und Mikrostruktur innerhalb eines Objektes, ohne die Notwendigkeit hochauflösender Bildgebung. Ähnlich kann Röntgenbildgebung basierend auf Röntgenkleinwinkelstreuung mit Hilfe des Dunkelfeldsignals eines Gitterinterferometers auch mit konventionellen Röntgenröhren durchgeführt werden. Bei beiden Methoden hängt die ermittelte Strukturinformation nicht direkt mit der räumlichen Auflösung des bildgebenden Systems zusammen, und eine Charakterisierung der lokalen Mikrostruktur mit einem großen Sichtfeld ist somit möglich. Da Röntgenstrahlen Materie durchdringen, besteht außerdem die Möglichkeit mit Hilfe der Computertomographie lokale Streuinformationen innerhalb eines dreidimensionalen Objektes zu rekonstruieren.

Die vorliegende Arbeit behandelt die tomographische Rekonstruktion richtungsabhängiger Streusignale. Der Fokus liegt hierbei insbesondere darauf, dreidimensionale Streuverteilungen zu rekonstruieren, aus welchen Strukturorientierungen abgeleitet werden können. Das Thema wird sowohl für Röntgenkleinwinkelstreuung an einem Synchrotron, als auch für Röntgen-Dunkelfeld-Bildgebung mit konventionellen Röntgenröhren behandelt. Die Arbeit ist dementsprechend in zwei Teile gegliedert. Zunächst wird eine Methode zur Rekonstruktion richtungsabhängiger Röntgenkleinwinkelstreuung präsentiert. Der zweite Teil der Arbeit beschäftigt sich mit richtungsabhängiger Computertomographie basierend auf Dunkelfeld-Bildgebung.

Contents

1	Introduction	1
2	Fundamentals of X-rays	5
2.1	X-ray scattering and diffraction	7
2.1.1	Thomson scattering	7
2.1.2	Momentum transfer vector	8
2.2	Small-angle X-ray scattering	10
2.2.1	Spatial coherence	12
2.3	Refraction & absorption of X-rays	13
2.3.1	Refraction	13
2.3.2	Photoelectric absorption	14
2.4	Generation of X-rays	15
2.4.1	X-ray tubes	15
2.4.2	Synchrotron	16
3	Computed tomography	19
3.1	Filtered backprojection	20
3.2	Iterative reconstruction	21
3.3	Description of sample rotation by rotation matrices	22
3.3.1	Rotation in two dimensions	23
3.3.2	Rotation in three dimensions and Euler angles	25
4	Imaging with small-angle X-ray scattering	27
4.1	Small-angle X-ray scattering experiment	27
4.2	Local differential cross section	28
4.3	Scanning small-angle X-ray scattering	30
4.4	Orientation analysis using scanning SAXS	32
4.5	Three-dimensional scanning SAXS	32
4.6	Small-angle X-ray scattering computed tomography	33
4.6.1	Isotropic signal	35
4.6.2	Anisotropic signal and rotational invariance	36
4.6.3	Attenuation in SAXS-CT	38
4.7	Dimensionality of small-angle X-ray scattering imaging techniques	39

5	Six-dimensional small-angle X-ray scattering computed tomography	41
5.1	Experimental requirements for 6-D SAXS-CT	41
5.1.1	Effect of an additional axis of rotation	42
5.2	6-D SAXS-CT experiment	43
5.2.1	Tooth sample	43
5.2.2	Data acquisition	46
5.3	Data processing	47
5.3.1	Cropping & azimuthal integration	48
5.3.2	Summation of opposite scattering data	49
5.3.3	Attenuation normalization	50
5.4	Reconstruction of the local scattering cross section	52
5.4.1	Quantification of rotational invariance for conventional SAXS-CT	52
5.4.2	Virtual tomography axes	54
5.4.3	Quantification of rotational invariance for virtual tomography axes	57
5.5	Complete six-dimensional reconstruction	58
5.5.1	Reconstructed scattering orientations	58
5.5.2	Reconstructed radial segments	59
5.5.3	SART-TV reconstruction	60
5.6	Analysis of the reconstructed data	60
5.6.1	Consistency between reconstructed and measured data	60
5.6.2	Visualization of local cross sections	61
5.6.3	Extraction of collagen fibre orientation	63
5.7	Limitations of the method	66
5.7.1	Data acquisition	66
5.7.2	Resolution	66
5.7.3	Reconstruction	67
5.8	Discussion	67
6	Grating-based X-ray imaging	69
6.1	Talbot-Lau interferometer	69
6.1.1	G1 & Talbot-effect	71
6.1.2	G2 & phase-stepping	72
6.1.3	G0 & Lau-effect	73
6.2	Image extraction	74
6.2.1	Attenuation signal	75
6.2.2	Differential phase-contrast signal	76
6.2.3	Dark-field signal	76
6.3	Origin of the dark-field signal	77
6.3.1	Small-angle scattering in a grating interferometer	77
6.3.2	Full description of the dark-field signal	80

7	Non-iterative directional dark-field tomography	85
7.1	Rotational invariance of the dark-field signal	85
7.1.1	Experimental parameters	87
7.1.2	Comparison of horizontal and vertical grating alignment	87
7.2	Piecewise reconstruction of the anisotropic dark-field signal	89
7.2.1	Experimental realization	90
7.3	Comparison with X-ray tensor tomography	92
7.4	Extraction of fibre orientation	94
7.5	Discussion	94
8	Iterative directional dark-field tomography	97
8.1	Review of X-ray tensor tomography	97
8.1.1	Limitations of the XTT reconstruction	98
8.2	Anisotropic X-ray dark-field tomography	99
8.3	Data acquisition with an Eulerian cradle	101
8.3.1	Scattering-orientation specific acquisition schemes	102
8.3.2	Limitations of the Eulerian cradle and rotated gratings	103
8.4	Imaging of large, strongly scattering objects	105
8.4.1	Low-Sensitivity setup for directional dark-field tomography	106
8.4.2	Experimental parameters	108
8.4.3	Wood	109
8.4.4	Freeze-cast ceramics	110
8.5	Discussion	112
9	Conclusion	115
	Bibliography	129
	List of Figures	132
	List of Tables	133
	Abbreviations	135
	Constants	137
	Publications and scientific presentations	139
	Acknowledgements	143

The very first Nobel prize in physics was awarded to Wilhelm Conrad Röntgen in 1901 for his discovery of X-rays six years before [Nobel Prize, 1901]. Initially believed to be a new kind of radiation, it was later revealed that X-rays are high-energetic electromagnetic waves. Owing to their short wavelength and ability to penetrate matter, X-rays are used in a wide variety of areas, including the determination of molecular structures, medical imaging, or security applications. The stunning possibility to view the internal structure of objects in a non-destructive fashion makes imaging one of the most commonly known applications of X-rays. This is surprisingly simple: an object is placed in between an X-ray source and a detection device, and differences in the attenuation of X-rays at different positions of the object are used to create an image of the object. With the rise of digital computers, computed tomography (CT) was developed by Allan McLeod Cormack and Godfrey Hounsfield, for which they received the Nobel Prize in Physiology or Medicine in 1979 [Nobel Prize, 1979]. In CT, several X-ray images taken from different sides of an object are combined to offer a detailed internal view of the object. Whereas the spatial resolution in clinical CT is limited by the radiation dose delivered to a patient, other areas in which a non-destructive internal characterization of an object is required do not suffer from this restriction. At the time of writing, state-of-the-art CT machines are able to visualize structures sized in the range of a few μm . High resolution imaging, however, comes at the cost of only being able to investigate a limited field of view. As a consequence, it is a great challenge to characterize microscopic structures in macroscopic objects. Given that the macroscopic properties of objects are frequently correlated to their microstructure, there is a need for imaging techniques that provide access to the local nano- and microstructure in macroscopic objects.

Albeit substantially less pronounced, X-rays are subject to diffraction effects, just like visible light. Out of many different types of X-ray diffraction experiments, small-angle X-ray scattering (SAXS) is of particular interest here, as it allows to investigate structures sized up to several hundred nanometres that do not possess perfect crystalline order. Although SAXS experiments typically average over a large number of individual structures, information is retrieved without the need of direct resolution, as is the case in conventional X-ray imaging. Therefore, a hybrid imaging modality that maps spatial variations of the local scattering information can be used to overcome some of the limitations present in conventional X-ray imaging. A combination of SAXS with two-dimensional spatial resolution was realized towards the end of the last century [Fratzl, 1997; Rinnerthaler, 1999; Žižak, 2000; Kinney, 2001]. SAXS imaging have to be commonly performed with

1 Introduction

highly brilliant X-rays beams produced at synchrotron sources, owing to the stringent requirements on the used radiation. More recent developments have spawned grating-based dark-field imaging, an X-ray scattering-based imaging technique compatible with conventional X-ray tubes [Pfeiffer, 2008]. Although not identical, the origins of the dark-field signal are strongly linked to SAXS [Strobl, 2014; Prade, 2015b]. For both these methods, structural information is derived from X-ray scattering and therefore not related to spatial resolution. As a consequence, SAXS and dark-field imaging are particularly suitable for the investigation of structural changes on the nano- and micro-scale, spatially resolved over large areas.

Scattering-based imaging can also be combined with CT to obtain a three-dimensional distribution of the scattering signal inside an object. This has both been shown for SAXS [Schroer, 2006; Stribeck, 2006; Feldkamp, 2009; Jensen, 2011a; Jensen, 2011b], as well as for dark-field imaging [Wang, 2009; Bech, 2010; Revol, 2011; Lauridsen, 2014; Scholkmann, 2014; Hanneschläger, 2015]. In comparison with conventional, attenuation-based X-ray data, the information content of X-ray scattering data is much more detailed. One particular trait shared between SAXS- and dark-field-imaging is the possibility to investigate structural orientation from anisotropic scattering [Fratzl, 1997; Bunk, 2009; Jensen, 2010a; Jensen, 2010b]. Translated to CT this calls for reconstruction methods that yield three-dimensional structural orientation at each point of an object, rather than just a single value like conventional CT.

The work presented in this thesis deals with these multidimensional reconstructions of scattering data, based on both the SAXS- and dark-field signal. In mathematical terms, the goal of the SAXS-part is to reconstruct the local-scattering cross section $\left(\frac{d\sigma}{d\Omega}\right)(\mathbf{q}, \mathbf{r})$. It is a function that maps a single value to each combination of the three-dimensional real-space, and the three-dimensional reciprocal space:

$$\left(\frac{d\sigma}{d\Omega}\right)(\mathbf{q}, \mathbf{r}) : \quad \mathbb{R}^3 \times \mathbb{R}^3 \mapsto \mathbb{R}. \quad (1.1)$$

Similarly, the goal of all dark-field-based reconstructions is to reconstruct an orientation-dependent dark-field signal $df_{\text{rec}}(\epsilon, \mathbf{r})$ as a function of position \mathbf{r} and scattering orientation ϵ :

$$df_{\text{rec}}(\epsilon, \mathbf{r}) : \quad \mathbb{S}^2 \times \mathbb{R}^3 \mapsto \mathbb{R}. \quad (1.2)$$

For reasons that will be given in the appropriate chapters, $df_{\text{rec}}(\epsilon, \mathbf{r})$ can only be represented as a function on the two-sphere \mathbb{S}^2 spatially resolved in three-dimensional real-space. Whereas X-ray tensor tomography (XTT) was presented as the first realization

of such a directional CT for the dark-field signal just three years ago [Malecki, 2014b; Malecki, 2013], no reconstruction method that preserves oriented scattering information exists for SAXS, yet. With this in mind, the two main goals of the work presented here can be stated as:

- implementation of a six-dimensional SAXS-CT method that preserves oriented scattering information,
- further improvement and application of the XTT method for dark-field imaging.

Outline

The thesis is structured accordingly. Chapter 2 serves as an introduction to X-ray physics, mainly aimed at small-angle X-ray scattering. SAXS imaging is covered in the two subsequent chapters. An elaborate overview of several different SAXS imaging methods and their limitations is given in chapter 4. The development of a novel six-dimensional SAXS-CT method is treated in chapter 5. Results of a first six-dimensional SAXS-CT experiment are presented, showcasing the reconstruction of collagen fibre orientation within a tooth sample.

Grating-based X-ray imaging is introduced in chapter 6. The origin of the dark-field signal and its connection to SAXS are covered in detail. An adaptation of the main idea behind the SAXS-CT reconstruction method to dark-field imaging, which leads to a simplified approach to XTT is presented in chapter 7. Several improvements of the original XTT method, as well as imaging applications are discussed in chapter 8. Lastly, a conclusion of these results, as well as an outlook on potential future developments of X-ray scattering-based CT is given in chapter 9.

This chapter shall serve as a short introduction to X-ray physics with the goal to provide the reader with the theory essential for the results presented in the following. Owing to the scope of this thesis the main focus is on small-angle X-ray scattering. From the large number of textbooks covering the subject, this chapter follows mainly references [Warren, 1990; Guinier, 1955; AlsNielsen, 2011; Feigin, 1987; Glatter, 1982; Sivia, 2011]. Like many other known types of radiation, including e.g. radio waves, infra-red radiation and visible light, X-rays are electromagnetic waves. An overview of the electromagnetic spectrum is given in figure 2.1. X-rays are found at very short wavelengths in the order of $1 \text{ \AA} = 10^{-10} \text{ m}$. Their physical properties are therefore those of high energetic photons. The propagation speed of photons in vacuum is the speed of light $c = 2.998 \times 10^8 \text{ ms}^{-1}$. The energy of photons E is determined from their wavelength λ with Planck's constant $h = 4.136 \times 10^{-15} \text{ eVs}$ as:

$$E = \frac{hc}{\lambda}. \quad (2.1)$$

The energy of X-ray photons therefore is in the order of a few 10 kV. The wave nature of X-rays also suggests the use of wave-vectors \mathbf{k} to describe an X-ray wave. These vectors point in the propagation direction of X-rays with a magnitude k determined via their wavelength:

$$k = |\mathbf{k}| = \frac{2\pi}{\lambda}. \quad (2.2)$$

We will see in section 2.1.2 that wave-vectors allow for a very simple formulation of X-ray scattering.

The interaction between X-rays and matter is primarily to do with the electrons of atoms. Figure 2.2 gives an overview of the four most prominent interactions. For low energies, the predominant interactions are photoelectric absorption and elastic scattering. Both of

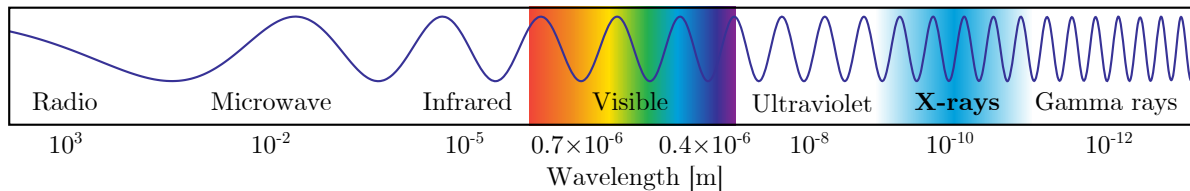


Figure 2.1: **X-rays in the electromagnetic spectrum.** X-rays are electromagnetic waves with wavelengths in the order of 10^{-10} m . Image adapted from https://en.wikipedia.org/wiki/electromagnetic_spectrum.

2 Fundamentals of X-rays

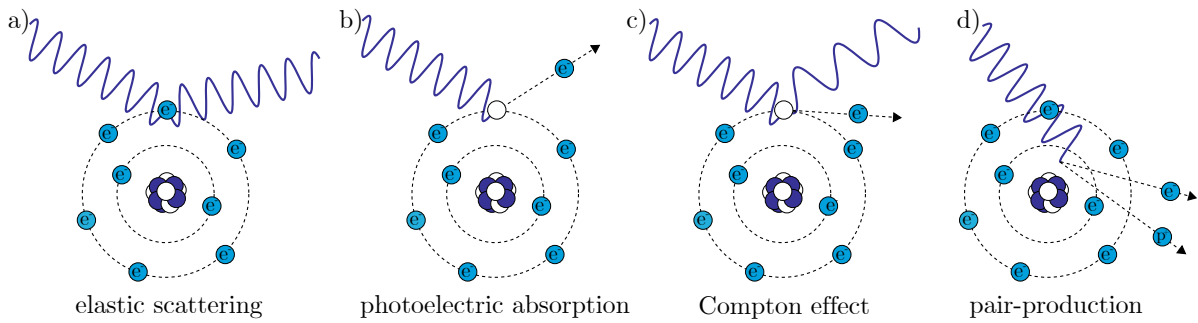


Figure 2.2: **The different interactions of X-ray photons with electrons.** a) Elastic scattering - also known as Thomson scattering: the photon is scattered from an electron without energy transfer. b) Photoelectric absorption: the photon is fully absorbed by an electron, which in turn is ejected from its atom. c) Compton effect: inelastic scattering of the photon by an electron. Part of the photon energy is transferred to the electron during the interaction. The wavelength of a Compton-scattered photon is therefore increased. d) Pair-production occurs in close proximity to the nucleus at photon energies higher than at least twice the electron rest energy. The entire energy of the photon is used to create an electron-positron pair.

them are covered in detail later in this chapter. As the photon energy increases, Compton scattering plays an increasing role while the importance of the former interactions declines. In contrast to its elastic counterpart, Compton scattering is the inelastic interaction of X-rays and electrons, with part of the X-rays energy transferred to the electron. After passing the threshold of 1.02 MeV, which is twice the electron rest energy of 511 keV, pair-production becomes the main source of interaction. All of the energy of a photon is converted into the mass of an electron-positron pair during this type of interaction. As all X-ray energies used during the work for this thesis were well below this threshold, pair-production is of no importance here.

The dominant interaction strongly depends on both the material and the X-ray energy. We will focus on elastic scattering and photoelectric absorption in the following sections. These interaction are dominant for the X-ray energies used for the work of this thesis.

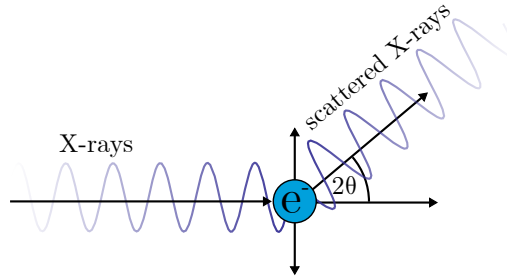


Figure 2.3: **Thomson scattering of X-rays by a single electron.** a) In the classical picture, X-rays are viewed as an electromagnetic wave that can drive an electron into oscillation. The electron in turn emits scattered radiation of the same wavelength as the incident X-rays. The angular distribution of the scattered intensity depends on the polarization of the incident radiation. For a polarized beam it is modified by a polarization factor equal to $1 + \cos^2 2\theta$ for scattering in, and a constant value of 1 for scattering out of the plane of polarization.

2.1 X-ray scattering and diffraction

As stated previously, scattering of X-rays by electrons without photon energy loss is called elastic scattering. The fundamental theory of this interaction is given in this section. Although a complete description requires quantum-mechanics, the model introduced with classical electromagnetism is sufficient for our purposes. An introduction to the quantum mechanical treatment can be found e.g. in [AlsNielsen, 2011, app. 5].

2.1.1 Thomson scattering

Let us first consider elastic scattering of X-rays by a single free electron, also known as Thomson scattering. The process is sketched in figure 2.3. In the classical picture, incident X-rays are viewed as an electromagnetic wave that interacts with an electron. During interaction the electron is accelerated by the alternating electric field of the wave and driven into oscillation. Given that charged particles emit radiation, the negatively charged electron acts as a source of radiation when accelerated by incident X-rays. The emitted waves are of the same frequency as the driving wave, i.e. the frequency of the X-ray wave. Thomson scattering is elastic and coherent, meaning there is no energy transfer to the electron [Glatter, 1982, p. 18][Sivia, 2011, p. 67]. The interaction probability for scattering processes is generally described by a cross section σ . For Thomson scattering, the total intensity scattered by a single electron is equal to the Thomson cross section σ_e :

$$\sigma_e = \frac{8}{3}\pi r_0^2 = 0.665 \times 10^{-24} \text{ cm}^2 ; r_0 = \frac{1}{4\pi\epsilon_0} \frac{e^2}{m_e c^2}. \quad (2.3)$$

2 Fundamentals of X-rays

Here, $r_0 = 2.818 \times 10^{-15}$ m is the so-called classical electron radius [AlsNielsen, 2011, p. 8]. It is calculated from the electric constant ϵ_0 , the elementary charge e , the electron mass m_e , and the speed of light c . Given its importance in Thomson scattering, r_0 is also known as the Thomson scattering length. Interestingly, in the classical picture σ_e does not depend on the energy of the incident X-rays. However, the very small value reveals that the interaction of X-rays with matter is very weak [Warren, 1990, p. 4].

Often times, the angular distribution of the scattered intensity is of interest rather than the absolute value. This can be described by a differential cross section $\left(\frac{d\sigma}{d\Omega}\right)$. For Thomson scattering by a single electron, the intensity scattered to a solid angle Ω depends on the apparent acceleration of the electron seen at an angle of observation 2θ [Warren, 1990, pp. 3-4]:

$$\left(\frac{d\sigma_e}{d\Omega}\right) = r_0^2 \left(\frac{1 + \cos^2 2\theta}{2}\right). \quad (2.4)$$

The term within brackets is the polarization factor, given here for unpolarized incident X-rays. For linearly polarized X-rays it changes to $\cos^2 2\theta$ and 1 for scattering angles in and out of the plane of polarization, respectively [AlsNielsen, 2011, p. 9].

2.1.2 Momentum transfer vector

During a real experiment we are not interested in scattering from a single electron, but from a very large number of electrons that make up matter. For this reason we will move on to X-ray scattering from several electrons in this section.

As there is no change in wavelength between incident and scattered radiation in Thomson scattering, waves scattered from different positions in space interfere. Let us consider every electron as the source of a secondary wave. The electromagnetic field seen at any point of detection is the result of interference between all secondary waves. Constructive or destructive interference occurs depending on the relative phases between all secondary waves. The intensity scattered in each direction is then given as the square of the resulting amplitude. We restrict ourselves to observation distances much greater than the distances between the scattering centres. This is known as the far-field limit, or Fraunhofer regime [AlsNielsen, 2011, p. 114]. It should be noted that a phase-shift of π between incident and scattered waves is introduced during a scattering event [AlsNielsen, 2011, p. 23]. This is owed to the fact that the frequencies of X-rays are much higher than the resonance frequencies of electrons. However, this phase-shift is the same for all scattered waves and we can safely ignore it for now [Warren, 1990, p. 4].

The most simple case is that of two electrons, A and B . This is illustrated in figure 2.4 a). An incident plane wave in the direction given by a unit vector \mathbf{s}_i is scattered by both electrons. The spatial arrangement of the electrons is given by the vector \mathbf{r} . In order to determine the scattered intensity in a direction given by the unit vector \mathbf{s}_f we need to know the phase relation $\Delta\Phi$ between the scattered waves. This phase difference arises

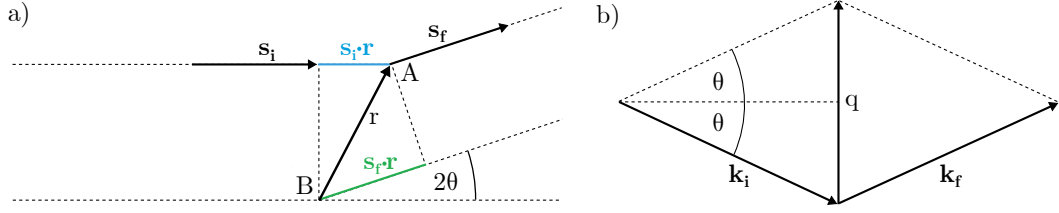


Figure 2.4: **Scattering and momentum transfer vector.** a) Scattering of a plane wave by two scattering centres A and B . The orientations of the incident and scattered waves are given by the unit vectors \mathbf{s}_i and \mathbf{s}_f , respectively. The magnitude of the scattered intensity is given by the relative phase between the waves scattered from both points. It depends on the path difference between the coloured parts. b) The momentum transfer vector \mathbf{q} is a convenient way to describe scattering phenomena. It is defined as the difference between the scattered and incident wavevector $\mathbf{k}_f - \mathbf{k}_i$.

from a path length difference Δs between the scattered beams. From simple geometry it is clear that only the coloured parts of each path are relevant for Δs . Their length can be readily calculated using the scalar product [Glatter, 1982, pp. 18-20]:

$$\Delta s = \mathbf{s}_f \cdot \mathbf{r} - \mathbf{s}_i \cdot \mathbf{r} = (\mathbf{s}_f - \mathbf{s}_i) \cdot \mathbf{r}. \quad (2.5)$$

As we are interested in the phase-difference $\Delta\Phi$ between both paths, we need to multiply Δs by $\frac{2\pi}{\lambda}$:

$$\Delta\Phi = \frac{2\pi}{\lambda}(\mathbf{s}_f - \mathbf{s}_i) \cdot \mathbf{r} = (\mathbf{k}_f - \mathbf{k}_i) \cdot \mathbf{r} = \mathbf{q} \cdot \mathbf{r}. \quad (2.6)$$

Here we described the incident and scattered waves by their respective wave-vectors \mathbf{k}_i and \mathbf{k}_f . These wave-vectors are obtained by scaling the previously used unit vectors \mathbf{s}_i and \mathbf{s}_f by the wave-number $\frac{2\pi}{\lambda}$ of the X-ray beam. For the case of elastic scattering the wavelength of the scattered radiation remains unchanged and both wave-vectors therefore have equal magnitude:

$$|\mathbf{k}_i| = |\mathbf{k}_f| = \frac{2\pi}{\lambda} = k. \quad (2.7)$$

Additionally, we introduced the momentum transfer vector \mathbf{q} as the difference between \mathbf{k}_f and \mathbf{k}_i . Its geometric construction is shown in figure 2.4 b). The momentum transfer vector simplifies the description of scattering processes greatly and is therefore also commonly known as scattering vector. In terms of the scattering angle 2θ its magnitude is given by:

$$q = |\mathbf{q}| = 2k \sin \theta = \frac{4\pi \sin \theta}{\lambda}. \quad (2.8)$$

2 Fundamentals of X-rays

From equation 2.6 it is clear that the use of scattering- and wave-vectors allows for a consolidated formulation of the problem. For a fixed wavelength - and hence wave-vector \mathbf{k} - there exists a reciprocal relation between \mathbf{q} and \mathbf{r} for constructive interference. Owing to this, scattering described by small momentum transfer vectors, i.e. small scattering angles, originates from structures large with respect to the X-ray wavelength [Guinier, 1955, pp. 2,4].

2.2 Small-angle X-ray scattering

To describe scattering from matter, an enormous number of electrons and their scattered waves need to be considered. Given that the work presented in this thesis exclusively deals with scattering at small angles $2\theta \ll 1^\circ$, several simplifications can be introduced here. First of all, a consequence of only considering scattering in the near-forward direction is that inelastic Compton scattering is comparatively weak and can be neglected [AlsNielsen, 2011, pp. 121-122]. Secondly, the polarization factor is approximately constant for small scattering angles. Within the small-angle approximation, $\left(\frac{d\sigma_e}{d\Omega}\right)$ therefore is independent of the scattering angle and proportional to r_0^2 [Feigin, 1987, p. 15][Feldkamp, 2011, p. 30]. In order to simplify further considerations we set $\left(\frac{d\sigma_e}{d\Omega}\right) \equiv 1$. If one is interested in quantitative results, the exact values of equation 2.4 can be reintroduced. Lastly, since the typical wavelength of X-rays used for scattering experiments is in the order of \AA , small angle scattering is insensitive to variations on atomic length-scales. From this follows that the intensity scattered by a single atom to small-angles only depends on the number of electrons, which is given by the atomic number Z [Feigin, 1987, p. 16]. The arrangement of individual electrons within an atom does not affect the scattering profile in the forward direction.

Our goal is to derive an expression for the scattered intensity as the sum of the waves originating from all electrons that make up matter. We will also make use of the single-scattering approximation, known as the first Born approximation, in which subsequent interactions of scattered waves are not considered [Feigin, 1987, p. 5]. This approximation is valid, owing to the weak interaction of X-rays with matter.

Given that atomic distances do not matter for small-angle scattering, it makes sense to employ the concept of electron density. In this picture, matter is seen as a continuous distribution of electrons that is described by an electron density function $\rho(\mathbf{r})$. The amplitude of the secondary wave emitted at a position \mathbf{r} therefore is proportional to the local electron density $\rho(\mathbf{r})$. Following the previous section, the total scattered amplitude $A(\mathbf{q})$ for a certain scattering vector \mathbf{q} is given as the superposition of all secondary waves. Hence we need to determine the relative phase for each secondary wave. Just like in the previous section, the phase for a secondary wave depends on the relative position inside the sample from which it originates and can be determined according to equation 2.6 as $\exp(i\mathbf{q} \cdot \mathbf{r})$. We use the exponential function to account for phase differences greater than 2π . Integration of $\rho(\mathbf{r})$ over the entire scattering volume V , weighted by the phase factor

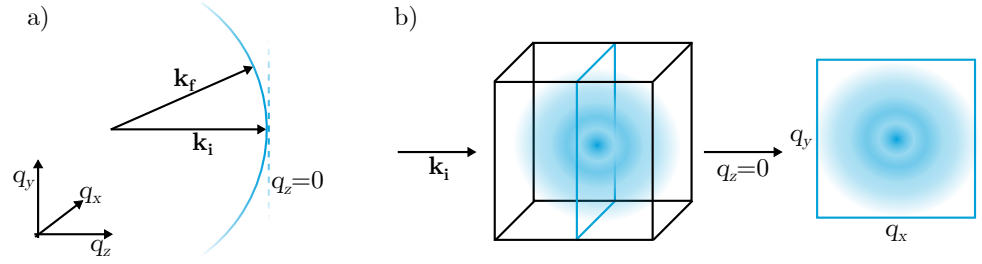


Figure 2.5: **Small-angle approximation.** a) For elastic scattering, only \mathbf{q} -vectors that end on a circle with radius k can be seen for a given \mathbf{k}_i . b) The curvature of the circle is negligible for small scattering angles and the two-dimensional slice of the reciprocal space perpendicular to \mathbf{k}_i is recorded in SAXS.

$\exp(i\mathbf{q} \cdot \mathbf{r})$, then yields $A(\mathbf{q})$ [Glatter, 1982, pp. 19-20]:

$$A(\mathbf{q}) = \int \rho(\mathbf{r}) e^{i\mathbf{q} \cdot \mathbf{r}} dV = \mathcal{F}(\rho(\mathbf{r})). \quad (2.9)$$

Mathematically, this integral resembles the Fourier transform of the electron density, $\mathcal{F}(\rho(\mathbf{r}))$. As only the scattered intensity $I_{\text{SAXS}}(\mathbf{q})$ can be measured in an experiment, the result of equation 2.9 has to be squared [Glatter, 1982, p. 19]:

$$I_{\text{SAXS}}(\mathbf{q}) = |A(\mathbf{q})|^2 = |\mathcal{F}(\rho(\mathbf{r}))|^2. \quad (2.10)$$

Equation 2.10 reveals an important result: the intensity distribution measured in the far-field resembles the square of the Fourier transform of the electron density distribution inside an object. Just like for a single electron, a microscopic differential cross section $\left(\frac{d\sigma}{d\Omega}\right)(\mathbf{q})$ can be used to describe the distribution of the scattered intensity:

$$I_{\text{SAXS}}(\mathbf{q}) \propto \left(\frac{d\sigma}{d\Omega}\right)(\mathbf{q}). \quad (2.11)$$

From the properties of Fourier transforms it follows that equal intensity is scattered to \mathbf{q} -vectors of opposite sign. This is also known as Friedel's law [AlsNielsen, 2011, p. 290]:

$$\left(\frac{d\sigma}{d\Omega}\right)(\mathbf{q}) = \left(\frac{d\sigma}{d\Omega}\right)(-\mathbf{q}). \quad (2.12)$$

When recording a single diffraction pattern, the incident radiation is fully described by the wave-vector \mathbf{k}_i . Both the direction and wavelength of the incident radiation are fixed. As there is no energy transfer in elastic scattering, only \mathbf{q} -vectors that end on a sphere with radius $|\mathbf{k}_f|$ give rise to elastic scattering. Figure 2.5 a) illustrates this fact. For the case of scattering to very small angles, the curvature of this sphere can be neglected. With the definition of \mathbf{k}_i along the z , and therefore q_z direction here, only \mathbf{q} -vectors with $q_z \ll q_x, q_y$ fall into the SAXS regime. From this follows that in the small-angle

2 Fundamentals of X-rays

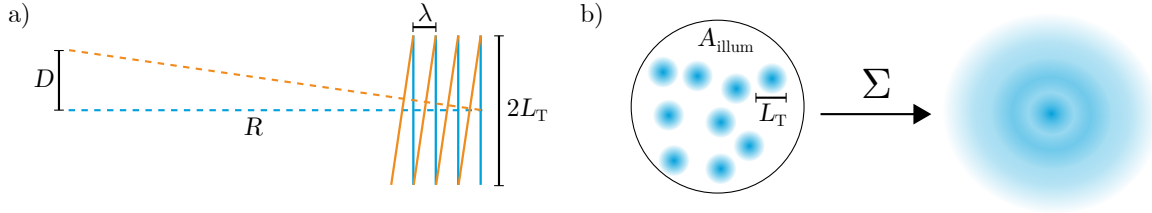


Figure 2.6: **Spatial coherence.** a) The spatial coherence length, L_T , can be calculated only from geometric parameters. For a source of size D and X-rays of wavelength λ it only depends on the distance away from the source R . b) In a typical small-angle X-ray scattering experiment, a corresponding coherence area πL_T^2 is much smaller than the area illuminated by the beam A_{illum} . The recorded SAXS signal therefore is the incoherent sum of the intensities of many diffraction patterns arising from difference coherence areas.

approximation $q_z = 0$, only \mathbf{q} -vectors in the slice perpendicular to \mathbf{k}_i are probed by a single SAXS measurement [AlsNielsen, 2011, p. 136][Paganin, 2006, p. 90]. The intensity of the SAXS pattern measured for $\mathbf{k}_i = (0, 0, k)$ therefore is a function of two variables: $I_{\text{SAXS}}(q_x, q_y, 0)$.

2.2.1 Spatial coherence

So far, we have assumed a perfect illumination. The derivations in section 2.1.2 require that the phase of the incident X-rays does not vary in the plane perpendicular to their propagation direction. This generally is not the case and a constant phase-relation between two points across the X-ray beam is only assured up to a certain distance between them. An X-ray beam can be characterized by its spatial - or transverse - coherence length, L_T . It is a measure of the distance between two points for which the phase of the X-ray beam varies by less than π . An illustration is given in figure 2.6 a). If the waves emitted by two distinct sources are exactly in phase at one point, L_T is defined as half the distance to the next point at which the waves are in phase again. The spatial coherence length depends on the wavelength λ of the X-rays, the size of the source, D , and the distance from the source, R . It can be calculated from these geometric parameters [AlsNielsen, 2011, pp. 25-27] as:

$$L_T = \frac{\lambda R}{2 D}. \quad (2.13)$$

The spatial coherence length therefore does not only depend on the X-ray beam, but rather the entire geometry of an experimental setup [Feldkamp, 2011, p. 32]. For a symmetric source we can define a coherence area as $A_{\text{coh}} = \pi L_T^2$. In the case of an asymmetric source, as is often the case for synchrotron sources, A_{coh} is asymmetric accordingly. The coherence area is the two dimensional analogue to the coherence length. For typical small-

2.3 Refraction & absorption of X-rays

angle X-ray scattering experiments, this area is very small compared to the size of the area illuminated by the X-ray beam A_{illum} [Feldkamp, 2011, pp. 61-64]:

$$A_{\text{illum}} \gg A_{\text{coh}}. \quad (2.14)$$

This is illustrated in figure 2.6 b). Even though there is no constant phase-relation over the entire illuminated area, each part of the beam is coherent in a small region defined by L_T . The diffracted intensity from one such coherence area corresponds to the Fourier transform of the electron density, as described by equation 2.10. In reality, the measured signal is the incoherent sum over a large number N of coherence volumes:

$$I_{\text{SAXS}}(\mathbf{q}) = \sum_{i=0}^N |A_{\text{coh},i}(\mathbf{q})|^2. \quad (2.15)$$

It is important to note that this sum is incoherent, i.e. the diffracted intensities from different coherence areas are summed rather than the amplitudes [Livet, 2007]. The measured SAXS signal therefore yields information about the spatially averaged structural information of the investigated volume.

2.3 Refraction & absorption of X-rays

The complex refractive index n is a useful tool to macroscopically describe the absorption and refraction of X-rays inside matter. It is material- and energy-dependent and consists of both a real and imaginary part:

$$n = 1 - \delta + i\beta. \quad (2.16)$$

2.3.1 Refraction

Just like for visible light, the refraction of X-rays is described by the real part of the refractive index, usually written as $1 - \delta$. On a microscopic level, refraction can be explained by Thomson scattering (cf. section 2.1.1). A derivation can be found in e.g. reference [AlsNielsen, 2011, pp. 71-75]. This connection can be seen in the definition of delta, which contains the Thomson scattering length r_0 :

$$\delta = \frac{2\pi\rho r_0}{k^2}. \quad (2.17)$$

The values of delta are of the order of $10^{-6} - 10^{-7}$ for hard X-rays in condensed matter [AlsNielsen, 2011, p.71]. Since δ is a positive quantity, the real part of the refractive index is less than one for X-rays, in contrast to visible light. This can be reasoned using the phase-shift of π introduced with Thomson scattering [Malecki, 2013, p. 6]. X-rays that travel through matter receive a phase-shift $\Delta\Phi$ with respect to travelling through vacuum.

2 Fundamentals of X-rays

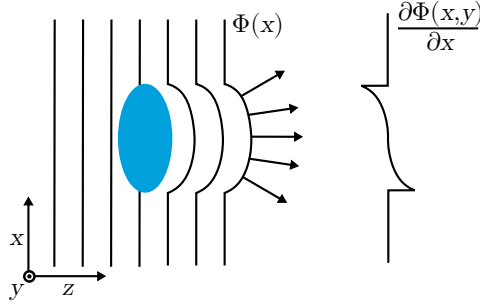


Figure 2.7: **X-ray refraction.** A plane wavefront is distorted when travelling through an object with inhomogeneous optical path thickness. The lines indicate wavefronts of equal phase. The refraction angle is proportional to the first derivative of the wavefront $\partial\Phi(x, y)/\partial x$.

This shift is calculated from the X-ray wavelength λ , the thickness d of the material and δ as:

$$\Delta\Phi = \frac{2\pi\delta d}{\lambda}. \quad (2.18)$$

An object of varying thickness or δ introduces a distortion to a previously plane wavefront, as depicted in figure 2.7. A curvature in the wave-front leads to refraction of the X-ray beam. The refraction angle α depends on the local gradient of the phase $\Phi(x, y)$ of the wave-front, evaluated perpendicular to the optical axis [Pfeiffer, 2006]. Here we set the x-direction to be perpendicular to the propagation direction of the X-rays, and the partial derivative along the x-axis is used accordingly:

$$\alpha = \frac{\lambda}{2\pi} \frac{\partial\Phi(x, y)}{\partial x}. \quad (2.19)$$

We recall that the wavelength of X-rays is in the order of \AA . The refraction angle depends on the wavelength and accordingly is very small for X-rays, in the order of a few microradians [Pfeiffer, 2006]. This makes the detection of X-ray refraction, and therefore phase-sensitive imaging, a non-trivial task. Over the years, several different methods for phase-imaging have been developed [Bech, 2009, pp. 3-6]. One of them is grating-based X-ray phase-contrast imaging. Its foundations are presented in chapter 6.

2.3.2 Photoelectric absorption

Let us move on to the imaginary part of the refractive index, $i\beta$. This term describes the attenuation of X-rays when passing through matter. While this includes photoelectric absorption, Compton scattering and pair-production, the former is the main process responsible for attenuation at low to moderate X-ray energies. The results presented in this thesis were all created with X-ray energies at which photoelectric absorption is dominant.

Photoelectric absorption is the process of an X-ray photon being absorbed by a bound electron from an atomic shell. A sketch of the interaction is given in figure 2.2 b). The photon is fully absorbed and its entire energy is transferred to the electron, which in turn is removed from its atom. The attenuation coefficient very strongly depends on the number of electrons, and therefore the atomic number Z . Whereas light elements are almost transparent for X-rays, those with high atomic number are highly absorbing. This is the reason that bones can be recognized so clearly in X-ray images, and soft tissue, which is weakly attenuating, is very hard to distinguish.

The attenuation of an X-ray beam with intensity I_0 when passing through matter of thickness d follows an exponential law, also known as the Lambert-Beer-law:

$$I(d) = I_0 \exp(-\mu d). \quad (2.20)$$

Here we used the attenuation coefficient μ , which is linked to β [AlsNielsen, 2011, p. 76]:

$$\mu = \frac{4\pi}{\lambda} \beta. \quad (2.21)$$

2.4 Generation of X-rays

There are several different ways to generate X-rays. The experiments presented in this thesis were conducted with X-rays generated by two different X-ray sources, namely a microfocus X-ray tube and a synchrotron undulator. Both of these sources are described here.

2.4.1 X-ray tubes

For medical imaging, security screening and industrial applications, X-rays are almost exclusively produced by X-ray tubes. Figure 2.8 shows a sketch of an X-ray tube. Although X-ray tubes come in a wide variety of implementations, the basic idea stays the same: electrons are created by a heated filament and accelerated towards a target using a strong electric field. When the electrons reach the target, which is typically made from a heavy element such as tungsten, they are decelerated and X-rays are emitted. If a small source spot, from which X-rays are emitted, is required, focussing coils that focus the electron beam onto the target can be included. Such microfocus X-ray tubes are able to reach focal spots no bigger than several μm^2 . The energies of X-rays generated in this way are distributed in a continuous spectrum, as can be seen in the example shown here. The highest energy of X-rays found in this so-called Bremsstrahlung is limited by the acceleration voltage. Additionally, there exist sharp peaks of high intensity for certain energies. These characteristic X-rays are produced when an outer-shell electron moves closer to the atomic core to fill a hole in one of the inner shells of the atom. The excess energy of the electron is released in the form of an X-ray photon in the process.

2 Fundamentals of X-rays

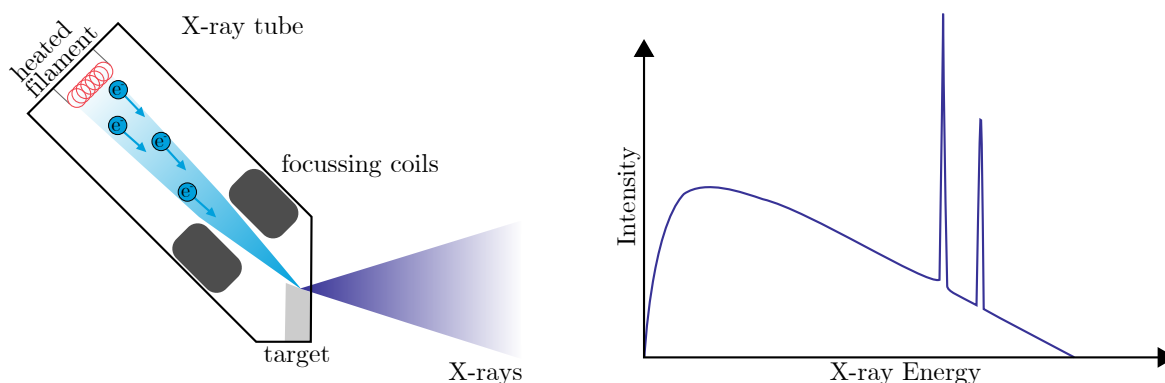


Figure 2.8: **X-ray tube.** Electrons are generated at a heated filament and accelerated in a high voltage electric field towards a target. The target is typically made out of a metal with high atomic number, e.g. tungsten. Upon hitting the target, the electrons are decelerated and X-rays are emitted. Some X-ray tubes use focussing coils to focus the electron beam onto a small impact area. The resulting intensity spectrum is shown to the right. It consists of a continuous Bremsstrahlung part and sharp characteristic peaks. The energy at which the characteristic peaks appear depends on the target material.

The energy levels found in an atom are unique to each element and the energy of the characteristic X-rays therefore depends on the target material. In the case of an X-ray tube, inner-shell vacancies are created when an accelerated electron strikes and ejects an electron from one of the inner shells.

2.4.2 Synchrotron

One of the major drawbacks of an X-ray tube is that the emitted radiation is polychromatic. If, for example, monochromatic radiation is required for an experiment, nearly all photons created by the X-ray tube have to be removed from the beam. An ideal X-ray source provides monochromatic radiation with very high intensity. From the demand for such X-ray sources, synchrotron light sources have emerged. A synchrotron is a large-scale electron-accelerator with the sole purpose of providing very intense beams of light. In a synchrotron, electrons accelerated to energies of a few GeV and forced onto a circular trajectory using strong bending magnets. The storage ring of a synchrotron often times has a circumference of several hundreds of meters. X-rays are created in a synchrotron either as bending magnet radiation from the strong radial acceleration used to keep them on track, or with specifically designed insertion devices. The latter are constructed around the path of the electron beam inside the storage ring in a straight section between bending magnets. We will focus on the radiation produced by an undulator insertion device here. An overview of an undulator is shown in figure 2.9. It consists of alternating strong magnetic fields that force the electrons inside the storage ring into rapid oscillation. This

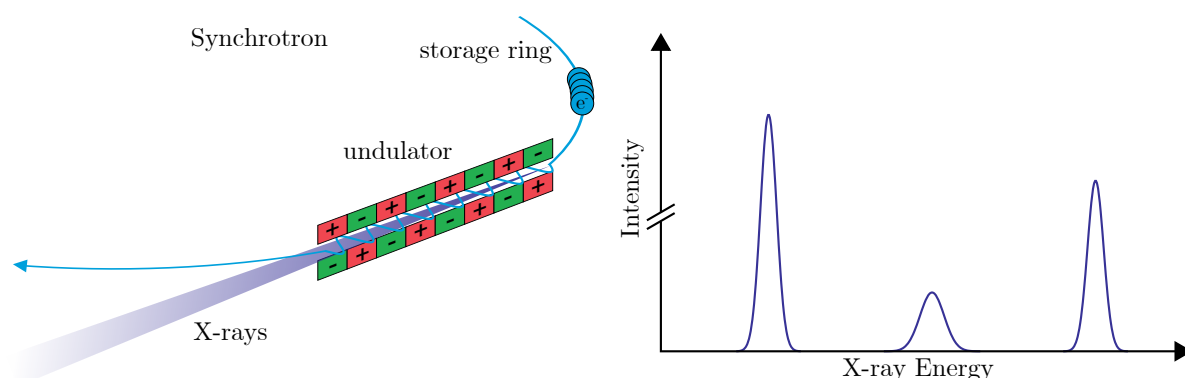


Figure 2.9: **Undulator at a synchrotron.** In a synchrotron, electrons travel inside a circular storage ring at nearly the speed of light. An undulator is an insertion device that is able to produce X-rays beams of very high quality. Alternating pairs of magnets force the electron beam into rapid oscillations. X-rays are generated in the process. The magnets are designed in such a way that the resulting spectrum consists of very sharp intensity peaks at defined X-ray energies. Note the X-ray flux provided by a synchrotron is much greater than that produced by an X-ray tube, and hence the spectrum can be filtered using a crystal monochromator and still leave sufficient flux for imaging.

lateral acceleration causes the electrons to emit X-rays. The magnetic fields in an undulator are designed in such a way that the emitted X-rays are concentrated in sharp peaks at specific energies. A typical undulator spectrum is sketched on the right. This allows the efficient use of monochromatic radiation. Furthermore, the X-ray flux generated by a synchrotron surpasses that of an X-ray tube by many orders of magnitude. A detailed overview over the generation of synchrotron radiation is found e.g. in the book by AlsNielsen and McMorrow [AlsNielsen, 2011, pp.33-60].

For the purpose of this thesis it is only important to outline that X-ray tubes are the essential source of X-rays for laboratory applications. All grating-interferometry experiments presented in chapters 7 and 8 were performed with a laboratory microfocus X-ray tube source. Experiments that require a very bright, monochromatic X-ray source have to often times be performed at a synchrotron. The SAXS experiments presented in chapter 5 were therefore performed with X-rays from an undulator source.

Tomography refers to imaging techniques that reconstruct the spatial distribution of a physical quantity inside an object. Although tomography is used in various different fields, X-ray computed tomography (CT) is the most widely known application. In conventional CT, the three-dimensional distribution of the attenuation coefficient μ inside an object is recovered from X-ray projection data. As this thesis is heavily based on CT, the basic principles are presented in this chapter.

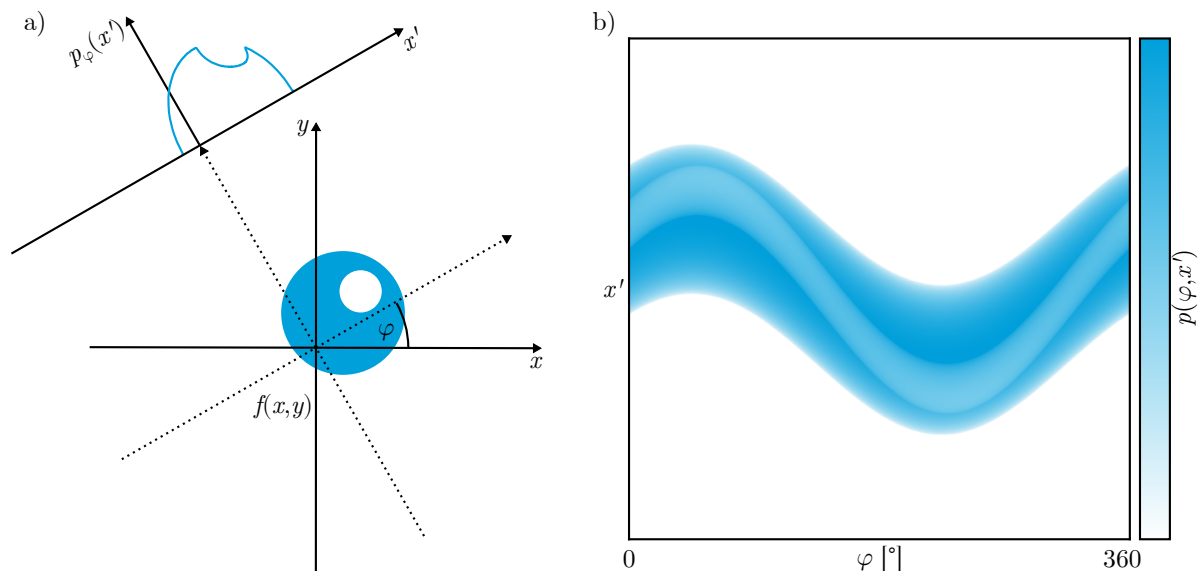


Figure 3.1: **X-ray projection.** a) The projection $p(\varphi, x')$ of an object function $f(x, y)$ is defined as line integrals under an angle φ . b) Sinogram of $f(x, y)$. Projection measurements $p(\varphi, x')$ for all possible φ are represented this way.

The goal in conventional X-ray CT is to obtain a value for μ at every position of an object. However, the mathematical description given here is not restricted to the reconstruction of μ alone, but rather any physical quantity that fits the model. For simplicity, let us consider a three-dimensional object as a stack of two-dimensional slices. A slice is described by an object function $f(x, y)$, which can be reconstructed independently from all other slices. During a standard CT measurement, projection data $p(\varphi, x')$ of $f(x, y)$ from various different rotations φ are recorded. The projection $p_\varphi(x')$ for a fixed angle φ is sketched in figure 3.1 a). The object in this example consists of a circle for which $f(x, y) = \text{const.}$,

3 Computed tomography

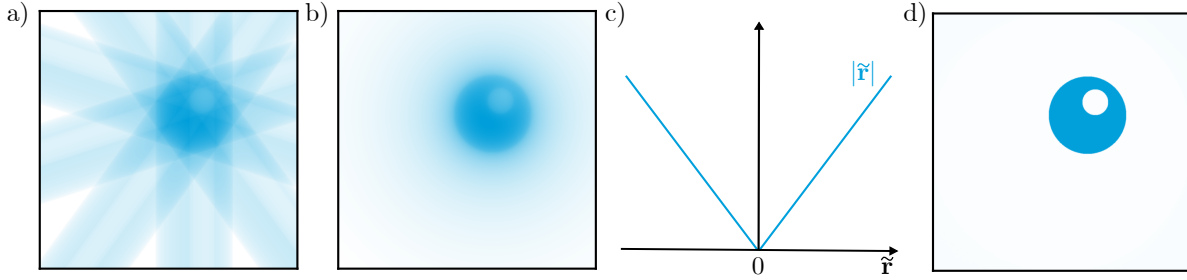


Figure 3.2: **Filtered backprojection.** a) The measured projections are projected back onto the image plane in order to create the reconstruction. Simple back-projection causes the image to appear blurred, as evident in b). c) A ramp filter applied in frequency space to the projections is necessary for a correct reconstruction, shown in d).

barring a circular hole. Outside the object, and inside the hole, $f(x, y) = 0$. Let us define a projection $p(\varphi, x')$ as the line integral of $f(x, y)$ along a path $L(\varphi, x')$:

$$p(\varphi, x') = \int_{L(\varphi, x')} f(x, y). \quad (3.1)$$

The one-dimensional function $p_\varphi(x')$ then resembles the collection of all line integrals with $\varphi = \text{const.}$. A two-dimensional image of $p(\varphi, x')$ is given in figure 3.1 b). Given the sinusoidal nature of the transformation, clearly visible in the image, $p(\varphi, x')$ is also often called the sinogram of $f(x, y)$. In an experiment, only $p(\varphi, x')$ is accessible and the task is to recover $f(x, y)$ from $p(\varphi, x')$.

3.1 Filtered backprojection

Filtered backprojection (FBP) is the most widely used method to reconstruct $f(x, y)$ from $p(\varphi, x')$ currently. It is based on the Fourier slice theorem which relates $p(\varphi, x')$ to the Fourier transform of $f(x, y)$ [AlsNielsen, 2011, pp. 309-310]. In \mathbb{R}^2 it states that

$$\mathcal{F}_1[p(\varphi = 0, x')] = \mathcal{F}_2[f(x, y)](\tilde{x}, \tilde{y} = 0). \quad (3.2)$$

Here, $p(\varphi = 0, x')$ is the parallel projection of $f(x, y)$ onto the y -axis, and the one- and two-dimensional Fourier transforms are denoted by \mathcal{F}_1 and \mathcal{F}_2 , respectively. The Fourier space variables corresponding to (x, y) are denoted as (\tilde{x}, \tilde{y}) .

For the reconstruction of $f(x, y)$ it is sufficient to know $\mathcal{F}_2[f(x, y)]$, as the Fourier transform can directly be inverted. From equation 3.2 it is clear that a one-dimensional slice through the origin of $\mathcal{F}_2(f)(\tilde{x}, \tilde{y})$ is probed for each $p_\varphi(x')$. Evidently, data from multiple $p(\varphi, x')$ can be combined to yield $\mathcal{F}_2(f)(\tilde{x}, \tilde{y})$, and therefore $f(x, y)$.

In practice the FBP reconstruction is performed as sketched in figure 3.2. Each $p(\varphi, x')$ is projected back onto the imaging plane along the axis from which it was measured, shown in a). Panel b) reveals that the reconstruction of such a simple backprojection is severely blurred. This is caused by a biased sampling towards low-frequencies and has to be accounted for. Precise mathematical treatment of the problem shows that a ramp-filter is required for the mathematically correct solution. Hence, a ramp-filter as shown in c) is applied to each $p(\varphi, x')$ in Fourier-space. Backprojection of the filtered $p(\varphi, x')$ leads to a correct reconstruction as seen in d).

FBP reconstruction poses several requirements to the recorded data. First of all, equiangular data over 180° or 360° must be provided. Secondly, the physical process of image generation needs to be linear. For X-ray attenuation imaging, which follows the exponential Lambert-Beer-law (cf. equation 2.20) this is achieved by taking the negative logarithm of the recorded data. Lastly, a sufficient amount of $p(\varphi, x')$ needs to be recorded in order to ensure an artefact-free reconstruction. If these requirements are met, FBP offers tomographic reconstruction at unrivalled computational efficiency. Owing to this, it is unsurprising that a large portion of CT-machines today rely on FBP reconstruction.

3.2 Iterative reconstruction

Next to the analytically correct solution based on the Fourier slice theorem, and its implementation in terms of FBP, tomographic reconstruction can also be performed using iterative methods. This offers greater flexibility, e.g. in the form of incorporating noise models or a priori knowledge into the reconstruction. This comes at the expense of greatly increased computational demands. Nonetheless, with the rapid improvement of computer hardware, iterative reconstruction methods have received increasing attention in recent years.

Let us sketch the basic idea of iterative reconstruction methods here. The tomographic measurement is understood as a system of linear equations. For this, the object volume is discretized into n voxels, whose values are contained in a single one-dimensional vector \mathbf{x} of length n . All projection measurements, i.e. the measured intensity values for each detector pixel and each rotation of the sample, are written as a vector \mathbf{p} of length m . Finally, an $m \times n$ system matrix \mathbf{M} that describes the complete imaging system is used to formulate the reconstruction as a matrix equation:

$$\mathbf{M}\mathbf{x} = \mathbf{p}. \quad (3.3)$$

The goal here is to find the \mathbf{x} that provides the best solution to equation 3.3. Although such a matrix equation is generally solvable using matrix inversion, the enormous size of \mathbf{M} renders this impossible in practice. Hence, iterative solvers have to be employed. Today, many different solvers exist and only the very basic idea is sketched in figure 3.3 here. From an initial estimate \mathbf{x}^i , a simulated measurement is calculated using \mathbf{M} , which

3 Computed tomography

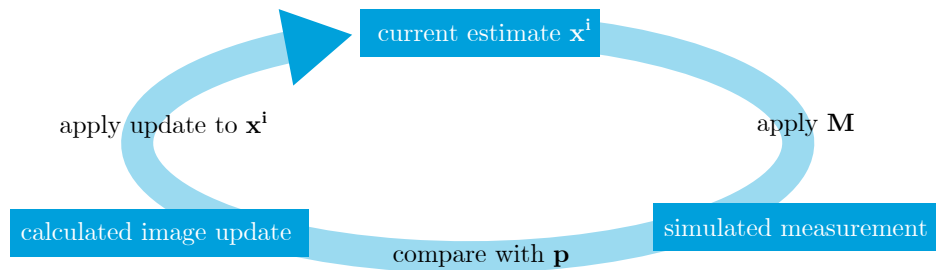


Figure 3.3: **Iterative reconstruction** The steps for one full iteration are shown. Starting with an estimate \mathbf{x}^i , the measurement is simulated by applying the system matrix \mathbf{M} . This simulated data is then compared to the measured data \mathbf{p} and an image update is applied to \mathbf{x}^i . This entire process is repeated until a satisfactory solution \mathbf{x} is found.

is known from the imaging geometry. This simulated measurement is then compared to the actual measured data \mathbf{p} and an image update is calculated from the differences. As a last step, this update is applied and an updated vector \mathbf{x}^{i+1} is obtained and used as initial estimate in the next iteration. This process is repeated until a certain criteria is met, e.g. a fixed amount of iterations is reached, or the image update is smaller than a certain threshold.

Although computationally more involved than FBP, iterative reconstruction serves as a powerful tool to deal with non-standard tomography problems. Hence, many results presented in this thesis were reconstructed using iterative methods. For example, the reconstruction presented in chapter 5 deals with undersampled and partially missing data, which made iterative reconstruction indispensable. Furthermore, the reconstruction method presented in chapter 8 was developed on the basis of iterative reconstruction.

3.3 Description of sample rotation by rotation matrices

Dealing with computed tomography naturally requires a way to describe the rotations between sample and imaging system that occur during a measurement. For conventional CT, this is fully done by using a single angle. However, we will see that the reconstruction methods presented in this thesis require additional rotations and a more complex description is therefore required.

Rotation matrices serve as backbone for the description of rotations in this thesis and hence are explained in more detail here. They are a mathematical tool to describe rotations in euclidean space.

3.3 Description of sample rotation by rotation matrices

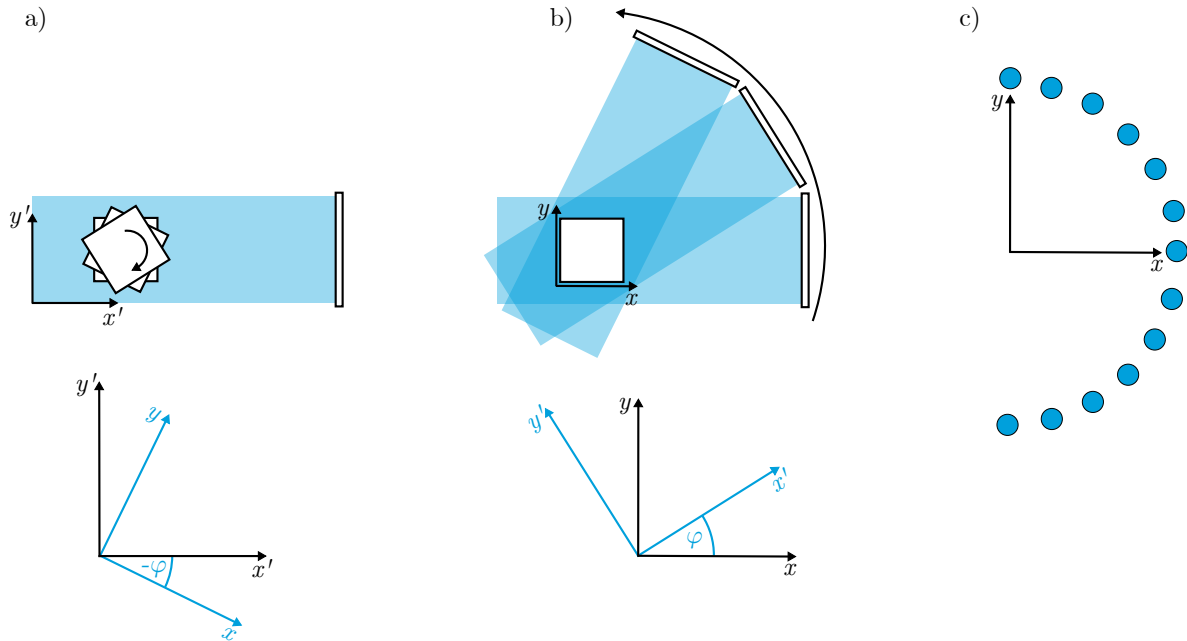


Figure 3.4: **Sample rotation in two dimensions.** During a CT measurement images are taken from different views of the sample. Either the imaging system (a), or the sample (b) can be considered stationary. Both views are equivalent. The rotations between the sample coordinate system (x, y) , and the laboratory coordinate system (x', y') are shown below. c) Schematic view of a CT measurement with 13 images. The sample is assumed to be at rest and in the centre of origin. Each point indicates a measurement from the respective orientation of the point with respect to the origin.

3.3.1 Rotation in two dimensions

Conventional CT experiments combine several two-dimensional images taken from different views of a sample to a three-dimensional dataset. This can be achieved in two ways, shown in figure 3.4. Panel a) shows the rotation of an object with respect to a stationary imaging device. The opposite case is depicted in panel b). The object now is at rest, and the entire imaging device is rotated. As rotating a patient is unreasonable, the latter option is used in medical imaging. Nonetheless, given that rotating a sample is way easier to implement, all non-medical applications are typically performed with a stationary imaging system. Consequently, all measurements presented in this thesis were performed with a rotating object.

In a purely mathematical sense, both methods are identical. It is only a matter of convention which coordinate system is rotated with respect to the other. In figure 3.4 we defined the x, y -coordinate system as that of the sample, and the x', y' -coordinate system as that of the imaging device. Let us define a two-dimensional a rotation matrix $\mathbf{R}(\varphi)$ as:

3 Computed tomography

$$\mathbf{R}(\varphi) = \begin{pmatrix} \cos \varphi & -\sin \varphi \\ \sin \varphi & \cos \varphi \end{pmatrix}. \quad (3.4)$$

We interpret the multiplication of $\mathbf{R}(\varphi)$ with a vector as a rotation around the origin by an angle φ . Specifically, the conversion between the two coordinate systems rotated with respect to each other by an angle φ is then given as simple matrix multiplication:

$$\begin{pmatrix} x \\ y \end{pmatrix} = \mathbf{R}(\varphi) \begin{pmatrix} x' \\ y' \end{pmatrix}. \quad (3.5)$$

Note that the sign of the rotation angle φ changes between figure 3.4 a) and b). This fact becomes clear if we consider the following. To exchange the stationary coordinate system with the rotated one, we need to calculate the inverse of the rotation matrix, \mathbf{R}^{-1} . The application of \mathbf{R}^{-1} must undo the effect of \mathbf{R} , i.e. describe a rotation with opposite sign:

$$\mathbf{R}^{-1} \begin{pmatrix} x \\ y \end{pmatrix} = \mathbf{R}^{-1} \mathbf{R} \begin{pmatrix} x' \\ y' \end{pmatrix} = \begin{pmatrix} x' \\ y' \end{pmatrix}. \quad (3.6)$$

One property of rotation matrices is that the inverse of a rotation matrix is equal to its transpose:

$$\mathbf{R}^{-1} = \mathbf{R}^\top. \quad (3.7)$$

As an example, consider the vector \mathbf{t} that describes the direction of X-rays which is given in laboratory coordinates $\mathbf{t}' = (x', y')^\top$. We will see in the following chapters that it is useful to work in the frame of reference of the sample for the reconstruction of oriented scattering information. For any given sample rotation it is therefore of interest to know the orientation of the X-ray beam in sample coordinates, given as \mathbf{t} . This can easily be calculated using the appropriate rotation matrix as:

$$\mathbf{t} = \mathbf{R}^\top \mathbf{t}'. \quad (3.8)$$

Let us go back to figure 3.4. Even though all measurements performed for this thesis were conducted with a stationary imaging system, the sample is the most important part. As already mentioned, both views are equivalent and easily interchangeable. Therefore we will always consider the sample to be stationary, as shown in panel b), regardless of the actual measurement. A simple representation of the measured sample rotations is sketched in figure 3.4 c). The sample is assumed to be at the origin of the coordinate system. Every point on the unit circle corresponds to a measurement from that indicated position. A complete measurement set consisting of images taken from 13 angles, evenly spaced between $[0, 180]$, is shown here.

3.3 Description of sample rotation by rotation matrices

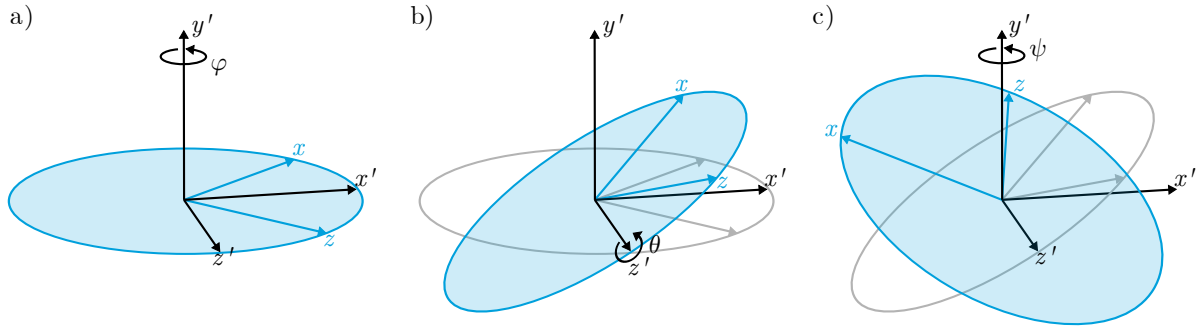


Figure 3.5: **Sample rotation in three dimensions using Euler angles.** With the convention used here, the full rotation consists of a rotation by φ around the y' -axis, followed by a rotation of θ around the z' -axis and a final rotation of ψ around the y' -axis once more. Note that the last rotation differs from the first, if $\theta \neq 0$. Following the different axes of rotation, this convention is also known as YZY.

3.3.2 Rotation in three dimensions and Euler angles

For conventional computed tomography of a scalar field, such as the attenuation coefficient, all necessary data can be recorded by rotating the sample - or imaging system - around a single axis. A single rotation angle, or alternatively a two-dimensional rotation matrix, is sufficient for a full description of the rotation. This changes when dealing with the reconstruction of orientation-dependent X-ray scattering. It is not enough to rotate a sample around a single axis any more. Reasons for this are discussed in chapters 5 and 8, respectively.

For now, let us focus on how to construct a rotation matrix that describes an arbitrary sample rotation in \mathbb{R}^3 . Three-dimensional rotations are required in several fields, including mechanical engineering, crystallography as well as computer graphics. A common way to describe the required rotations relies on three Euler angles. There exist several different definitions, of which only the one used in this thesis is discussed here. Essentially, any full rotation is composed of three successive elementary rotations. Each individual rotation is around a predefined axis of the coordinate system. The Euler angles denoting the magnitude of each of the three elementary rotations therefore are sufficient to describe the full rotation. Figure 3.5 shows the three elementary rotations in the order they are performed in according to the definition used for the rest of this thesis. We again have our sample coordinate system and laboratory coordinate systems denoted as x, y, z and x', y', z' , respectively. The first rotation, shown in a), is around the y' -axis by φ . As the y -axis and y' -axis coincide at this point, the rotation can also be seen around the y -axis. Figure 3.5 b) shows the second rotation. The sample coordinate system now is rotated around the z' -axis by the second Euler angle, θ . Lastly, c) shows the final rotation around the y' -axis by ψ . Each of these rotations can be described by a rotation matrix

3 Computed tomography

$\mathbf{R}(\varphi)$, $\mathbf{R}(\theta)$, $\mathbf{R}(\psi)$, respectively:

$$\mathbf{R}(\varphi) = \begin{pmatrix} \cos \varphi & 0 & \sin \varphi \\ 0 & 1 & 0 \\ -\sin \varphi & 0 & \cos \varphi \end{pmatrix}, \quad (3.9)$$

$$\mathbf{R}(\theta) = \begin{pmatrix} \cos \theta & -\sin \theta & 0 \\ \sin \theta & \cos \theta & 0 \\ 0 & 0 & 1 \end{pmatrix}, \quad (3.10)$$

$$\mathbf{R}(\psi) = \begin{pmatrix} \cos \psi & 0 & \sin \psi \\ 0 & 1 & 0 \\ -\sin \psi & 0 & \cos \psi \end{pmatrix}. \quad (3.11)$$

Successive application of matrices is equivalent to matrix multiplication of the individual matrices [Fischer, 2005, pp. 143-147]. The full rotation matrix $\mathbf{R}(\psi, \theta, \varphi)$ therefore is calculated as the product of the three individual rotation matrices:

$$\mathbf{R}(\psi, \theta, \varphi) = \mathbf{R}(\psi)\mathbf{R}(\theta)\mathbf{R}(\varphi). \quad (3.12)$$

With abbreviating cosine and sine as c and s, respectively, the complete definition of $\mathbf{R}(\psi, \theta, \varphi)$ reads:

$$\mathbf{R}(\psi, \theta, \varphi) = \begin{pmatrix} -s\psi \cdot s\varphi + c\theta \cdot c\psi \cdot c\varphi & -s\theta \cdot c\psi & s\psi \cdot c\varphi + c\theta \cdot c\psi \cdot s\varphi \\ s\theta \cdot c\varphi & c\theta & s\theta \cdot s\varphi \\ -c\psi \cdot s\varphi - c\theta \cdot s\psi \cdot c\varphi & s\theta \cdot s\psi & c\psi \cdot c\varphi - c\theta \cdot s\psi \cdot s\varphi \end{pmatrix}. \quad (3.13)$$

The order of the matrix multiplication here is important, as \mathbb{R}^3 rotation matrices do not commute. As the vector-matrix multiplication introduced in equation 3.5 is from the right, the rightmost matrix corresponds to the first rotation, etc. For this reason, the correct order is given as $\mathbf{R}(\psi)\mathbf{R}(\theta)\mathbf{R}(\varphi)$. If the order was inverted, the resulting matrix is exactly the inverse of $\mathbf{R}(\psi, \theta, \varphi)$:

$$\mathbf{R}(\psi, \theta, \varphi)^{-1} = \mathbf{R}(\varphi)\mathbf{R}(\theta)\mathbf{R}(\psi). \quad (3.14)$$

This can easily be seen by exchanging ψ and φ in equation 3.13. The resulting matrix is equivalent to $\mathbf{R}(\psi, \theta, \varphi)^\top$, and therefore $\mathbf{R}(\psi, \theta, \varphi)^{-1}$.

As the definition of the Euler angles used here comprises rotations around y', z' and y' , it is also known as YZY convention. The practical implementation of these rotations in the form of an Eulerian Cradle can be found in figure 8.3 on page 102.

Imaging with small-angle X-ray scattering 4

This chapter provides an introduction to small-angle X-ray scattering (SAXS) as an imaging technique. An overview of various different SAXS imaging techniques is presented. Two-dimensional SAXS projection imaging as well as three-dimensional tomographic reconstruction of the SAXS signal are discussed. Possibilities and current limitations of these methods are outlined.

4.1 Small-angle X-ray scattering experiment

Since its development in the first half of the 20th century, SAXS has been widely used to determine size and structure of macromolecules in solution [Guinier, 1955; Glatter, 1982]. The intensity scattered under small angles yields valuable information about nanometre sized structures (cf. section 2.2). Figure 4.1 a) gives an overview of a standard SAXS experiment.

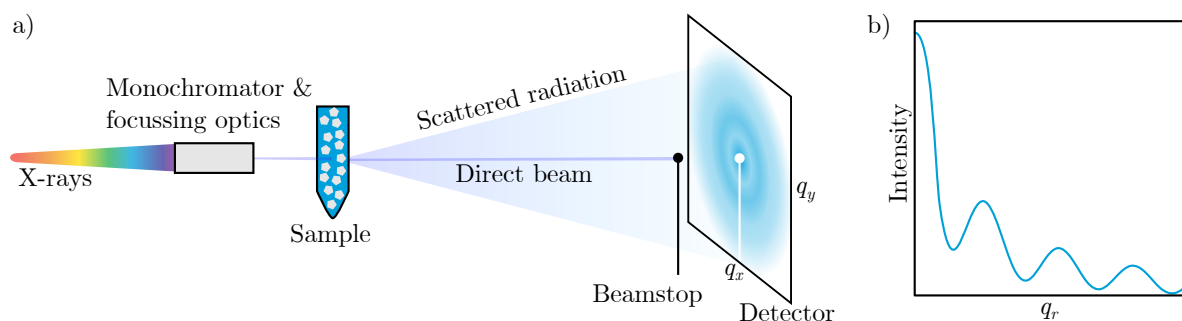


Figure 4.1: **Small-angle X-ray scattering experiment.** a) Overview of the essential parts for a SAXS experiment. A beam of monochromatic, focussed X-rays is created by a monochromator and focussing optics, respectively. A sample, typically macromolecules in solution, in the beam gives rise to X-ray scattering. As the scattering angles investigated with SAXS are very small, the detector has to be placed at a relatively large distance behind the sample. This allows the scattered radiation to be separated from the direct, unscattered beam. The latter is caught by a beamstop in order to protect the position sensitive detector on which SAXS patterns are recorded. Note that scattering angles here are drawn greatly exaggerated. b) Data analysis is performed on azimuthally integrated data.

4 Imaging with small-angle X-ray scattering

Monochromatic X-rays are required so that intensity scattered under a certain angle can be unambiguously associated to the correct scattering vector \mathbf{q} . Therefore, it is essential to use a monochromator that limits the incident beam to X-rays of a single wavelength. Owing to the high X-ray flux available at a synchrotron, the X-ray beam is typically focussed to a fine, so-called pencil beam. Although wider beams can be used in a SAXS experiment, a pencil beam greatly facilitates subsequent data analysis [Pauw, 2013]. Given the small angles under investigation, the detector is placed at a distance far enough behind the sample to separate the scattered radiation from the direct beam. Although not shown here, an evacuated flight tube is often installed in the free space between the sample and detector. This reduces parasitic scattering at air molecules and improves data quality. With the high flux available at modern synchrotron beamlines, pixelized area detectors are used to collect the scattered radiation. In order to protect the detector from the very intense direct beam, a beamstop is used to collect the unscattered X-rays.

Many macromolecules do not exist in crystalline form and are not suited for X-ray crystallography. However, as atomic distances are not relevant, SAXS is well suited for the investigation of non-crystalline samples. Therefore, experiments are often performed in solution, as shown in figure 4.1. The downside is that rotationally averaged information is retrieved [Glatter, 1982, p. 4]. Owing to this, data analysis is restricted to azimuthally integrated, one-dimensional data as shown in b). Only the radial component of the scattering vector $q_r = |\mathbf{q}| = q$ can be used in the analysis of solution SAXS, due to the rotationally averaged data. Nonetheless, this one-dimensional data is very valuable for structure determination.

4.2 Local differential cross section

For the scope of this thesis, it is important to take a closer look at the role of coherence in SAXS experiments with emphasis on tomographic imaging. An extensive analysis on this topic is given in [Feldkamp, 2011, pp. 61-64]. The most important results are repeated here. Obviously there is little benefit to performing imaging experiments on a homogeneous solution of particles as introduced in the previous section. Therefore, the term sample refers to a macroscopic solid object from now on.

From the concept of coherence length presented in section 2.2.1, it follows that the measured SAXS signal is the incoherent sum from many coherence areas. However, coherence lengths in direction of the beam often surpass the size of a sample. Owing to this, summation of the scattered amplitude from different parts of the sample along the beam direction is coherent. This poses a problem for SAXS imaging, in particular for computed tomography (CT). As described in chapter 3, CT relies on line integrals that represent incoherent summations along the beam direction. This stands in contrast to the coherent addition in beam direction caused by large coherence lengths [Feldkamp, 2011, p. 64].

An elegant solution that resolves this problem was presented in [Feldkamp, 2011, pp. 61-64]. We assume the nano-structures of several adjacent coherence areas perpendicular to

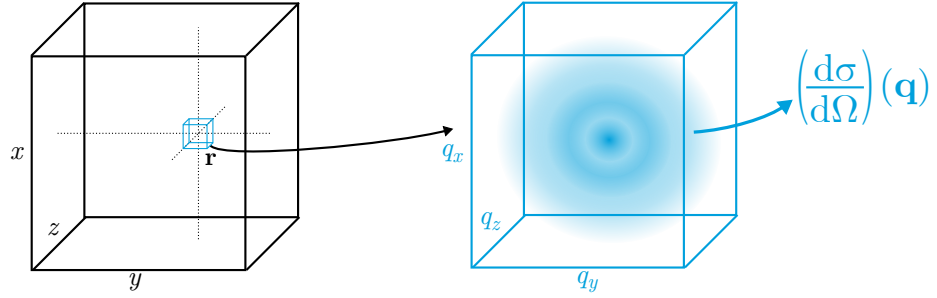


Figure 4.2: **Local differential cross section.** An object is described by a six-dimensional function $\left(\frac{d\sigma}{d\Omega}\right)(\mathbf{q}, \mathbf{r})$. This spatially resolved differential cross section describes the scattering characteristics at every position \mathbf{r} of the object.

the beam direction to be very similar without being identical copies. These assumptions are easily met for non-crystalline samples that are encountered in SAXS imaging. As there are a large number of coherence areas in an X-ray beam, the effects of coherent summation along the beam direction are effectively cancelled out.

Therefore we use the local differential cross section $\left(\frac{d\sigma}{d\Omega}\right)(\mathbf{q}, \mathbf{r})$ as a function of six variables in $\mathbb{R}^3 \times \mathbb{R}^3$ to describe the scattering behaviour of a sample. Real space-resolution is given by three variables $\mathbf{r} = (x, y, z)^\top$, and the actual differential cross section depends on the momentum transfer vector, given by another three variables in reciprocal space, $\mathbf{q} = (q_x, q_y, q_z)^\top$. A way to look at this is sketched in figure 4.2. At every position \mathbf{r} , a local differential cross section $\left(\frac{d\sigma}{d\Omega}\right)(\mathbf{q}, \mathbf{r})$ describes the scattering distribution from a small volume element.

The recorded scattered intensity $I_{\text{SAXS}}(\mathbf{q})$ is proportional to the integral of $\left(\frac{d\sigma}{d\Omega}\right)(\mathbf{q}, \mathbf{r})$ over the entire volume probed by the beam. For a thin beam, as used in SAXS, this can be seen as a line integral along the line L of the X-ray beam through the sample:

$$I_{\text{SAXS}}(\mathbf{q}) \propto \int_L \left(\frac{d\sigma}{d\Omega}\right)(\mathbf{q}, \mathbf{r}). \quad (4.1)$$

An important consequence of equation 4.1 is that the three-dimensional tomographic reconstruction of $\left(\frac{d\sigma}{d\Omega}\right)(\mathbf{q}, \mathbf{r})$ can be based on the same formulations used for conventional CT.

It is important to realize that this description breaks down for infinitesimally small sub-volumes of the sample and only works in the limit of a finite sub-volume consisting of many coherence volumes. Owing to limited real-space resolution defined by the size of the X-ray beam used in SAXS imaging, we are not concerned with coherence effects. Furthermore, it is debatable whether a description using summations, or one using integration is more accurate when considering the effects of a thick sample. For convenience and consistency with conventional tomography, we will be using integrals here. One should, however, keep in mind that for infinitesimally small volumes this is not exact. This problem is

4 Imaging with small-angle X-ray scattering

inevitable in scattering-based imaging, as an infinite spatial resolution renders structure investigation through scattering experiments pointless. Within these limitations, we will use the discretized form of $\left(\frac{d\sigma}{d\Omega}\right)(\mathbf{q}, \mathbf{r})$ to represent an object from here on.

4.3 Scanning small-angle X-ray scattering

It was not until the end of the last century that SAXS started being used as an imaging technique [Fratzl, 1997]. The goal in SAXS imaging is to use localized SAXS data to create spatially resolved information about the nano-structure of an extended object. An illustration of a such an experiment is given in figure 4.3. The basic experimental setup is identical to the one introduced in the previous chapter. The sample is placed into a narrowly focussed beam and the scattered intensity is recorded by an area detector. The use of a pencil beam allows the illumination of a small part of the sample at a time and record localized SAXS information [Fratzl, 1997]. A map of the local SAXS signal is created by changing the position of the beam at the sample plane. This is done by adjusting the position of a sample in the plane perpendicular to the beam direction. If we assume the beam direction to be z' here, the sample translation is in x' and y' . A two-dimensional image is created by raster-scanning the object along these two axes through the beam and recording a SAXS pattern at each position. Owing to this procedure, SAXS imaging is also known as scanning SAXS. The inset displayed in figure 4.3 shows how local SAXS patterns are recorded at each point of a sample with scanning SAXS. Note that this is merely an illustration of the imaging technique, and a more thorough analysis than simply stitching SAXS patterns together is generally performed.

Two different kinds of resolutions need to be distinguished in scanning SAXS. While the spatial resolution depends on the size and shape of the X-ray beam and the stepping intervals, resolution in reciprocal space is solely given by the SAXS part of the experiment. The step size between neighbouring points typically is chosen to match the size of the beam, i.e. a step size of $50\ \mu\text{m}$ in both horizontal and vertical direction is chosen for a $50\ \mu\text{m} \times 50\ \mu\text{m}$ beam. Reciprocal space resolution in SAXS is a combination of source characteristics, experimental geometry and detector.

The data obtained from scanning SAXS experiments contains a lot of information. Rather than a two-dimensional image, the complete data set is a four-dimensional combination of real- and reciprocal space. Raster scanning in combination with a pencil beam allows for SAXS data to be spatially resolved in two real space dimensions, x' and y' . Owing to the small-angle approximation (cf. chapter 2.2) the recorded SAXS data itself corresponds the two-dimensional slice of the three-dimensional reciprocal space perpendicular to the beam direction. Therefore, scanning SAXS provides access to two dimensions in real-, as well as two dimensions in reciprocal space. For a complete scanning SAXS projection image, the intensity in each detector pixel and position of the image $I(q_{x'}, q_{y'}, x', y')$, therefore is a function of four variables. Let the direction of the X-ray beam with initial intensity I_0 be z' . The measured intensity is then given as the integral along z' :

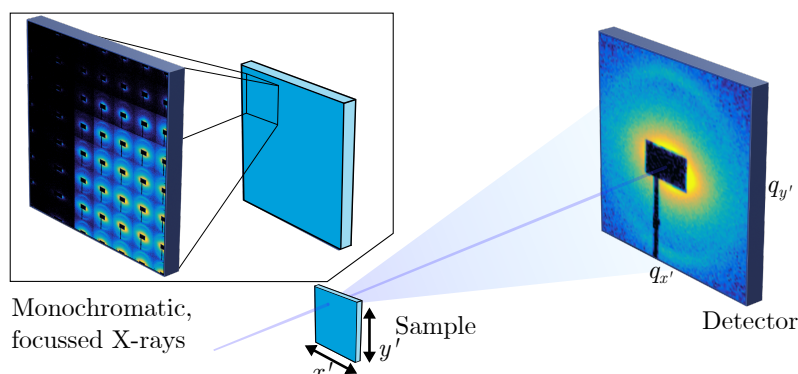


Figure 4.3: **Scanning small-angle X-ray scattering.** The sample is illuminated with a focussed, monochromatic X-ray beam. Spatially resolved SAXS information is recorded by raster scanning the sample through the beam perpendicular to the beam in x' and y' direction. The combination of a finely focussed beam and raster scanning allows to collect SAXS patterns at distinct positions of the sample. A position resolved detector is used to record the scattered intensity. The inset shows how the spatially resolved SAXS information changes across the sample.

$$I(q_{x'}, q_{y'}, x', y') = I_0 \int \left(\frac{d\sigma}{d\Omega} \right) (q_{x'}, q_{y'}, x', y', z') dz'. \quad (4.2)$$

As with conventional X-ray projection imaging, all depth information of the signal is lost as a consequence of the integration. Scanning SAXS, therefore, is best performed on thin objects, for which depth information is of little importance. This limitation can be overcome using computed tomography, see section 4.6.

One class of materials commonly investigated with scanning SAXS is biological tissues. These materials are made up of nanometre sized collagen fibres which give rise to a very characteristic SAXS signal. Ever since its early days, scanning SAXS has been used to investigate biological materials such as bone [Fratzl, 1997; Rinnerthaler, 1999; Žižak, 2000; Giannini, 2012] and the bone-like dentine found in teeth [Kinney, 2001; Märten, 2010]. Examples of other biological materials that have been subject to scanning SAXS studies are muscle tissue [Bunk, 2009], cornea tissue [Boote, 2004; Meek, 2009], or leather [BasilJones, 2010]. Scanning SAXS experiments have also been conducted on man-made materials such as polymers [LorenzHaas, 2003], carbon fibres [Fratzl, 2003; Loidl, 2005], and friction stir welds inside aluminium [Dumont, 2006]. Recently, scanning SAXS was used to investigate the flow behaviour of surfactants confined inside microfluidic flow channels [Martin, 2016; LutzBueno, 2016].

4 Imaging with small-angle X-ray scattering

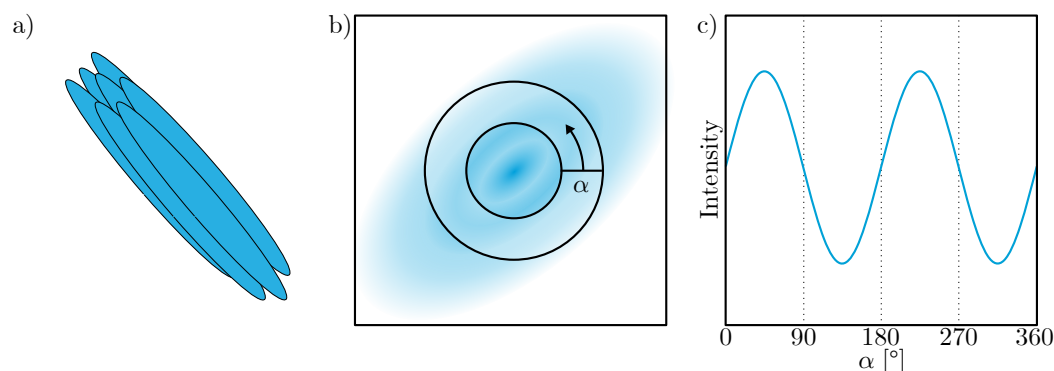


Figure 4.4: **Anisotropic scattering intensity distribution.** An anisotropic sample, shown in a), exhibits a preferential orientation in its scattering pattern, shown in b). From the anisotropic scattering signal, conclusions about the orientation of the underlying structure can be drawn. c) The plot shows the radially integrated intensity over the highlighted area plotted against the azimuthal angle α .

4.4 Orientation analysis using scanning SAXS

Particles in solution are mostly free to move and the measured signal, therefore, corresponds to the average over all possible particle orientations. For solid objects, however, an anisotropic nano-structure gives rise to an anisotropic scattering signal. One recurring type of analysis in almost all scanning SAXS works is the extraction of nano-structure orientation. A common way of doing this is by analysing the intensity distribution with respect to the azimuthal angle α , as demonstrated in figure 4.4 [Fratzl, 1997]. The structure shown in a) causes an anisotropic scattering pattern b). Panel c) shows a simple type of orientation analysis. The intensity is radially integrated in the highlighted area and plotted against α . The maxima and minima of the resulting curve allow us to accurately determine structure orientations. This type of analysis has been extended to take advantage also of the shape, as well as radial changes of the curve [Bunk, 2009].

4.5 Three-dimensional scanning SAXS

Two limitations remain in scanning SAXS. Both the differential cross section in reciprocal-space, as well as the real space distribution inside the sample are three-dimensional functions. As already mentioned, scanning SAXS is only able to provide information in four out of these six dimensions. A way to extend scanning SAXS to the third dimension in reciprocal space was given in the form of 3-D scanning SAXS [Wagermaier, 2007; Liu, 2010; Georgiadis, 2015]. An illustration of this method is given in figure 4.5.

3-D scanning SAXS requires the use of thin, quasi two-dimensional samples. For such

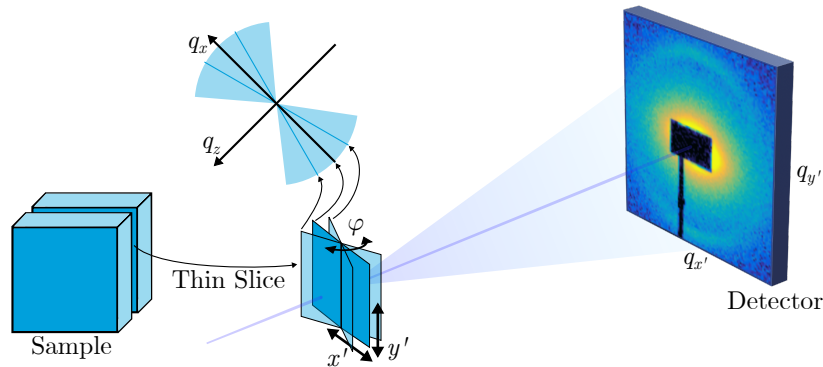


Figure 4.5: **3-D scanning SAXS**. This technique aims to add an additional dimension to the data measured with scanning SAXS. A thin slice is physically extracted from a bulk sample and placed into the beam. Scanning SAXS projections are taken under different rotations of the slice. Each projection image probes a different two-dimensional slice of the reciprocal space. By combining the individual projections, the third dimension in reciprocal space becomes accessible. Three-dimensional information in real space is achieved by physically slicing an object.

a sample, the integral in equation 4.2 can be neglected and rotating a thin slice up to a certain angle does not drastically change which parts of the sample overlap in beam direction. This is contrary to computed tomography, where a rotation drastically changes the integrated signal. Here, the same area of the sample is measured under different rotations φ . As the signal in reciprocal space is the two-dimensional slice perpendicular to the beam direction, the third dimension in reciprocal space, \mathbf{q}_z here, can be accessed by rotation of the sample. A three-dimensional reciprocal space can be reconstructed at each position of the two-dimensional sample using 3-D scanning SAXS. The technique, however, is limited to two dimensions in real space. A three dimensional analysis of an extended object is only possible by physically slicing the object into many successive thin slices and imaging each one of them individually.

4.6 Small-angle X-ray scattering computed tomography

So far the information obtained with scanning SAXS is restricted to two spatial dimensions. Although 3-D scanning SAXS offers the possibility to extend the analysis to three dimensions in reciprocal space, it is limited to thin slices only. If one is interested in spatially resolved SAXS information in three dimensions, both these methods are not sufficient. Computed tomography was introduced in chapter 3 as a method to retrieve three-

4 Imaging with small-angle X-ray scattering

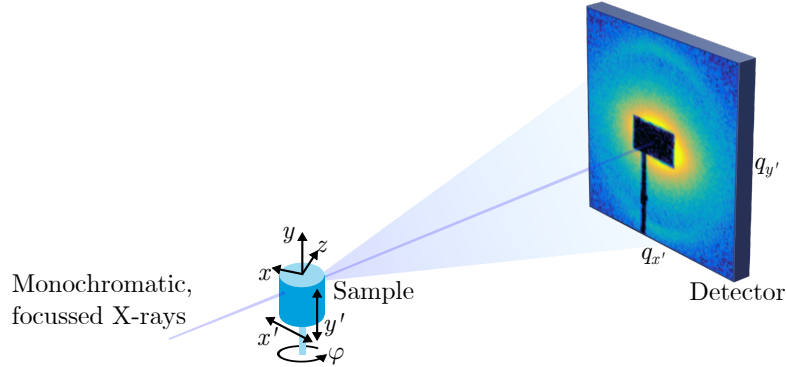


Figure 4.6: **Sketch of a SAXS-CT experiment.** The scanning-SAXS experiment shown in figure 4.3 is extended by an additional rotation of the sample around the vertical axis. The direction of the scanning remains constant for all rotations along the laboratory x' - and y' -axes.

dimensional information from two-dimensional projection images. As scanning SAXS provides projection images of an object in a sense, a logical step is to perform CT with data based on scanning SAXS. Just like 3-D scanning SAXS, CT requires a rotation of the sample with respect to the imaging system. However, in contrast to 3-D scanning SAXS, the rotation angle φ has to cover at least 180° , as shown in figure 4.6. It is important to note that the direction of the scanning motion during acquisition of a single scanning SAXS image remains unchanged under rotation of the sample. Regardless of its rotation, the sample is always scanned in the plane perpendicular to the beam.

The goal in SAXS-CT is to reconstruct $\left(\frac{d\sigma}{d\Omega}\right)(\mathbf{q}, \mathbf{r})$. The following presentation of SAXS tomography aims to keep the mathematical formulation easily readable and intuitive, rather than being mathematically exact.

Let us introduce necessary notation with the help of figure 4.7. We consider the local three-dimensional cross section $\left(\frac{d\sigma}{d\Omega}\right)(\mathbf{q}, \mathbf{r})$ in reciprocal space, sketched in a). We recall that with a single scanning SAXS image, we are only able to measure a two-dimensional slice out of this three-dimensional reciprocal space function (cf. 4.3). For an incident beam in direction given by the unit vector \mathbf{t} , we denote the slice perpendicular to \mathbf{t} out of $\left(\frac{d\sigma}{d\Omega}\right)(\mathbf{q}, \mathbf{r})$ as $\left(\frac{d\sigma}{d\Omega}\right)_{\perp\mathbf{t}}(\mathbf{q}, \mathbf{r})$. As the direction of \mathbf{t} depends on the orientation of the sample during a tomography measurement, so does $\left(\frac{d\sigma}{d\Omega}\right)_{\perp\mathbf{t}}(\mathbf{q}, \mathbf{r})$. In addition, a rotation of the sample also causes the volume illuminated by the beam to change. According to section 4.2 we consider a sample to be made up of many small scattering volumes. The scattered intensity from each of these volumes is given by their local differential cross sections. Figure 4.7 b) shows the discretized case of a two-dimensional sample. Each of the square areas represents a local scattering area. For a single measurement, i.e. one diffraction pattern on the detector, only part of the sample is illuminated by the beam.

For a given measurement i , the scattered intensity I_i then depends on the integral of

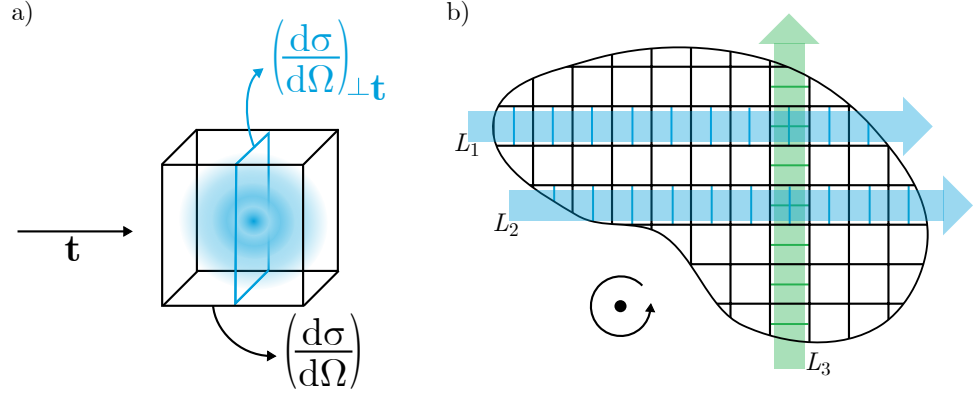


Figure 4.7: **Scattering vectors probed with SAXS-CT.** a) A two-dimensional slice of $\left(\frac{d\sigma}{d\Omega}\right)_{\perp\mathbf{t}}$ perpendicular to \mathbf{t} is probed with a single measurement. b) Rotation of an object during a CT measurement not only changes the reciprocal space data that is recorded, but also the integration path of the X-ray beam.

$\left(\frac{d\sigma}{d\Omega}\right)_{\perp\mathbf{t}_i}(\mathbf{q}, \mathbf{r})$ along a line L_i through the sample:

$$I_i = I_0 \int_{L_i} \left(\frac{d\sigma}{d\Omega}\right)_{\perp\mathbf{t}_i}(\mathbf{q}, \mathbf{r}). \quad (4.3)$$

In figure 4.7 b), three different beam paths through the sample are denoted by L_1 , L_2 and L_3 . Paths L_1 and L_2 show measurements from the same orientation of the sample, i.e. what can be considered two points of a scanning SAXS image. Although the integration is along two different paths through the sample, the orientation of the X-ray beam is the same, $\mathbf{t}_1 = \mathbf{t}_2$. Owing to this, the same plane in reciprocal space is probed for both measurements. The only difference is that different parts of the sample are illuminated for L_1 and L_2 . The third path through the sample, L_3 , integrates information from a different slice in reciprocal space, as it is along a different spatial orientation. Therefore, even if some parts of the sample are illuminated by L_1 or L_2 , as well as L_3 , the probed scattering information for each beam is unique.

Computed tomography of $\left(\frac{d\sigma}{d\Omega}\right)_{\perp\mathbf{t}_i}(\mathbf{q}, \mathbf{r})$ is severely hindered by this dependence of the SAXS signal on the illumination, not only in real-, but also in reciprocal space. However, there exist two special cases, for which SAXS-CT can be treated analogous to conventional CT. We differentiate between rotationally isotropic, and anisotropic SAXS signals.

4.6.1 Isotropic signal

Let us first assume a sample with an isotropic average nanostructure. A random distribution of particles inside a matrix is one example of this. It was mentioned in section 4.1 that data analysis is restricted to azimuthally integrated, one-dimensional data $q = |\mathbf{q}|$, for an isotropically scattering sample. Given that different q can be treated completely

4 Imaging with small-angle X-ray scattering

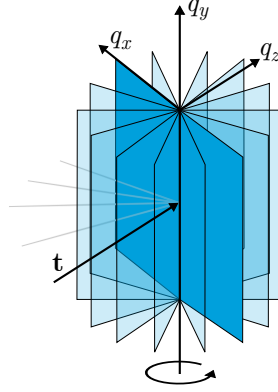


Figure 4.8: **Rotational invariance of the scattering signal.** A rotation around the vertical axis during a CT measurement causes a different reciprocal space slice $\left(\frac{d\sigma}{d\Omega}\right)_{\perp\mathbf{t}}$ to be recorded for each view of the sample. Data for \mathbf{q} -vectors parallel the rotation axis are recorded for all rotations.

independent from one another, the scattering signal for a single q breaks down to a scalar value:

$$I_i(q) = I_0 \int_{L_i} \left(\frac{d\sigma}{d\Omega}\right)(q, \mathbf{r}). \quad (4.4)$$

This formulation of the recorded signal is identical to that of conventional CT (cf. chapter 3), with the exception that a discrimination of different q is possible. SAXS-CT of an isotropic signal has been presented e.g. by Jensen et al. [Jensen, 2011b; Jensen, 2011a]. This method is well suited for samples that are known to scatter isotropically. If no a priori information about a sample exists, an anisotropic scattering signal has to be assumed. This is the second case we will examine here.

4.6.2 Anisotropic signal and rotational invariance

In the previous section, we have seen that SAXS-CT is possible in the limiting case of isotropically scattering samples. While this is the case for almost all studies in solution, solid samples often have a nanostructure with preferred orientation. The assumption of an isotropic signal breaks down in this case, and a reconstruction using azimuthally integrated data is not possible any more. Nonetheless, Feldkamp et al. have shown that parts of the signal can be treated as being invariant under rotation [Feldkamp, 2009]. Figure 4.8 gives a visualization of how a sample rotation during CT affects the reciprocal plane from which the SAXS signal is probed. Here we want to show that parts of the reciprocal space are probed for all rotations of the sample. The tomographic rotation so far has always been around the y' -axis, for which a rotation matrix $\mathbf{R}(\varphi)$ was given by equation 3.9 as

4.6 Small-angle X-ray scattering computed tomography

$$\mathbf{R}(\varphi) = \begin{pmatrix} \cos \varphi & 0 & \sin \varphi \\ 0 & 1 & 0 \\ -\sin \varphi & 0 & \cos \varphi \end{pmatrix}. \quad (4.5)$$

Prior to any rotation, the laboratory coordinate system x', y', z' and the sample coordinate system x, y, z coincide, and therefore $\mathbf{q}' = \mathbf{q}$. For an X-ray beam direction $\mathbf{t}' = (0, 0, 1)$, scattering information of the $(q_{x'}, q_{y'}, 0)$ slice is recorded. A rotation of the sample changes the relation between \mathbf{q}' and \mathbf{q} . After rotation, a vector \mathbf{q} can be expressed in laboratory coordinates as $\mathbf{q}' = \mathbf{R}(\varphi)^\top (q_x, q_y, q_z)^\top$. We notice from equation 4.5 that $\mathbf{R}(\varphi)$ does not affect the q_y -component. Owing to this, any reciprocal space vector $\mathbf{q} = (0, q_y, 0)$ is unaffected by $\mathbf{R}(\varphi)$.

Technically, the scattered intensity for any \mathbf{q} -vector is invariant under rotation about any axis. The question should rather be whether we are able to access that information or not, i.e. whether the relation between \mathbf{q} and \mathbf{q}' is rotationally invariant. For a SAXS-CT measurement, scattering information for \mathbf{q} -vectors that have only a non-zero q_y -component is recorded for all rotations of the sample. As a consequence, all parts of the recorded SAXS patterns with $\mathbf{q} = (0, q_y, 0)$ can be treated as scalar values:

$$I_i(q_y) = I_0 \int_{L_i} \left(\frac{d\sigma}{d\Omega} \right) (0, q_y, 0, \mathbf{r}). \quad (4.6)$$

This allows for a standard reconstruction of all $(0, q_y, 0)$ -vectors. There is no a priori information about the sample required as for the already discussed case of isotropic scattering. Any possible sample can therefore be measured, as part of the scattering vectors can always be reconstructed. As a downside, however, this drastically reduces the amount of useful data from a measurement. Whereas for the isotropic case all of the information contained in the measured SAXS pattern can be used for the reconstruction, only a small fraction of the data is used for the partial reconstruction of an anisotropic signal.

Even though we restricted ourselves to a rotation around the y' -axis here, rotational invariance of the signal for small-angle scattering experiments can be generalized as [Feldkamp, 2009]:

$$\left(\frac{d\sigma}{d\Omega} \right) (\mathbf{q}, \mathbf{r}) \text{ can be reconstructed for all } \mathbf{q} \parallel \mathbf{a}, \text{ where } \mathbf{a} \text{ is the axis of rotation}$$

This statement is of great importance for computed tomography based on small-angle scattering data. Regardless of the sample, it shows that a partial reconstruction of the scattering signal is possible.

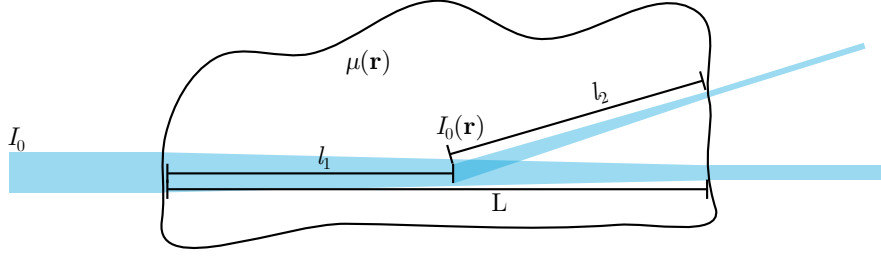


Figure 4.9: **Attenuation in scattering experiments.** Both the incident beam and the scattered beam receive attenuation along paths l_1 and l_2 , respectively.

4.6.3 Attenuation in SAXS-CT

So far we have treated the sample to be non-absorbing, i.e. $\mu(x, y, z) = 0$. In a real experiment, however, X-ray attenuation occurs both for the incident and scattered radiation alike. We define l_1 as the path of the incident beam leading up to a scattering centre according to figure 4.9. The remaining path of the scattered beam inside the sample is denoted as l_2 . X-ray attenuation occurs along both paths according to the exponential Lambert-Beer-Law given by equation 2.20. Attenuation of the incident beam along l_1 leads to a position-dependent illumination I_{0,l_1} :

$$I_{0,l_1} = I_0 e^{-\int_{l_1} \mu(\mathbf{r})}. \quad (4.7)$$

The exit path for scattered radiation, l_2 , depends both on the diffraction angle, and therefore \mathbf{q} , as well the position from which scattering inside the sample occurs, \mathbf{r} . Owing to this, modelling of attenuation in scattering experiments proves to be challenging. The present case of small-angle scattering allows to us to employ several simplifications. Given that the investigated scattering angles are very small, we can approximate l_2 to run in the same direction as l_1 [Jensen, 2011b]. As a consequence of this, the exit path is now independent of \mathbf{q} . We extend equation 4.3 to include attenuation and arrive at:

$$I = \int_L I_0 e^{-\int_{l_1} \mu(\mathbf{r})} \left(\frac{d\sigma}{d\Omega} \right)_{\perp \mathbf{t}}(\mathbf{r}) e^{-\int_{l_2} \mu(\mathbf{r})}. \quad (4.8)$$

Here we included the position dependent illumination from equation 4.7, as well attenuation of the scattered beam. For this, the attenuation coefficient $\mu(\mathbf{r})$ is integrated along paths l_1 and l_2 , respectively. It is obvious that the combination of l_1 and l_2 yields the complete path L of the X-ray beam through the sample. The integrations of $\mu(\mathbf{r})$ can therefore be combined into a single integral over L [Jensen, 2011b]:

$$I = I_0 e^{-\int_L \mu(\mathbf{r})} \int_L \left(\frac{d\sigma}{d\Omega} \right)_{\perp \mathbf{t}}(\mathbf{r}). \quad (4.9)$$

As we lose the splitting of L into l_1 and l_2 , we are able to pull $I_0 \exp[-\int_L \mu(\mathbf{r})]$ out of the integral. The entire attenuation only depends on the full path L through the sample. For

4.7 Dimensionality of small-angle X-ray scattering imaging techniques

	Dim_{real}	$Dim_{reciprocal}$	
solution SAXS	0	1	[Guinier, 1955]
scanning SAXS	2	2	[Fratzl, 1997; Rinnerthaler, 1999; LorenzHaas, 2003; Bunk, 2009; LutzBueno, 2016; Martin, 2016]
3-D scanning SAXS	2	3	[Wagermaier, 2007; Liu, 2010; Georgiadis, 2015]
SAXS-CT	3	1	[Schroer, 2006; Stribeck, 2006; Feldkamp, 2009; Jensen, 2011a; Jensen, 2011b]
<i>6-D SAXS-CT</i>	3	3	-

Table 4.1: **Overview of different SAXS-imaging techniques.** The dimensionality of the obtained data in real- and reciprocal space, Dim_{real} and $Dim_{reciprocal}$, respectively, is given. No technique is able to yield a complete six-dimensional data set. A *6-D SAXS-CT* that fills this void is presented in this thesis.

a given path L , it is constant for all \mathbf{q} . Equation 4.9 is only valid for the limiting case of small-angle scattering, as only this assumption allows us to formulate a secondary path l_2 , independent of the scattering angle. This results also shows that it does not matter whether attenuation occurs before or after scattering for SAXS. Attenuation correction of the scattered data can be performed according to equation 4.9 by measuring the ratio of the unscattered beam behind the sample and I_0 .

4.7 Dimensionality of small-angle X-ray scattering imaging techniques

Table 4.1 gives an overview of the different SAXS-imaging techniques presented in this chapter. In particular, the number of accessible dimensions in real- and reciprocal space are listed. Three dimensions can be accessed both in real- and reciprocal space, but no technique is able to do so simultaneously thus far. Even though multi-dimensional information in reciprocal space is recorded during scanning-SAXS, a three dimensional real-space reconstruction of an object is only possible with one-dimensional reciprocal-space data. In particular, this means that any orientation-dependency of the scattering signal is lost during tomography. However, this part of the SAXS signal can be very valuable for characterizing the nanostructure of partially ordered systems.

The next chapter presents a SAXS imaging method that maintains three-dimensional scattering information throughout a three-dimensional reconstruction. The aim is a full reconstruction of the three-dimensional reciprocal space at every point of a sample, i.e. $\left(\frac{d\sigma}{d\Omega}\right)(\mathbf{q}, \mathbf{r})$. Consequently, it is called *6-D SAXS-CT* in table 4.1.

As presented in the last chapter, small-angle X-ray scattering (SAXS) in combination with computed tomography (CT) is a powerful hybrid imaging technique. The local nanostructure can be characterized non-destructively in macroscopic samples by reconstructing a spatially resolved scattering signal. Given that structural information is obtained independently from spatial resolution, a trade-off between resolution and field of view in the traditional sense does not exist for SAXS imaging. However, SAXS-CT has been limited to one reciprocal space dimension only. Owing to this, any directional information of the SAXS signal is lost during the reconstruction.

In order to make use of that information, we developed an advanced SAXS-CT method, namely six-dimensional small-angle X-ray scattering computed tomography (6-D SAXS-CT). Detailed theory and results of 6-D SAXS-CT are presented in this chapter. The topic was also covered in the following publication, from which some of the figures are adapted:

Schaff, F., Bech, M., Zaslansky, P., Jud, C., Liebi, M., Guizar-Sicairos, M. & Pfeiffer, F. Six-dimensional real and reciprocal space small-angle X-ray scattering tomography. *Nature* **527**, 353-356 (2015).

5.1 Experimental requirements for 6-D SAXS-CT

If we take a closer look at the free variables during a SAXS imaging measurement, we quickly realize that using two translations, one rotation and a two-dimensional position resolved detector only yields five independent variables. However, we set out to reconstruct a six-dimensional quantity. It is clear that such a reconstruction from data with only five independent variables is an ill-posed problem [Feldkamp, 2011, pp. 56-57]. We therefore need to extend the measurement by an additional variable. For this reason we implement a second rotation to our experimental setup as shown in figure 5.1. This allows us to tilt the original rotation axis around x' by an angle θ . The translations necessary for scanning SAXS remain along x' and y' . Rather than around a fixed axis, the rotation around φ now also depends on θ . In terms of sample coordinates, φ is a rotation around y for all θ .

At first, the exact choice for this second rotation might not be entirely clear. It is, indeed, an arbitrary choice to tilt the primary rotation axis by θ around x' . Any axis in the plane parallel to the detector would be equally valid. It is only important that the tilt

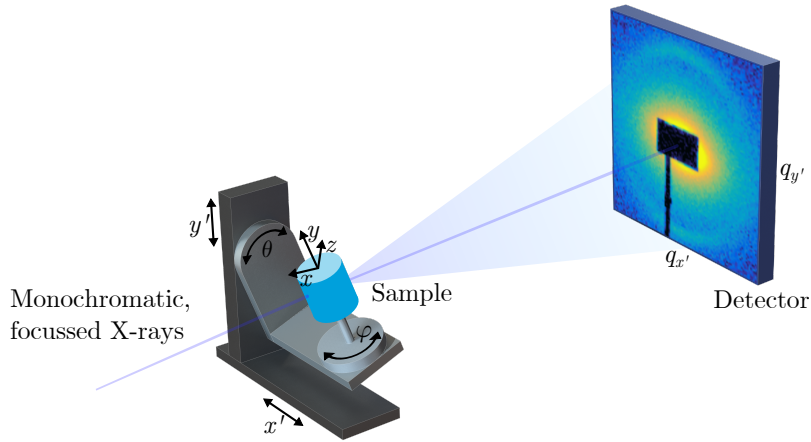


Figure 5.1: **Experimental setup for 6-D SAXS-CT.** For conventional SAXS-CT the sample is translated in x' and y' and rotated around y by φ . 6-D SAXS-CT requires an additional degree of freedom. For this a second rotation of the sample around x' by θ is introduced.

is performed around an axis parallel to the detector. Consider the other extreme, a tilt around the axis perpendicular to the detector. This tilt is completely useless as it is equivalent to a simple rotation of the detector. No additional data can be recorded that way. These rotations conform with the notation using Euler angles given in chapter 3.3.2 if $\psi = 90^\circ$.

5.1.1 Effect of an additional axis of rotation

Let us discuss of the possibilities an additional rotation offers during a measurement. Figure 5.2 shows three different tilt angles $\theta = 0^\circ, 30^\circ, 60^\circ$ of the original rotation axis in a), b) and c), respectively. The measured directions are visualized using the method introduced in chapter 3.3.2. Each filled point represents one detector position. Empty point are used to indicate the exact opposite positions, which would yield identical data. All points of the previous panels are maintained in panels b) and c) for reference, along with the new points. It is clear that additional information is probed for $\theta \neq 0^\circ$. It is important to note that the standard case without any tilt angle only requires a rotation over 180° , since the mirrored positions lie on the same trajectory as the original points. For $\theta \neq 0^\circ$, this is not the case any more, as the trajectory of the mirrored directions no longer coincides with that of the actual measurements. Given that all mirrored points lie on the opposite hemisphere, additional information is obtained by measuring a full 360° rotation for $\theta \neq 0^\circ$. For this reason, a rotation of φ over 180° is shown for a), and over 360° for b) and c).

For us the task is to measure the sample from many directions, evenly spaced over one hemisphere. This can be done in multiple ways, the easiest being a full rotation over 360°

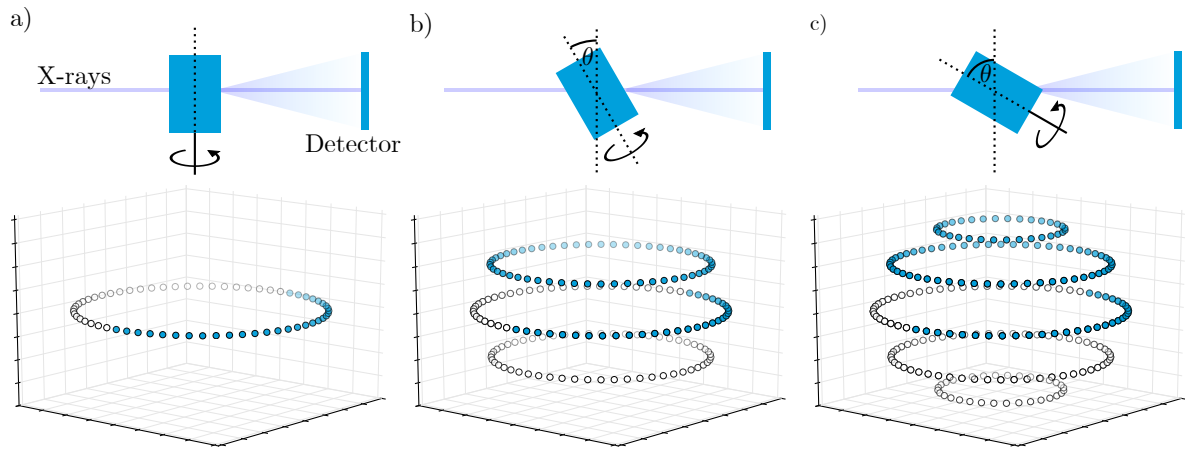


Figure 5.2: **Effect of an additional axis of rotation.** a) Standard CT acquisition scheme with a rotation from 0° to 180° . In this visualization the sample is assumed to be at the origin of the coordinate system and every point represents the position of the detector for one single measurement. The filled point show the measured data, the empty points show the mirrored points. For a standard CT geometry, a rotation over more than 180° does not yield additional data. The rotation axis is tilted by b) $\theta = 30^\circ$ and c) $\theta = 60^\circ$. The points from the previous panels are kept in b) and c) for reference. A full rotation over 360° is shown. In contrast to the case without tilting, the second half of the rotation yields additional information.

of φ , and a tilt angle up to $\theta = 90^\circ$. Generally, there is no practical restriction on φ , and a rotation over 360° is almost always possible. Therefore, an acquisition scheme with a full 360° rotation is preferred as it keeps the required range of θ to a minimum.

5.2 6-D SAXS-CT experiment

A 6-D SAXS-CT experiment was performed at the coherent small-angle X-ray scattering (cSAXS) beamline of the Swiss Light Source (SLS) in Villigen, Switzerland (www.psi.ch/sls/csaxs/). The cSAXS beamline is optimized for performing X-ray diffraction-based imaging experiments using a highly focussed beam and rapid acquisition. A detailed description of the experiment is given in this section.

5.2.1 Tooth sample

A sample to demonstrate the technique of 3-D SAXS-CT should ideally consist of an anisotropic nano-structure that changes over the entire volume of the sample. Bone [Fratzl, 1997; Rinnerthaler, 1999] and teeth [Kinney, 2001; Märtens, 2010; Gaiser, 2012]

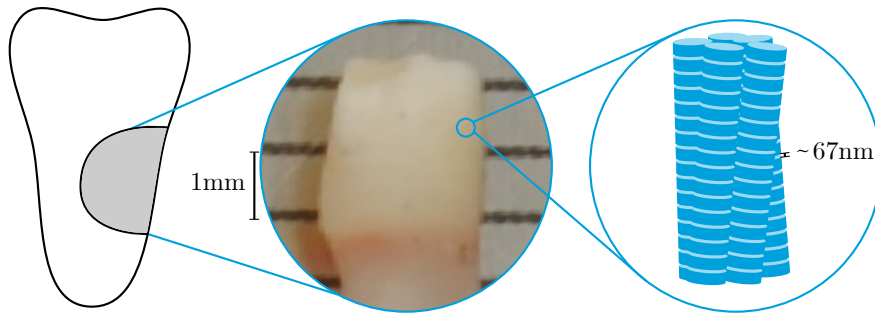


Figure 5.3: **Tooth sample.** A cylindrical segment was extracted from an upper lateral incisor for a 6-D SAXS-CT measurement. Teeth are mainly composed of mineralized collagen-fibrils, which are aligned in approximately the same direction on a microscopic level. Macroscopically, the orientation of the collagen fibrils depends on the region of the tooth. Collagen fibrils are made up from collagen molecules that are arranged with a distinctive period of roughly 67 nm.

are largely composed of mineralized collagen fibrils. The size of collagen fibrils is in the range of a few hundred nanometres, which severely hinders characterization of the collagen nano-structure over a large volume [Fratzl, 2007]. On a molecular level, these fibrils are made up of individual collagen molecules, which are long chains of approximately 300 nm length and 1.5 nm diameter [Fratzl, 2007]. Collagen molecules self-assemble and are arranged in a staggered way that leaves gaps of approximately 67 nm along the long axis of the resulting fibrils [Fratzl, 2007; Su, 2014]. A bundle of collagen fibres is sketched in figure 5.3. In mineralized tissue, such as bone and teeth, these gaps are filled by hydroxyapatite crystals [Fratzl, 2007]. Furthermore, collagen fibrils within tissue are not oriented randomly, but rather along a preferred orientation. The combination of a large electron density contrast, the orientational alignment of the fibrils, and the high periodicity within the structures gives rise to a very distinct SAXS signal. Owing to this, scanning SAXS is very suited for the characterization of collagen-based materials, and has expanded our knowledge about the nano-structure of bone and teeth substantially [Fratzl, 1997; Rinnerthaler, 1999; Kinney, 2001; Märten, 2010; Gaiser, 2012].

From previous studies on two-dimensional slices of teeth it is known that the preferred orientation of the collagen fibrils strongly depends on the position within the tooth [Kinney, 2001; Märten, 2010; Gaiser, 2012]. Mechanical properties of teeth are greatly influenced by the nano-structural arrangement of collagen fibres [Kinney, 2001]. Knowledge of the local nano-morphology can therefore be used to improve our understanding of the complex materials that teeth are composed of.

For these reasons we chose to demonstrate 3-D SAXS-CT on a tooth sample. A cylindrical segment of a human upper lateral incisor sample was kindly provided by Dr. Paul Zaslansky. The sample is approximately 2.5 mm in diameter and 3 mm in height and originates from a region beneath the tooth crown within the root. It was extracted from the buccal

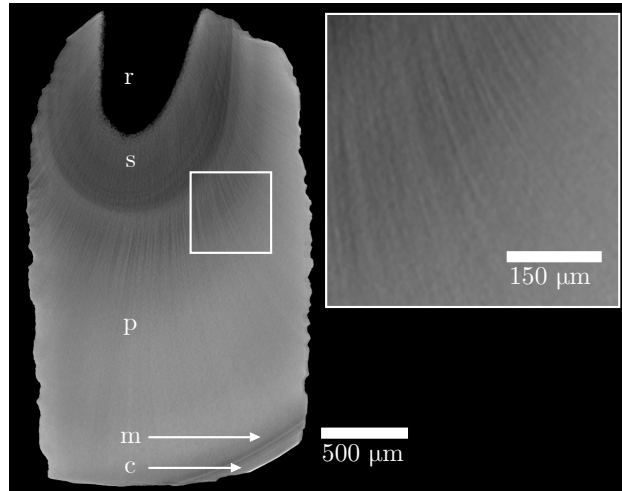


Figure 5.4: **Micro-CT slice of the tooth sample.** The average density in a slice from the centre of the sample is shown. Several different dental tissues are present in the sample. The surface of the tooth is covered by cementum (c). The root canal (r) in the centre of the tooth is surrounded by secondary dentine (s), primary dentine (p), and mantle dentine (m). The voxel size of the reconstruction is $3.087\ \mu\text{m}$, which is much larger than the size of collagen fibres.

side of the tooth (facing the lip) using water-cooled dental drills. The tooth was provided by an anonymous donor with written informed consent, according to the directives of the Ethical Review Committee of the Charité - Universitätsmedizin Berlin (EA4/002/09). A photograph image of the sample is shown in figure 5.3. The region inside the tooth from where the sample was extracted is marked.

A high-resolution micro-CT of the sample with $3.087\ \mu\text{m}$ voxel size was generated using a state-of-the-art VersaXRM-500 X-ray microscope. Although the data shown in figure 5.4 is of high quality, detailed information about the collagen nano-structure remains out of reach. Nonetheless, this image provides an overview of the different kinds of dental tissues found in the sample. The root canal (r) is encased by secondary dentine (s). Primary dentine (p) makes up the largest part of the sample. Thin layers of mantle dentine (m) and cementum (c) are found near the surface of the tooth. All these tissues are composed of mineralized collagen fibres. The goal of 6-D SAXS-CT is a three-dimensional characterization of the nano-structure and to provide a better picture of differences between the various tissues.

5 Six-dimensional small-angle X-ray scattering computed tomography

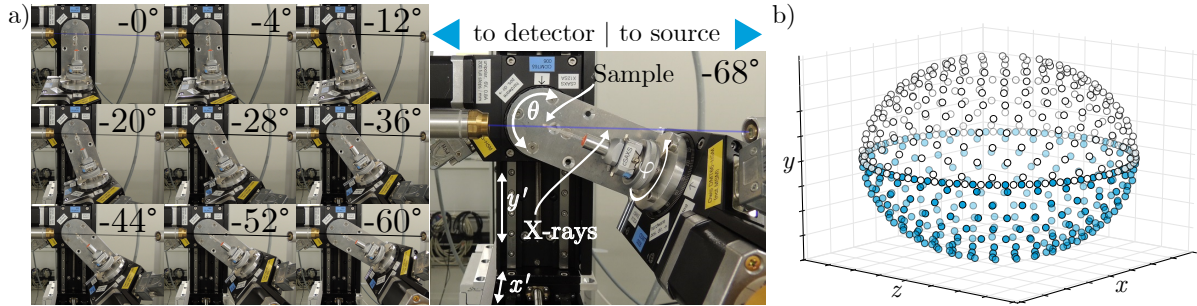


Figure 5.5: **Sample orientations measured for 6-D SAXS-CT.** a) Overview of the ten different tilt-angles θ used during the tooth measurement. Various components of the experimental setup can be identified in the magnified image. The sample is mounted on top of a glass capillary, centred on both axes of rotation, φ and θ . During the measurement, the sample is raster scanned through the X-ray beam along x' and y' . Given that for $\theta = -68^\circ$ the sample stage almost blocks the X-ray beam, higher θ could not be used. b) Visualization of the orientation for all measured P_j on the unit sphere as filled dots. For clarity, the points are mirrored at the origin.

5.2.2 Data acquisition

X-rays for the cSAXS beamline are generated with an in-vacuum undulator in a straight section of the Swiss Light Source. An arrangement of slits, mirrors and a monochromator provides a monochromatic, focussed X-ray beam at the sample position. The 6-D SAXS-CT experiment was conducted with a photon energy of 18.6 keV. The beam size at the sample position was approximately $50 \mu\text{m} \times 50 \mu\text{m}$. An evacuated flight-tube was installed between the sample and detector to reduce parasitic air scattering. The SAXS signal was collected using a PILATUS 2M photon counting detector with a silicon sensor, placed 7363 mm downstream of the sample [Eikenberry, 2003]. PILATUS detectors by design have no background noise, which greatly helps with the detection of weak signals, as typically encountered in scattering experiments. This makes these kind of detectors one of the best choices for scattering experiments. A beamstop was installed inside the flight tube to protect the detector from the very intense direct X-ray beam. In addition, a diode was mounted directly on the beamstop, which simultaneously recorded the intensity of the direct beam for each SAXS pattern.

The tooth sample was mounted on top of a glass capillary, as seen in figure 5.5. During the measurement, the sample was raster scanned with a step size of $50 \mu\text{m}$, i.e. matching the size of the beam, in x' - and y' -direction. A continuous raster scan was employed in x' -direction. Instead of moving the sample to a position and recording a SAXS pattern, the sample was moved through the X-ray beam at a constant speed, and SAXS patterns were recorded after every $50 \mu\text{m}$ sample movement. The resulting scanning SAXS images consist of 59×81 SAXS patterns. Each individual SAXS pattern was taken with an

θ	0°	-4°	-12°	-20°	-28°	-36°	-44°	-52°	-60°	-68°
N_φ	55	29	29	29	29	29	29	25	19	15
Offset	0	0	6.2°	0	6.2°	0	6.2°	0	6.2°	0

Table 5.1: **Combinations of the measured rotations.** For every tilt of the tomography axis θ , scanning SAXS projections were recorded for N_φ values of φ , evenly distributed over 360° . An offset was added to the values of φ for several tilt angles θ .

exposure time of 50 ms. The exposure time was chosen so that the first characteristic collagen peak can clearly be seen in the individual SAXS patterns (cf. figure 5.6). To outline the similarity of scanning SAXS to regular imaging, we shall call the set of SAXS patterns from a fixed sample orientation as projection P_j from here on. Keep in mind that each P_j contains four-dimensional data, owing to the two-dimensional SAXS pattern recorded at each point. In total, 288 different P_j were recorded. For each of these the sample was rotated by a unique combination of φ and θ . Figure 5.5 visualizes the different rotations during the measurement. We chose ten tilt angles θ of the original rotation axis up to $\theta = -68^\circ$. Any rotation of θ beyond this value would have caused the sample stage to move in front of the beam and render measuring impossible. The number of different φ measured for each tilt of the rotation axis, N_φ , is given in table 5.1. For each θ , scanning SAXS projections were recorded in x' and y' direction for N_φ positions of φ , evenly spaced over a full rotation of 360° . Given that points are sampled much denser for high θ , N_φ decreases with increasing θ . An offset of 6.2° to the values of φ was implemented for several θ . This aims at improving the spatial distribution of the measured orientations of the sample. A visualization of beam direction in the sample reference frame, \mathbf{t} , for all P_j according to the method introduced in chapter 3.3.2 is given in figure 5.5 b). Orientations for P_j and their mirrored counterparts are shown as filled and empty circles, respectively. It is clear to see that the conventional rotation axis, represented by points on the equator, is sampled much finer than all other orientations on the sphere. There was excess time at the end of the measurement so that a much larger number of angles could be measured for $\theta = 0$ (cf. table 5.1). Additionally, as the mirrored information lies on the same trajectory, the density of measured points is furthermore increased by a factor of two. In total, 1,376,352 SAXS patterns were collected in slightly under 40 h.

5.3 Data processing

Before we turn our attention to the actual reconstruction, the recorded data has to be brought to a usable form. This section describes the vital processing performed on the raw data. Each step is visualized using real data from the experiment.

5 Six-dimensional small-angle X-ray scattering computed tomography

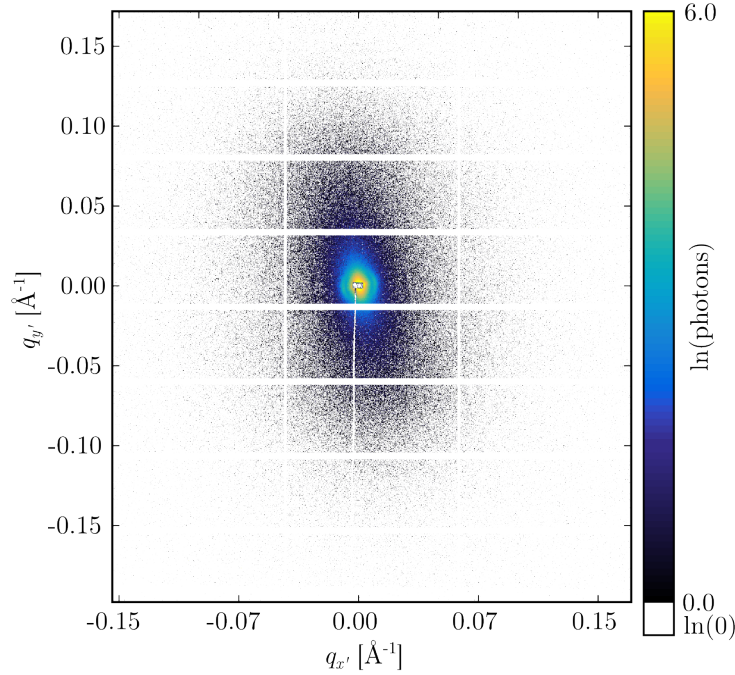


Figure 5.6: **Raw PILATUS 2M image.** A SAXS pattern from collagen can be seen in the center. The white horizontal and vertical stripes are dead areas of the detector. A magnified version of the cropped central part is shown in figure 5.7 a).

5.3.1 Cropping & azimuthal integration

A single SAXS pattern of the tooth sample as recorded by the PILATUS 2M detector is shown in Figure 5.6. As the SAXS signal covers several orders of magnitude, the natural logarithm of the total amount of photons scattered onto each pixel is used. A PILATUS 2M detector consists of 1475×1679 pixels in horizontal and vertical direction, respectively. Several parts of the detector cannot be used to record scattering information. Some of these pixels are physical gaps in the detector between individual modules, which leads to horizontal and vertical lines of missing data in the image. Additionally, the beamstop and the needle it is mounted on block the central part of the SAXS pattern, as well as a thin vertical part. With the experimental parameters used in the experiment, scattering information for scattering vectors $|\mathbf{q}| < 0.15 \text{\AA}^{-1}$ was recorded. However, all relevant information for the experiment is contained in the central region of the detector. Hence, only the central 225×225 pixels of the detector were used in the data analysis. A magnified version of the cropped central part is shown in figure 5.7 a). One striking feature of a collagen SAXS pattern can be seen in the form of two arcs around $|\mathbf{q}| \approx 0.01 \text{\AA}^{-1}$. These characteristic intensity peaks correspond to the 67 nm repetition period found in collagen fibrils. Furthermore, the SAXS pattern is clearly asymmetric, owing to the preferred

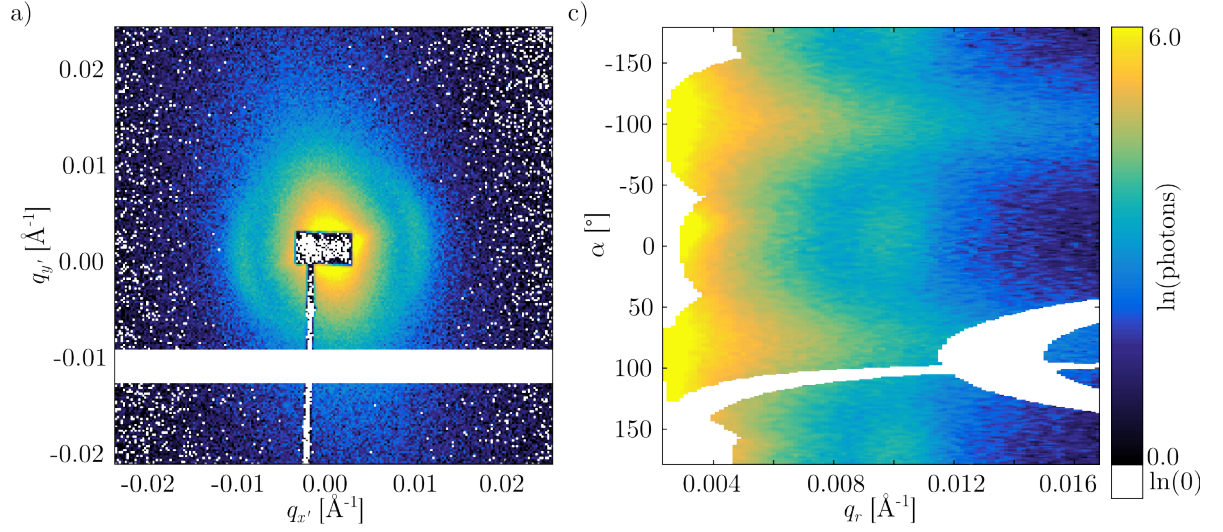


Figure 5.7: **Azimuthal integration.** a) The relevant SAXS data is contained entirely on a central segment of the detector and all images are cropped accordingly. b) Azimuthal regrouping of the scattering data to polar coordinates.

orientation of the underlying collagen fibrils.

Initially, the data is recorded in $q_{x'}-q_{y'}$ -coordinates. For further analysis a polar coordinate system with a radial coordinate q_r and an angular coordinate α is advantageous. Every SAXS pattern $I_i(q_{x'}, q_{y'})$ therefore was azimuthally regrouped to $I_i(q_r, \alpha)$. This was done using a python implementation for fast azimuthal integration, developed at the European Synchrotron Radiation Facility (ESRF) [Kieffer, 2013]. The source code is available from www.github.com/silx-kit/pyFAI. Figure 5.7 b) depicts how azimuthal integration transforms the cropped SAXS pattern, given in a). Scattering information for very small $q_r \approx 0$ that is blocked entirely by the beamstop is not shown. In this representation, the characteristic SAXS peaks of collagen can clearly be identified at $|\mathbf{q}| \approx 0.01 \text{ \AA}^{-1}$.

5.3.2 Summation of opposite scattering data

We recall from chapter 2.2 that the SAXS signal is symmetric around the origin, i.e. $I(\mathbf{q}) = I(-\mathbf{q})$. For this reason, we combine data from opposite \mathbf{q} -vectors. This has some practical advantages. Photon counting statistics is improved for every pair $I(\mathbf{q}) = I(-\mathbf{q})$, while at the same time the absolute amount of data is reduced by a factor of two. It should be noted that increased photon statistic is not achieved when one part of pair is blocked by either a PILATUS gap or the beamstop, so-called dead areas of the detector. Furthermore we can restrict our analysis to $0^\circ \leq \alpha < 180^\circ$. With the data regrouped to polar coordinates, a combination of opposing scattering data is easily realized as a simple summation $I_i(q_r, \alpha) + I_i(q_r, \alpha + 180^\circ)$ for $0^\circ \leq \alpha < 180^\circ$.

Figure 5.8 a) shows the data given in 5.7 b) reduced to $\alpha < 180^\circ$. The effect of missing

5 Six-dimensional small-angle X-ray scattering computed tomography

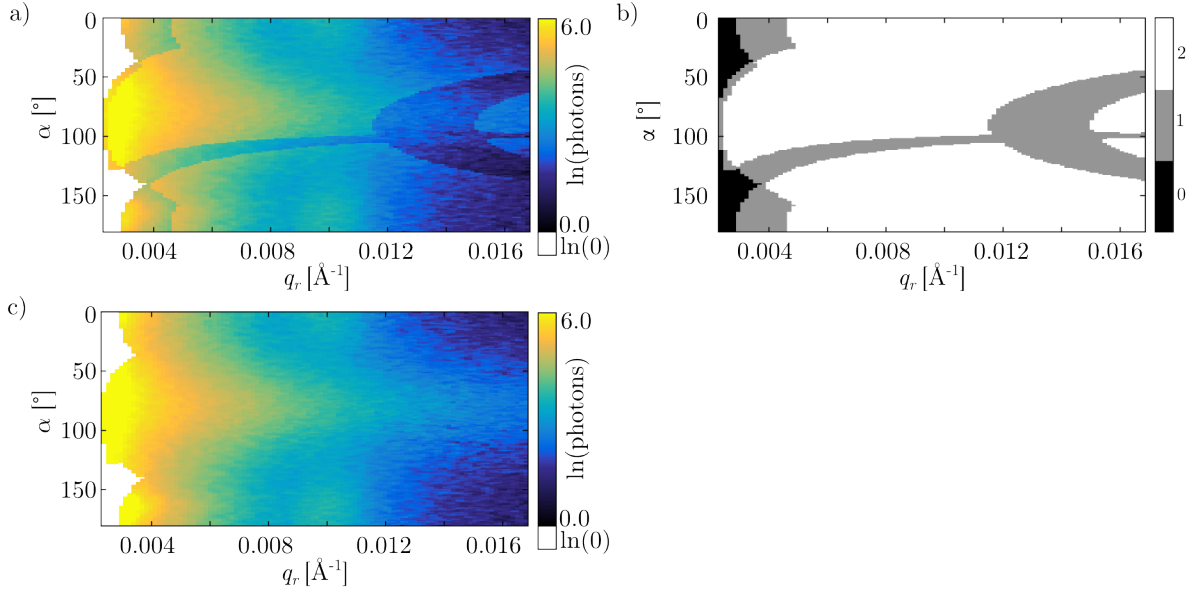


Figure 5.8: **Combination of data from opposing q-vectors.** a) The summation of $I_i(q_r, \alpha) + I_i(q_r, \alpha + 180)$. Missing data caused by gaps in the detector and the beamstop remains in the image as visible artefacts. This is fixed with help of a mask that contains all dead pixels. b) Summation of the azimuthally integrated mask. c) Dead-area corrected image.

data due to dead areas on the detector is clearly visible. All $I_i(q_r, \alpha)$ for which one of the two summands corresponds to a dead area obviously has a lower combined intensity. Identifying the amount of non-zero contributions for each $I_i(q_r, \alpha)$ can easily be done using a mask that contains only the dead-areas of the detector. The azimuthally integrated and reduced mask is shown in figure 5.8 b). The result in a) is corrected for the effect of dead-areas by division with the mask image in b). Division by 0 obviously is not allowed, however, this only affects areas in which no useful information is contained in the first place. The result of the dead-area correction is shown in c). At this point, the data for each SAXS pattern now is in reduced polar coordinates.

5.3.3 Attenuation normalization

Correction for attenuation is the most crucial step of data processing. In chapter 4.6.3, it was derived that attenuation of the SAXS signal prior to and post scattering is equivalent and can be treated simultaneously. Attenuation data exists in the form of a single diode intensity measurement of the direct beam, d_i , for every measured SAXS pattern I_i . Correction for attenuation is readily performed as:

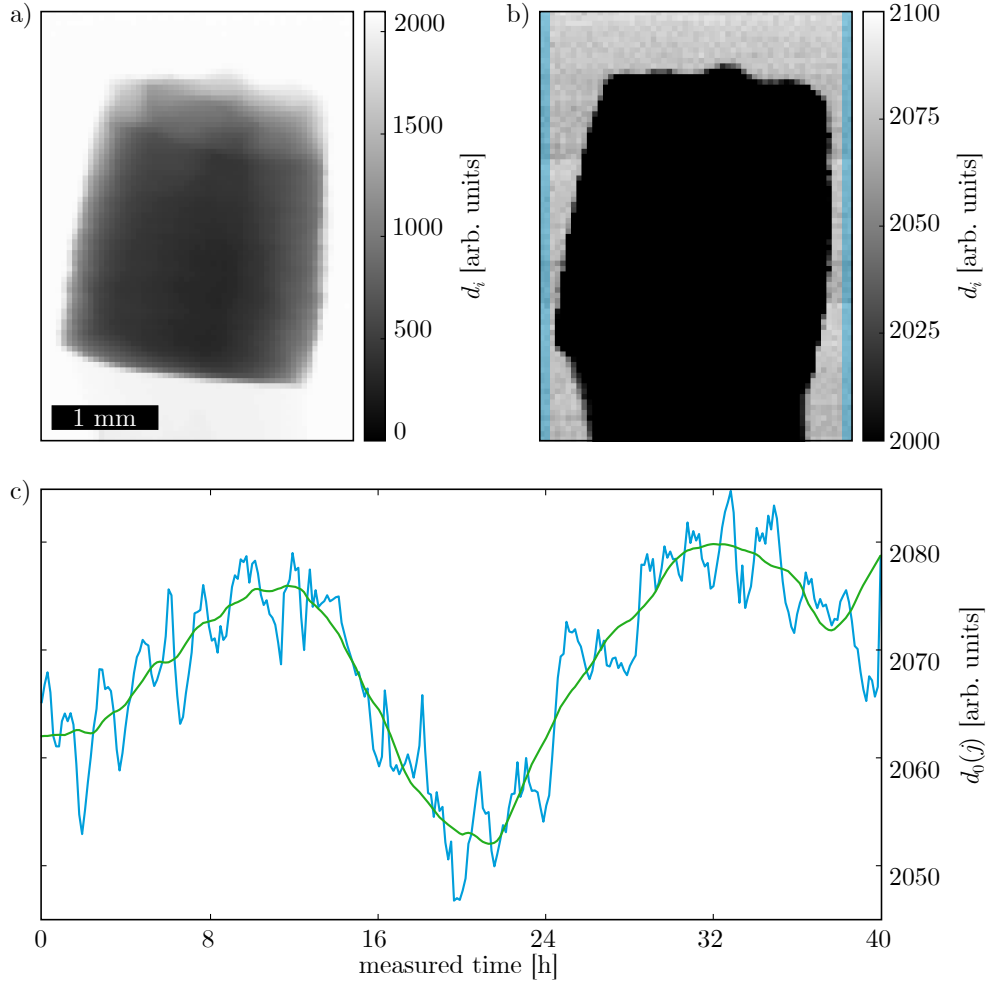


Figure 5.9: **Determination of beam intensity.** a) Attenuation image generated from diode data. b) Periodic Intensity fluctuations are revealed by narrowly scaling the image. The areas highlighted in blue serve as a reference. c) The average value of the reference areas plotted against the measured time. A daily variation is visible. The data is smoothed by a Savitzky-Golay filter.

$$I_i^{\text{corr}}(q_r, \alpha) = I_i(q_r, \alpha) \frac{d_0}{d_i}. \quad (5.1)$$

Here, d_0 is the diode intensity measured without attenuation. Ideally, d_0 is a constant throughout the entire measurement. However, the intensity of the synchrotron beam fluctuates slightly over time. Figures 5.9 a) and b) show an image generated from all diode measurements d_i of one P_j . The result is a conventional attenuation based X-ray image. We recall that the sample was scanned in vertical lines. One way to obtain d_0 for every measurement is to take the diode measurements d_i at the start and end of every scan-

line as d_0 for that line. These points generally do not contain sample information, and are shaded blue in b). The tight window in b) reveals short-term fluctuations of the beam that can be seen as vertical lines in the areas without sample. This is caused by the periodic replenishment of the electron-beam stored inside the synchrotron. This may occur at any point of a scan-line and without a constant beam monitor that yields $d_0(i)$ for every d_i , a correction of short-term fluctuations is difficult. As such a device was not available we took an average $d_0(j)$ for every projection j as the mean over all start and end-points of the scan-lines. Figure 5.9 c) shows a plot of $d_0(j)$ over the entire duration of the measurement. A long-term fluctuation over 24 h can be seen, as well as a certain periodicity on a time-scale of hours. The latter is caused by the way $d_0(j)$ is calculated and related to the short-term fluctuations. Depending on the exact times of beam replenishment, $d_0(j)$ is biased to higher or lower values. We can therefore only reliably correct for the long-term fluctuations of the beam. This was done using a Savitzky-Golay filter to smooth the data, and take the resulting curve as $d_0(j)$.

Additionally, the attenuation data was used to correct for relative shifts between the individual projections with respect to each other [GuizarSicairos, 2015].

5.4 Reconstruction of the local scattering cross section

The approach for reconstructing $\left(\frac{d\sigma}{d\Omega}\right)(\mathbf{q}, \mathbf{r})$ presented here revolves around splitting the complete reconstruction into several smaller, independent reconstructions. This is done by using the rotational invariance of the SAXS signal under certain conditions, as introduced in chapter 4.6.

5.4.1 Quantification of rotational invariance for conventional SAXS-CT

A method to quantify rotational invariance of scattering data for the standard CT case was given by Feldkamp [Feldkamp, 2011, pp. 82-89]. For now we restrict ourselves to all P_j with $\theta = 0$. This subset of projections is what would be measured for a standard CT around the y' -axis. The weight $\omega_{j,y'}$ for one line at height y' of a projection P_j with N measurements in x' is defined as [Feldkamp, 2011, p. 83]:

$$\omega_{j,y'}(q_{x'}, q_{y'}) = \sum_{x'=0}^N P_j(x', y', q_{x'}, q_{y'}). \quad (5.2)$$

This definition stems from the idea that during a tomographic measurement, information is redistributed within a plane perpendicular to the tomographic axis, in our case the $x' - z'$ -plane at a given height y' . Integration in z' -direction is performed by the X-ray projection. The summation over all scattering patterns recorded at height y' therefore gives the integrated scattering signal for each projection. This value must be constant

5.4 Reconstruction of the local scattering cross section

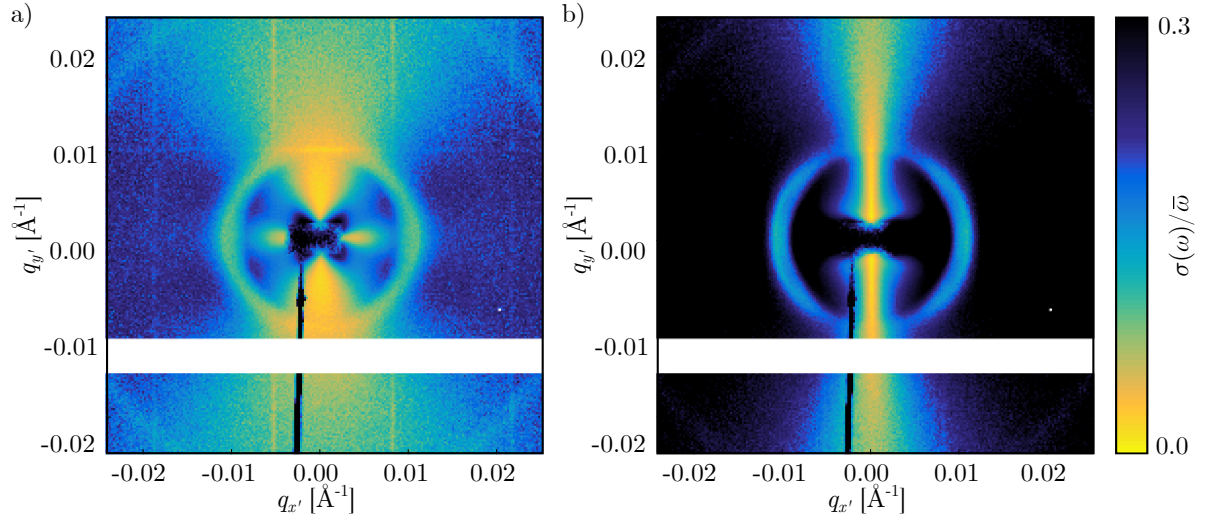


Figure 5.10: **Rotational invariance for conventional SAXS-CT.** The ratio $\sigma(\omega)/\bar{\omega}$ is used to quantify how strong the scattering data in each pixel changes with rotation. The metric is calculated for a slice from the upper (a) and lower half (b) of the tooth sample. Low values correspond to rotational invariant data, which is generally only seen for scattering parallel to the rotation axis during the CT measurement, vertical here.

under rotation for a signal that is rotationally invariant. Let us restrict ourselves to a single $y' = \text{const.}$. For each pixel of the detector, and therefore recorded scattering vector, we calculate the mean weight $\bar{\omega}$ and standard deviation of the weights $\sigma(\omega)$. This is done for a total number of J different P_j as [Feldkamp, 2011, pp. 83-84]:

$$\bar{\omega} = \frac{1}{J} \sum_{j=0}^J \omega_j. \quad (5.3)$$

$$\sigma(\omega) = \sqrt{\frac{1}{J} \sum_{j=0}^J (\omega_j - \bar{\omega})^2}. \quad (5.4)$$

A quantitative value for the rotational invariance of the scattering signal in each pixel is then calculated as the relative standard deviation $\sigma(\omega)/\bar{\omega}$.

The rotational invariance measure for scattering data recorded around a vertical rotation axis is showcased in Figure 5.10. The measure is calculated for two slices of the measured tooth sample at different y' from the subset including all projections with $\theta = 0$. A high value of $\sigma(\omega)/\bar{\omega}$ corresponds to a scattering signal that changes strongly under rotation. The scattering information recorded in pixels with a small value of $\sigma(\omega)/\bar{\omega}$ can be considered rotationally invariant, which is only the case for the vertical direction. This is

exceptionally clear in b). Certain symmetries of the scattering structures provide rotational invariant signals in a) for pixels not corresponding to vertical scattering vectors. This, however, is just coincidentally. General rotational invariance of the signal is only true for the vertical direction.

5.4.2 Virtual tomography axes

The concept of rotational invariance tells us that it is always possible to reconstruct the scattering vectors parallel to the rotation axis \mathbf{a} . Furthermore, the reconstruction of a single \mathbf{q} -vector is performed independent from all others. This allows us to reconstruct a scalar value in each individual reconstruction, and all well-understood theory on CT can be applied.

As scattering vectors parallel to a rotation axis can be reconstructed, a straight-forward reconstruction of $\left(\frac{d\sigma}{d\Omega}\right)(\mathbf{q}, \mathbf{r})$ can be implemented by simply recording CT data sets for multiple rotation axes \mathbf{a}_k . Each of the individual CT data sets then contributes scattering vectors $\mathbf{q} \parallel \mathbf{a}_k$ to the complete reconstruction of $\left(\frac{d\sigma}{d\Omega}\right)(\mathbf{q}, \mathbf{r})$. While this in theory is possible, practical limits are quickly reached. SAXS-CT measurements are very time consuming and only a limited number of projections can be recorded. As an example, it took over seven minutes to record a single projection P_j of the tooth sample. Computed tomography requires several P_j to be recorded for each \mathbf{a}_k , which ultimately limits the investigation to a small amount of tomography axes. The main drawback of this method rests on the highly inefficient way of using data. Only $\mathbf{q} \parallel \mathbf{a}_k$ are used in the reconstructions. This is only a tiny fraction of the measured data and a large part of all SAXS patterns would be discarded.

A more efficient way of using data therefore is required in order to facilitate a direct reconstruction using the concept of rotational invariance. Here we introduce the concept of virtual tomography axes as a method to use the recorded data in a highly efficient way. Instead of directly measuring a large amount of CT data sets, we measure many projections distributed over half the unit sphere, as described in section 5.2. The reconstruction of $\mathbf{q} \parallel \mathbf{a}_k$ is performed not by measuring a CT data set around \mathbf{a}_k , but rather by selecting those P_j that form a CT data set around the virtual tomography axis \mathbf{a}_k . This technique allows us to reuse the data contained in a single P_j for multiple \mathbf{a}_k . Owing to this, a substantially more efficient usage of the recorded data is achieved.

The basic idea of virtual tomography axes is visualized in figure 5.11. Several P_j recorded for different combinations φ, θ are shown. Three different virtual tomography axes, $\mathbf{a}_1, \mathbf{a}_2, \mathbf{a}_3$, are sketched within the sample. The blue axis, \mathbf{a}_1 , corresponds to the standard CT case. All P_j that form a CT data set around \mathbf{a}_1 are marked by blue arrows accordingly, which also indicates the direction of $\mathbf{q} \parallel \mathbf{a}_1$. Let us now consider another axis, \mathbf{a}_2 . First of all, we realize that different P_j are required to form a CT data set around \mathbf{a}_2 . These P_j are indicated by green arrows accordingly, which also show the orientation of $\mathbf{q} \parallel \mathbf{a}_2$ for this set of P_j . One P_j is contained both in the blue and green data sets. However, different

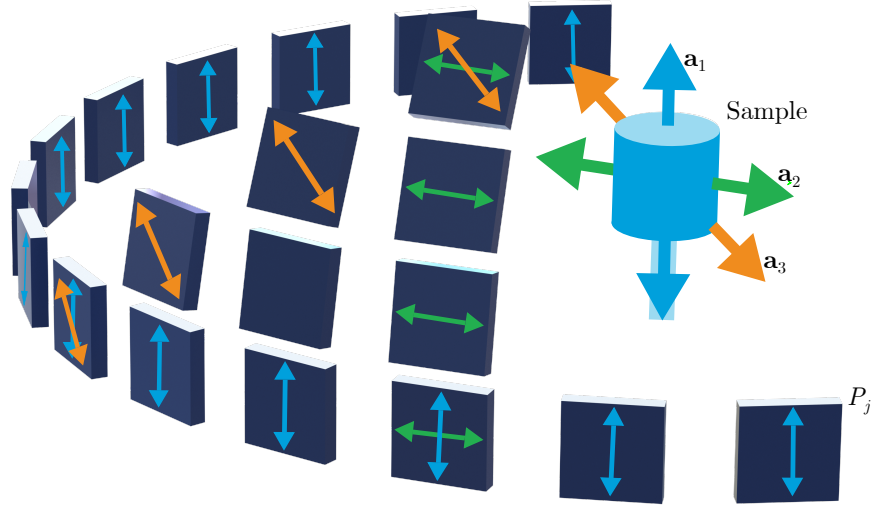


Figure 5.11: **Concept of virtual tomography axes.** SAXS-projections P_j of a sample are recorded from all directions. For an arbitrary axis within the sample, a subset of all P_j that resembles a conventional CT measurement around that axis is used to reconstruct the scattering information parallel to that axis. Three different virtual tomography axes \mathbf{a} are shown by three different colours. Only scattering data parallel to \mathbf{a} is used for the respective tomographic reconstruction. This is indicated by the direction of the arrows on each P_j . As one P_j is used for multiple subsets the amount of data required for a full reconstruction is reduced substantially.

parts of the scattering information are used for the reconstructions. We are therefore able to use the data contained in a projection P_j for more than one \mathbf{a}_k .

Another way to look at this is to consider the following. In order to reconstruct $\left(\frac{d\sigma}{d\Omega}\right)_{\mathbf{q}}(\mathbf{r})$ for a certain \mathbf{q} , we look for those P_j that record scattering information for \mathbf{q} . We uniquely denote the pose of P_j by the direction of the incident beam \mathbf{t}_j . In sample coordinates it is given as

$$\mathbf{t}_j = \mathbf{R}^{-1}(0, 0, 1)^\top, \quad (5.5)$$

with the rotation matrix \mathbf{R}_j^{-1} . As the measured SAXS signal is perpendicular to the incident beam, any P_j for which

$$\mathbf{q} \cdot \mathbf{t}_j = 0 \quad (5.6)$$

contains scattering data for \mathbf{q} . As only a limited amount of P_j can be sampled within reasonable time, it is highly unlikely that the condition of equation 5.6 is exactly met. We use the fact that the SAXS signal does not exhibit sharp peaks and is rather slowly

5 Six-dimensional small-angle X-ray scattering computed tomography

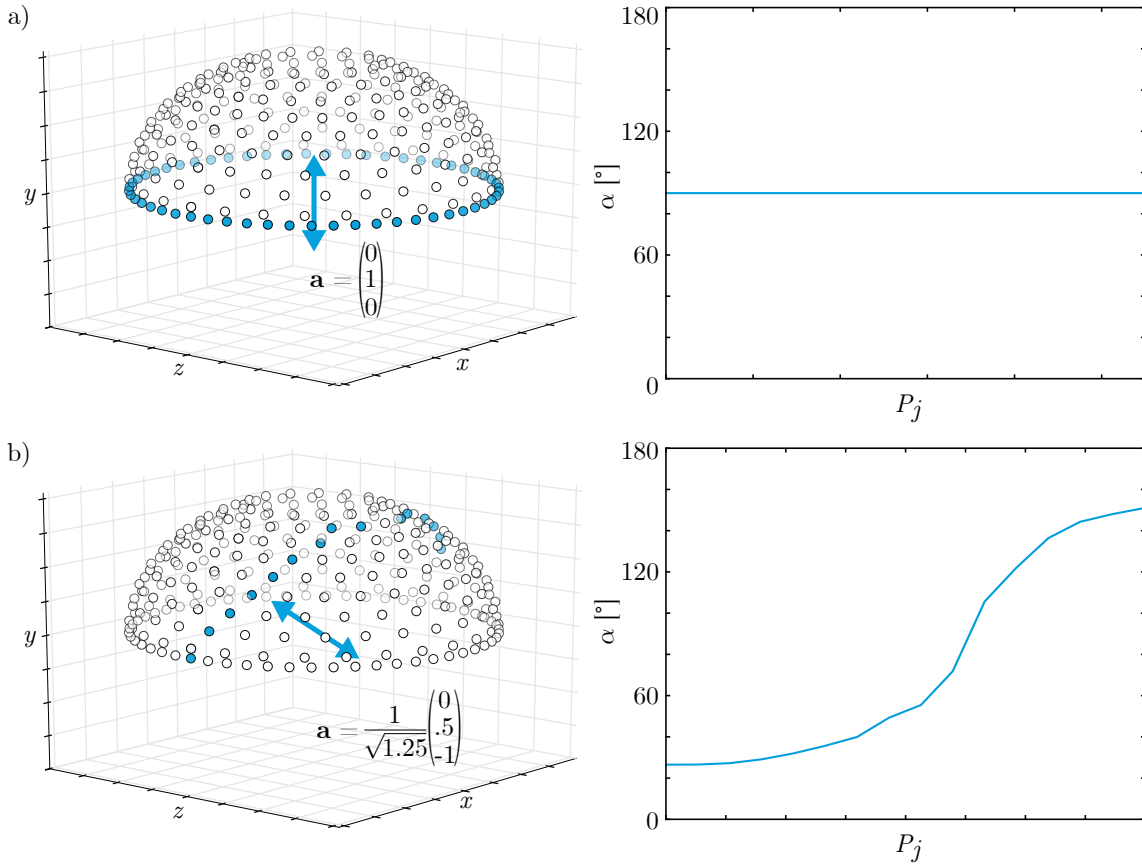


Figure 5.12: **Data selection for virtual tomography axes.** All projections recorded for the tooth measurement are shown (upper hemisphere for clarity). Subsets around two virtual tomography axes $\mathbf{a} = (0, 1, 0)^\top$ (a) and $\mathbf{a} = 1/\sqrt{1.25}(0, .5, 1)^\top$ (b) are highlighted as filled spheres. Those projections are used to reconstruct scattering vectors parallel to the respective axis \mathbf{a} . Only scattering data parallel to \mathbf{a} is rotationally invariant and can be used in a simple reconstruction. The azimuthal coordinate α for which the scattering data is parallel to \mathbf{a} is plotted against P_j for both data sets.

5.4 Reconstruction of the local scattering cross section

varying, contrary to e.g. crystal diffraction. This approximation holds for nearly all materials investigated with SAXS, and we can therefore relax the condition to

$$0 < |\mathbf{q} \cdot \mathbf{t}_j| \ll 1. \quad (5.7)$$

This approximation allows us to ensure a sufficient amount of P_j is used for each reconstruction. As a consequence of equation 5.7, nearly perfectly crystalline objects are not suited for the presented method.

After having identified all $\{P_j \mid 0 < |\mathbf{q} \cdot \mathbf{t}_j| \ll 1\}$, we need to figure out the coordinates q_r, α of \mathbf{q} in the recorded data for every P_j . Owing to the small discrepancy introduced with equation 5.7 we use the projection of \mathbf{q} onto the detector plane, $\mathbf{q} - (\mathbf{q} \cdot \mathbf{t}_j)\mathbf{t}_j$. Using the appropriate rotation matrices \mathbf{R}_j , this two-dimensional vector can be transformed into laboratory coordinates and polar form to comply with the notation used for the recorded intensity, $I(q_r, \alpha)$. Note that the azimuthal coordinate α depends on \mathbf{q} and \mathbf{t}_j , and therefore both on \mathbf{a}_k and P_j . This dependence is illustrated in figure 5.12. All P_j measured for the tooth sample are shown, mirrored to the upper hemisphere for clarity. The subsets of P_j for $\mathbf{a} = (0, 1, 0)^\top$ and $\mathbf{a} = 1/\sqrt{1.25}(0, .5, 1)^\top$ are shown as filled circles in a) and b), respectively. The azimuthal coordinate, α , which contains scattering data parallel to \mathbf{a} is plotted against P_j . Owing to the way the data are recorded, α is constant for the case of a conventional CT axis, as presented in a). For other \mathbf{a} , α depends on P_j , as evident in b).

5.4.3 Quantification of rotational invariance for virtual tomography axes

In section 5.4.1, we presented a method to quantify rotational invariance for a given set of CT data. The goal here is to expand that concept to non-standard rotations. First of all, owing to the additional rotation, movement of individual parts of the sample is not restricted to the plane perpendicular to a single rotation axis. This makes a slice-by-slice investigation not possible any more. We therefore cannot define a weight for each vertical line of the sample as given in equation 5.2. Instead we have to sum P_j along both real-space axes to obtain a weight ω_j for every P_j that consists of $N \times M$ SAXS projections:

$$\omega_j(q_r, \alpha) = \sum_{y'=0}^M \sum_{x'=0}^N P_j(x', y', q_r, \alpha). \quad (5.8)$$

This equation uses the polar form of detector coordinates, (q_r, α) . As the rotational invariant data is found for different α_j for each P_j , we need to account for this offset accordingly. Let $\alpha_{\text{RI},j}$ be the azimuthal variable, offset corrected so that the rotational invariant data falls onto $\alpha_{\text{RI},j} = 0$ for each P_j . With this we can calculate $\sigma(\omega)$ and $\bar{\omega}$. This allows us to quantify rotational invariance for any virtual tomography axis.

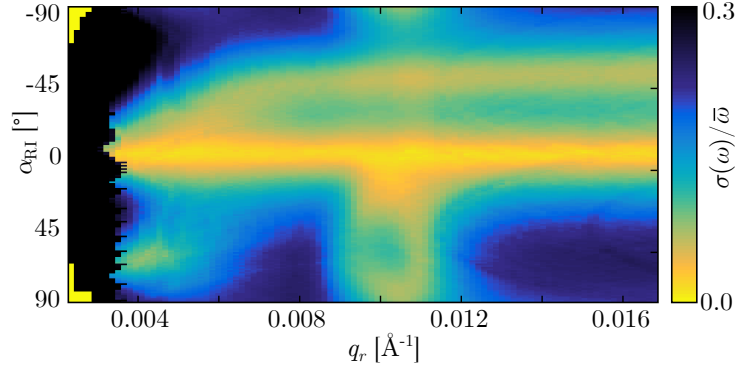


Figure 5.13: **Quantification of rotational invariance for virtual tomography axes.** Data of the tooth measurement for $\mathbf{a} = 1/\sqrt{2}(1, 1, 0)^\top$ is shown. Data for all P_j is offset corrected so that $\alpha_{\text{RI}} = 0$ corresponds to scattering vectors parallel to \mathbf{a} , for which high rotational invariance of the data can be seen.

Figure 5.13 presents an extended rotational invariance quantification for $\mathbf{a} = 1/\sqrt{2}(1, 1, 0)^\top$. It is clear to see that the ratio $\sigma(\omega)/\bar{\omega}$ is low for $\alpha_{\text{RI}} = 0$. This confirms that it is possible to extract rotational invariance data from projections with the help of virtual rotation axes.

5.5 Complete six-dimensional reconstruction

The previous section introduced all the tools we need for a complete reconstruction of $(\frac{d\sigma}{d\Omega})(\mathbf{q}, \mathbf{r})$. This section presents the results of a 6-D SAXS-CT reconstruction for the tooth sample.

5.5.1 Reconstructed scattering orientations

The question of how many and which \mathbf{a}_k to reconstruct still remains. This problem can be understood as finding a set of points that, ideally, are distributed isotropically over a hemisphere. Finding a uniform distribution of N_{pix} points on a (hemi-)sphere for $N_{\text{pix}} > 20$ is a non-trivial problem [Tegmark, 1996]. Similar problems occur in various fields of research, including the determination of protein shape [Morris, 2005], computer vision [Shao, 1996; Martinez, 2007] and diffusion magnetic resonance imaging [Bates, 2016]. For a large number of points, several approximations arose from pixelating the celestial sphere in astrophysics [Tegmark, 1996; Gorski, 2005].

For our case, the Hierarchical Equal Area isoLatitude Pixelisation (HEALpix) method used in astrophysics [Gorski, 2005] was used. It provides a quasi-isotropic distribution of points over the full unit-sphere. HEALpix distributions are scalable and see frequent use in astrophysics, owing to several advantageous mathematical properties [Gorski, 2005].

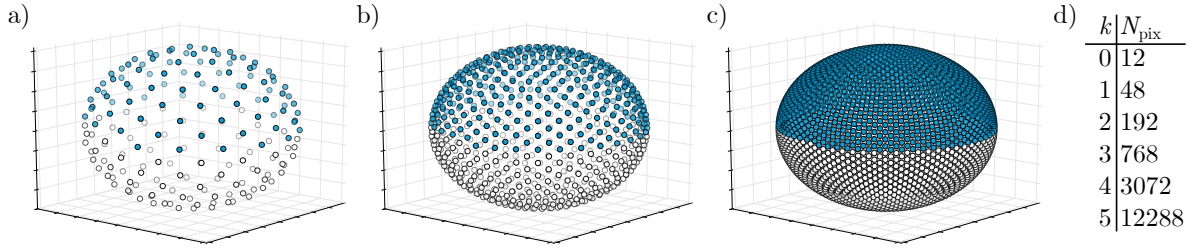


Figure 5.14: **HEALpix pixelation schemes.** Three HEALpix distributions with (a) $N_{\text{pix}} = 192$, (b) $N_{\text{pix}} = 768$ and (c) $N_{\text{pix}} = 3072$ points. The upper hemisphere is shown with filled dots. d) Dependence of N_{pix} on the resolution parameter k . The upper half of distribution (b) with $N = 768/2 = 384$ points was used for the 6-D SAXS-CT reconstruction.

Three HEALpix distributions for $N_{\text{pix}} = 192$, $N_{\text{pix}} = 768$ and $N_{\text{pix}} = 3072$ points are given in figures 5.14 a), b) and c), respectively. The total amount of points for a full distribution is given by a resolution parameter k . Figure d) presents a list of the number of points N_{pix} for the first six values for k . One drawback of the HEALpix distributions is revealed here. Although the amount of points can be modified by different k , only a discrete number of distributions are available.

For 6-D SAXS-CT, it is important to reconstruct a sufficient amount of scattering orientations. Reconstruction time and a finite resolution of the measured data serves as an upper limit for the amount of reconstructed orientations. As all HEALpix distributions are symmetric around the origin, we are only interested in half the points (one hemisphere). Therefore the final amount of points is half of that given in figure 5.14 d). Considering all of these points, the upper hemisphere of the distribution for $k = 3$, shown in figure 5.14 b), was used for the 6-D SAXS-CT reconstruction presented here. It consists of 384 orientations which served as a basis for the reconstructed scattering orientations \mathbf{a}_k .

5.5.2 Reconstructed radial segments

The complete reconstruction can be performed separately for all q_r . With the scattering data $I(q_r, \alpha)$ in polar coordinates, this is a trivial task. Scattering data was available from $q_r = 4.0 \times 10^{-3} \text{ \AA}^{-1}$ to $q_r = 16.8 \times 10^{-3} \text{ \AA}^{-1}$ in 44 discrete steps. This corresponds to structure sizes from 155.16 nm to 37.30 nm. As the raw data was recorded with a low exposure time, the radial segments were chosen to include data from several pixels, both in radial, as well as azimuthal direction. This reduces noise of the individual data points, at the cost of reciprocal space resolution. Given that the reconstruction technique already approximates in reciprocal space, binning adjacent data points does not have a substantial impact on the results.

5.5.3 SART-TV reconstruction

With 384 reconstructed orientations for 44 radial segments, the complete six-dimensional reconstruction consisted of 16896 independent reconstructions. Each of them yields the distribution of $\left(\frac{d\sigma}{d\Omega}\right)(\mathbf{q}, \mathbf{r})$ in real space for one specific \mathbf{q} -vector. A deviation $|\mathbf{q} \cdot \mathbf{t}_j| < 0.08$ was used to select appropriate P_j for each \mathbf{a}_k , which means that on average only about 15 P_j were suitable for a single \mathbf{a}_k . This is a very low amount of projections for a reconstruction of a volume with $81 \times 81 \times 81$ voxels. Additionally, owing to the limitations imposed by the measurement geometry, the available data does not cover a full 180° rotation for several \mathbf{a}_k . Most of the individual reconstructions therefore suffer from severe undersampling, as well as possible limited angle acquisition. Especially the latter rules out the use of filtered-back projection as a reconstruction method, which relies on evenly sampled data over 180° . For this reason, the reconstructions were performed using simultaneous algebraic reconstruction technique (SART) with total variation (TV) regularization [Rudin, 1992]. It has been shown that SART in combination with TV regularization is able to cope with both limited-angle problems, as well as undersampled data reasonably well [Sidky, 2009]. A SART-TV reconstruction was performed for each of the 16896 reconstructed \mathbf{q} -vectors. The regularization parameter for the TV step in every reconstruction was adjusted to the used sub-set of the data. This is necessary, as the scattered intensity strongly depends on q_r . In a final step, all partial results were combined into a single data set to obtain the complete reconstruction of $\left(\frac{d\sigma}{d\Omega}\right)(\mathbf{q}, \mathbf{r})$.

5.6 Analysis of the reconstructed data

The full reconstruction of $\left(\frac{d\sigma}{d\Omega}\right)(\mathbf{q}, \mathbf{r})$ is a six-dimensional data set. Given the complexity of the reconstructed data, an essential step to understanding the results is to extract and visualize information of interest from $\left(\frac{d\sigma}{d\Omega}\right)(\mathbf{q}, \mathbf{r})$. In this section, several different ways to work with $\left(\frac{d\sigma}{d\Omega}\right)(\mathbf{q}, \mathbf{r})$ are presented.

5.6.1 Consistency between reconstructed and measured data

First of all, let us verify the results by comparing them to the measured data. A forward projection of the reconstructed data on to the imaging plane according to the model presented in chapter 4.6 was calculated for P_j with $\theta = 0^\circ$ and $\varphi = 346.9^\circ$. Scattering data with $q_r = 9.0 \times 10^{-3} \text{ \AA}^{-1}$ were used for this analysis, as the peaks characteristic for collagen are found close to these scattering vectors. Two-dimensional images are created by further restricting the data to a single α . A side-by-side comparison of the reprojected results with the corresponding slice of the measured data is given in figure 5.15 b) and a), respectively. Each of the three pairs corresponds to scattering in a single direction, given by α and indicated by the arrows. Evidently, the images based on reconstruction results are much smoother than their measured counterparts. This is due to the reconstruction

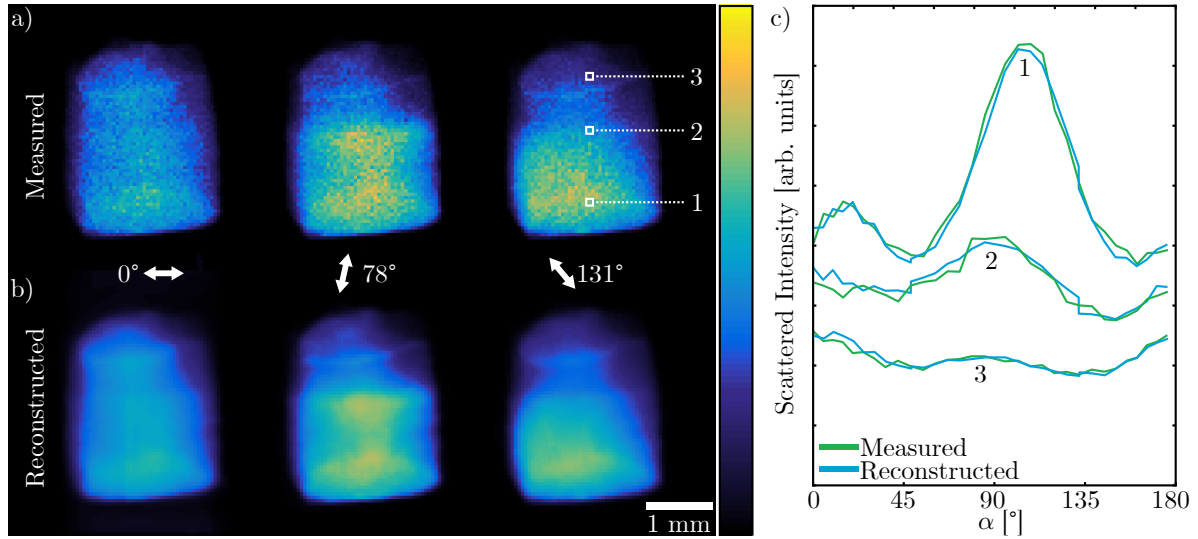


Figure 5.15: **Consistency between reconstructed and measured data.** a) SAXS projection generated from measured data with $q_r = 9.0 \times 10^{-3} \text{ \AA}^{-1}$ and $\alpha = 0^\circ, 78^\circ, 131^\circ$. The projection corresponds to sample rotation $\theta = 0^\circ$ and $\varphi = 346.9^\circ$. b) The same projections generated by reprojecting the reconstructed data onto the imaging plane. c) Plot of the measured and reconstructed scattering intensity for three points marked in a) against α . To reduce noise, the data were averaged over an area of 3×3 pixels for each point. Animation available at <https://www.youtube.com/watch?v=Zcxv94dW7H8>. 

and regularization used. Besides that, the similarity within the image pairs is clear. Subtle features of the intensity distribution are seen both in the measured and reconstructed data. To further showcase the correct reconstruction, a plot of the scattered intensity over α is given for three different points in c). The data were averaged over an area of 3×3 pixels which are indicated in a), to counteract noise. The three points were chosen to include structurally different parts of the sample. A strong correlation between the plots for measured and reconstructed data exists, which shows that the measured data are well described by the used model and the reconstruction approach.

5.6.2 Visualization of local cross sections

Visualizing $\left(\frac{d\sigma}{d\Omega}\right)(\mathbf{q}, \mathbf{r})$ in an understandable form is a difficult task. In a first step, we will restrict ourselves to the local cross section at discrete spatial positions \mathbf{r} within the sample, $\left(\frac{d\sigma}{d\Omega}\right)_{\mathbf{r}}(\mathbf{q})$. A very intuitive representation to anyone familiar with conventional SAXS patterns is to look at two-dimensional slices through $\left(\frac{d\sigma}{d\Omega}\right)_{\mathbf{r}}(\mathbf{q})$. Figure 5.16 presents

5 Six-dimensional small-angle X-ray scattering computed tomography

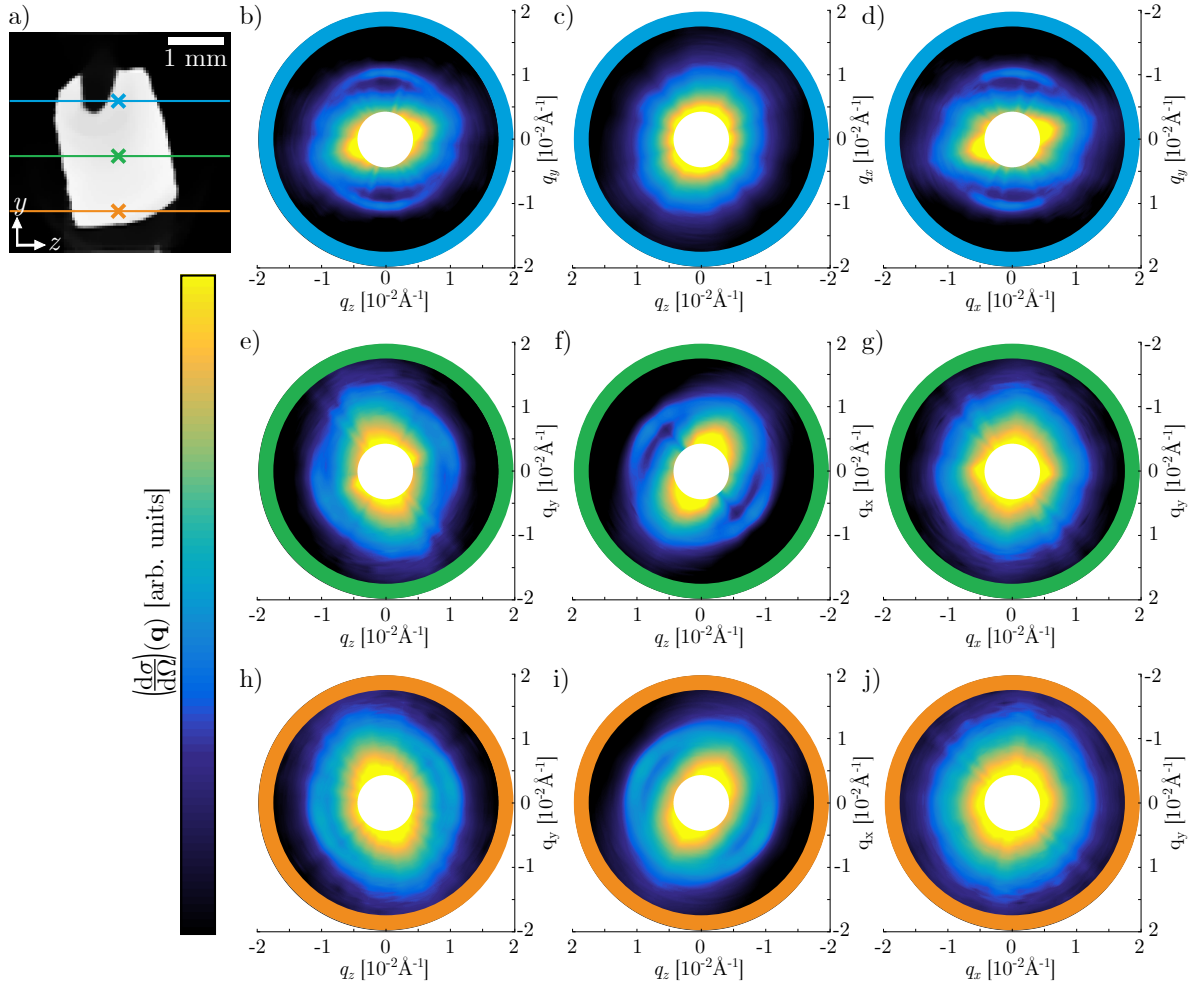


Figure 5.16: **Virtual extraction of SAXS patterns.** Three locations are marked within the sample on the attenuation data (a). For each of these locations, three slices through the local scattering cross section $\left(\frac{d\sigma}{d\Omega}\right)(\mathbf{q})$ perpendicular to the three coordinate axes are shown. The representation is similar to conventional SAXS patterns, which helps understand the data. The orientation of the underlying collagen structures changes drastically from the top to the bottom part of the sample. Animation available at <https://www.youtube.com/watch?v=4B46xiT05w4>.



several slices perpendicular to the three coordinate axes for central points near the top [b)-d)], centre [e)-g)] and bottom [h)-j)] of the sample. The exact locations are marked in a). Given that the scattered intensity is proportional to $\left(\frac{d\sigma}{d\Omega}\right)$, it is clear that this representation looks very similar to SAXS patterns. Qualitative information about the underlying collagen structure can already be seen from this simple representation of the results. The orientation of the characteristic collagen peaks in the top part of the sample [b)-d)] is almost vertical, which hints at a vertical alignment of the underlying collagen fibres. This orientation changes drastically towards the centre [e)-g)] and bottom [h)-j)] of the sample. Furthermore, a noticeable increase of $\left(\frac{d\sigma}{d\Omega}\right)$ towards the bottom of the sample can be observed.

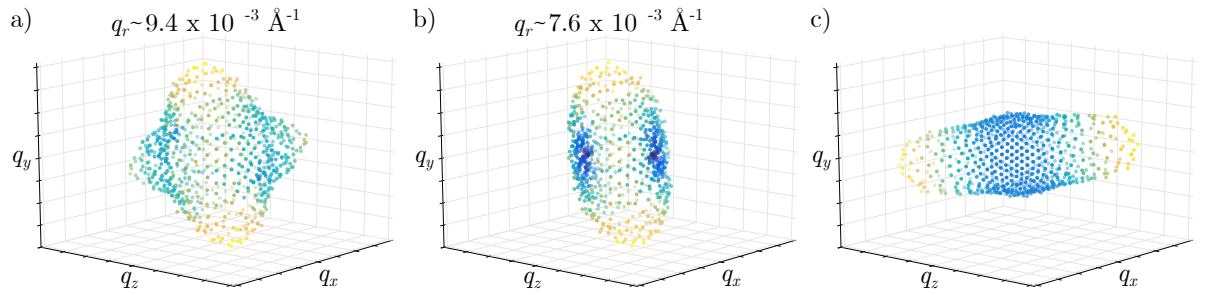


Figure 5.17: **Extraction of collagen fibre orientation.** The measured directions on half the unit sphere scaled and coloured with $\left(\frac{d\sigma}{d\Omega}\right)$ (\mathbf{q}) at two different q_r . a) The characteristic collagen peak is clearly visible in the three dimensional representation for data with $q_r \approx 9.4 \times 10^{-3} \text{ \AA}^{-1}$. b) The radial segment with $q_r \approx 7.6 \times 10^{-3} \text{ \AA}^{-1}$ does not contain this peak. c) An ellipsoid fit to the ratio of the data with (a) and without (b) the additional collagen peak was used to calculate the direction of collagen fibres. The colour scale is not constant between a), b), and c).

5.6.3 Extraction of collagen fibre orientation

One of the main goals of 6-D SAXS-CT was to preserve oriented scattering information throughout the reconstruction. For the investigated tooth sample, obtaining information of the local collagen fibre orientation in three dimensions is an integral part of the analysis. Therefore, a way to extract this information out of $\left(\frac{d\sigma}{d\Omega}\right)$ (\mathbf{q}, \mathbf{r}) is required. For this, we look at yet another way to visualize $\left(\frac{d\sigma}{d\Omega}\right)$ (\mathbf{q}) for one voxel. Here we restrict the visualization to data for a constant q_r , and in return visualize all scattering directions of $\left(\frac{d\sigma}{d\Omega}\right)$ ($\mathbf{q} \mid q_r = \text{const}$) for this q_r . This is done by scaling the measured directions, given as unit vectors (cf. fig 5.5), by the reconstructed values of $\left(\frac{d\sigma}{d\Omega}\right)$ ($\mathbf{q} \mid q_r = \text{const}$). Figure 5.17 a) displays this representation of the data in one voxel for $q_r \approx 9.4 \times 10^{-3} \text{ \AA}^{-1}$. The individual dots are furthermore coloured according to their distance from the origin, i.e.

5 Six-dimensional small-angle X-ray scattering computed tomography

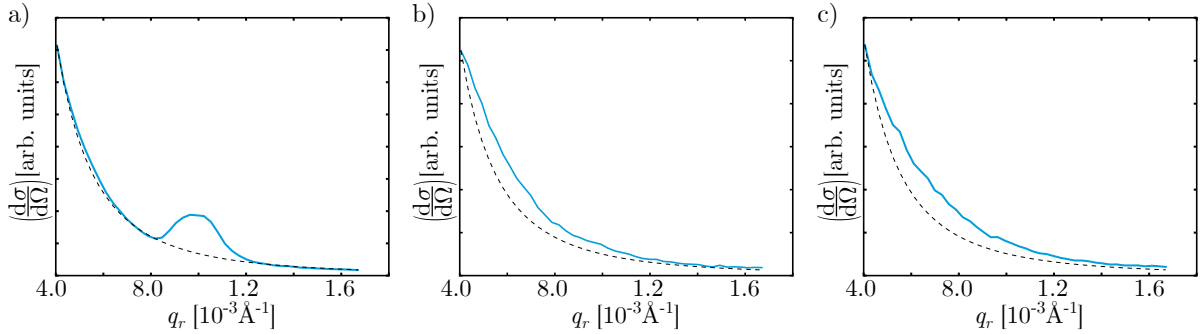


Figure 5.18: **Radial plot of cross sections.** $\left(\frac{d\sigma}{d\Omega}\right)$ is plotted against q_r as solid line for the scattering direction along (a), and two directions perpendicular to the main collagen direction [b) & c)]. A power-law function $c \exp(-2.6q_r)$ normed to the data curve is plotted with dashed lines.

the scaling factor $\left(\frac{d\sigma}{d\Omega}\right)(\mathbf{q})$. Characteristic collagen scattering occurs at this specific q_r . When compared to data at $q_r \approx 7.6 \times 10^{-3} \text{ \AA}^{-1}$, shown in b), the additional scattering arising from the collagen periodicity can clearly be seen.

From previous studies on collagen in teeth, it is known that the shape of $\left(\frac{d\sigma}{d\Omega}\right)(\mathbf{q})$ with increasing q_r can be approximated by a power-law function with an exponent of about -2.6 in the absence of an additional collagen peak [Gaiser, 2012]. Plots of $\left(\frac{d\sigma}{d\Omega}\right)(q_r)$ for scattering orientations in and perpendicular to the direction of collagen fibres are given in figures 5.18 a), b) and c), respectively. In addition, a normed power-law function $c \exp(-2.6q_r)$ is plotted for the three displayed scattering orientations. This function matches almost perfectly to the curve shown in a). Although not as good, a reasonable match can be seen for both plots based on scattering perpendicular to the collagen fibre orientation [b) & c)]. Taking this into consideration, the point-wise ratio between data shown in figures 5.17 a) and 5.17 b) is expected to be approximately constant except for orientations that contain additional collagen scattering. This ratio of $\left(\frac{d\sigma}{d\Omega}\right)$ is shown for every scattering direction in 5.17 c). We see that the resulting three-dimensional distribution has the shape of an elongated ellipsoid with its long axis given by the collagen peak. Using an ellipsoid fit [Qingde Li, 2004] to this ratio allows us to determine the orientation of the collagen fibres in each voxel. Consequently, we use the largest semi-principle axes of the ellipsoid fit as the directions of the collagen fibres. With this method, the collagen orientations are given as a three-dimensional vector-field.

Figure 5.19 shows a visualization of slices through this vector-field, overlaid onto an attenuation reconstruction obtained from the diode data. Given that opposite fibre directions are equivalent, all vectors are represented by bars that are centred at the origin. Furthermore, fibre orientations are only shown in every second voxel for clarity. One needs to also consider that the ellipsoid fit yields results for voxels outside of the sample. The length of each bar therefore was scaled with the attenuation data to suppress visibility of

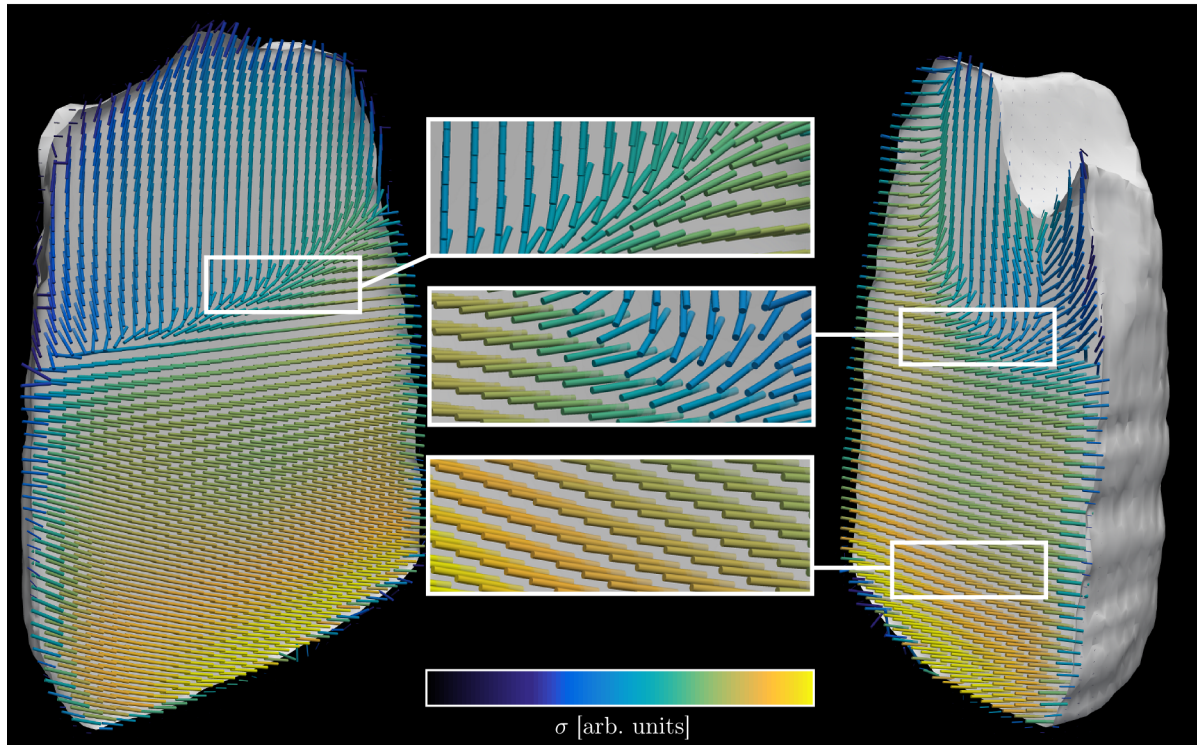


Figure 5.19: **Three dimensional visualization of collagen fibre orientation.**

Two orthogonal slices through the tooth sample are shown. The local orientation of the collagen fibres is visualized by the coloured bars. The colour corresponds to the total cross section σ at $q_r \approx 9.4 \times 10^{-3} \text{ \AA}^{-1}$. Animation available at <https://www.youtube.com/watch?v=J0VaqqV05M>.



vectors outside the sample. Lastly, the colour of each bar is given by the total scattering cross section σ at $q_r \approx 9.4 \times 10^{-3} \text{ \AA}^{-1}$. One characteristic of the HEALpix distribution is that an equal area of the unit sphere is allocated to each point, which allows for a straight forward calculation of σ . Several conclusions about the collagen orientation can be drawn from figure 5.19. First of all, it is evident that the fibre orientation drastically changes within the sample. Fibres close to the root canal are aligned circularly around it. This corresponds to the area of secondary dentine, marked in figure 5.4. Further away from the root canal, in the region of primary dentine, the fibre orientation is almost perfectly parallel to the root canal. Additionally, the increased scattering signal towards the outside of the sample is also clearly visible here.

5.7 Limitations of the method

So far the focus was on the reconstruction and data interpretation. However, several limitations of the method exist, some of which will be discussed here in detail.

5.7.1 Data acquisition

As 6-D SAXS-CT has to be performed at a synchrotron source, acquisition times are crucial. Raster-scanning the sample through the beam is very time consuming, and the available time at the synchrotron ultimately limits the amount of data that can be recorded. The time required to record a single SAXS pattern strongly depends on the energy and flux of the synchrotron beam. The tooth sample was measured with the highest energy available at the cSAXS beamline, 18.6 keV. A substantial amount of the beam was absorbed within the sample at this energy and did not contribute to the SAXS pattern. About 97 percent of the X-rays were absorbed on the longest path through the sample. Given that X-rays attenuation depends strongly on the energy of the photons, even a small increase in energy would significantly reduce attenuation losses. Additionally, synchrotron technology is constantly being improved. Many facilities around the world undergo periodic upgrades with the goal of increasing the available photon flux for experiments. As an example, the upgrade currently being installed at the European Synchrotron Radiation Facility (ESRF) is expected to increase the performance by up to two orders of magnitude. Every bit of more photons available, be it through less attenuation or higher flux, can directly be converted into a faster acquisition time. Latest detector technology is already able to record images with frame rates of several kilohertz and able to handle rapid data acquisition [Dinapoli, 2011]. New limitations may arise in the form of radiation damage to the sample, or the overhead due to mechanical stepping becoming a larger factor. Nonetheless, only a tenfold decrease in acquisition time would push the presented experiment down to a few hours. This would open the door for 6-D SAXS-CT studies with several samples.

5.7.2 Resolution

One needs to differentiate between resolution in real- and reciprocal-space. As mentioned in chapter 4.3, the former is given by the computed tomography part of the measurement, and the latter depends on the scattering geometry during the experiment.

Let us first take a look at real-space resolution. Essentially, the size of the X-ray beam and accordingly the stepping width during raster scanning set a limit for spatial resolution. Given that a P_j is raster-scanned in two directions, the time to record a single P_j scales quadratically with resolution. Furthermore, spatial resolution can be maintained through computed tomography only with a sufficient amount of P_j . One effect of undersampled tomographic data is a loss in spatial resolution after reconstruction. Owing to these

dependencies, an increase in spatial resolution leads to a drastic increase in measurement time. A compromise between the amount of recorded P_j and their resolution needs to be found. Considering all this, the size of a sample ultimately dictates the size of the X-ray beam and therefore spatial resolution. It should be noted that spatial resolution is not the primary goal for this type of experiment. Even though it is difficult to provide an exact number, spatial resolution for the tooth sample is in the order of $10^2 \mu\text{m}$.

Resolution in reciprocal space can be separated into radial and azimuthal resolution. The radial part is easy to determine. It is determined only from the angular divergence of the X-ray beam and the pixel size of the detector. Angular resolution is linked to spatial resolution in some way. The way P_j are selected for each virtual tomography using equation 5.7 introduces a slight mismatch between the reconstructed scattering orientations provided by each individual P_j . A deviation of the scalar product $|\mathbf{q} \cdot \mathbf{t}_j| < 0.08$ corresponds to a mismatch of up to $\approx 5^\circ$. The large amount of virtual tomography axes complicate matters even further and make it hard to provide a quantitative statement about azimuthal reciprocal space resolution.

5.7.3 Reconstruction

A single reconstruction for one combination of q_r and \mathbf{a}_k took ≈ 40 s on a computing server with 2 Intel Xeon E5-2667 processors, 256 GB DDR3 RAM and 4 Nvidia Titan GPUs. With 16896 individual reconstructions in total, performed on two similar computing machines in parallel, the total six-dimensional reconstruction took approximately four days. Given that all reconstructions in principle can be performed in parallel, reconstruction time can be substantially reduced with dedicated reconstruction soft- and hardware. Data processing therefore should not pose a major limitation in the future, even with drastically improved acquisition times.

5.8 Discussion

Six-dimensional SAXS-CT as a method for the complete reconstruction of $\left(\frac{d\sigma}{d\Omega}\right)(\mathbf{q}, \mathbf{r})$ as a combination of three reciprocal- and three real-space dimensions was presented in this chapter. With the complete reciprocal space reconstructed, directional information is preserved in 6-D SAXS-CT. This had been a major limitation in conventional SAXS-CT so far. One of the largest gains from this is the possibility to determine the local orientation of nano-structures.

As the millimetre sized tooth sample consists of oriented collagen fibres with a typical diameter < 300 nm, the full potential of 6-D SAXS-CT was demonstrated here. The possibility to investigate the nano-structure in objects that are several orders of magnitude larger is unique to 6-D SAXS-CT. Let alone the difficulty to non-destructively investigate < 300 nm sized structures in three dimensions, the difference in length-scale between structure and sample size makes an investigation with conventional methods nigh impossible.

5 Six-dimensional small-angle X-ray scattering computed tomography

As 6-D SAXS-CT was developed independently from a specific sample, potential applications are not restricted to collagen-based natural materials, such as bone or teeth. It should be noted that, although the local nano-structure can be characterized for macroscopic objects using 6-D SAXS-CT, structural information is always averaged over the entire volume of a single voxel. Therefore, 6-D SAXS-CT is best suited for investigating changes of the nano-structure over a large field of view, i.e. hierarchically structured materials.

One of the main drawbacks of small-angle X-ray scattering (SAXS) imaging experiments is the necessity of a collimated, monochromatic X-ray beam. Owing to this, SAXS imaging experiments have to be performed at synchrotron facilities. Measurement time at a synchrotron is highly sought after and therefore of limited availability. Additionally, recording scattering information pixel-by-pixel with raster-scanning is very slow compared to conventional imaging.

In the past decade, scattering-based X-ray imaging was brought to the lab in the form of grating-based X-ray dark-field imaging. It is a full-field imaging method that can be performed with laboratory X-ray sources [Pfeiffer, 2008]. Its origins are closely linked to SAXS [Strobl, 2014; Prade, 2015b]. Furthermore, the dark-field can be used to characterize the orientation of structures on length-scales smaller than the actual imaging systems resolution, similar to SAXS imaging [Jensen, 2010a; Jensen, 2010b]. Anisotropic dark-field computed tomography therefore becomes a possibility.

Developed in the early 2000s, grating-based X-ray imaging (GBI) utilizes the refraction and scattering of X-rays to form so-called phase-contrast and dark-field images, respectively [David, 2002; Momose, 2003; Momose, 2003; Weitkamp, 2005]. Although it is one of the more recently developed methods, GBI has already positioned itself as a leading technique for laboratory-based phase-contrast and dark-field imaging. Both additional images are created in full-field mode, next to the conventional attenuation image. One of its key advantages over comparable methods is that GBI is compatible with conventional X-ray tubes and detectors [Pfeiffer, 2006]. Well developed equipment from medical and industrial X-ray imaging can be used, which has allowed GBI to bring X-ray phase-contrast imaging to the lab [Pfeiffer, 2006].

This chapter gives an introduction to grating-based X-ray imaging, with a focus on the dark-field signal.

6.1 Talbot-Lau interferometer

There exist several slightly different realizations of GBI, which all share the basic concept of using a structured illumination to detect slight deflections of the X-ray beam caused by an object. A common laboratory implementation of GBI today is the so-called Talbot-Lau interferometer, which we will base all explanation on here. It stands out from other realizations by its high sensitivity [Birnbacher, 2016]. A Talbot-Lau interferometer is sketched in figure 6.1. Next to a conventional X-ray tube and detector, it consists of three

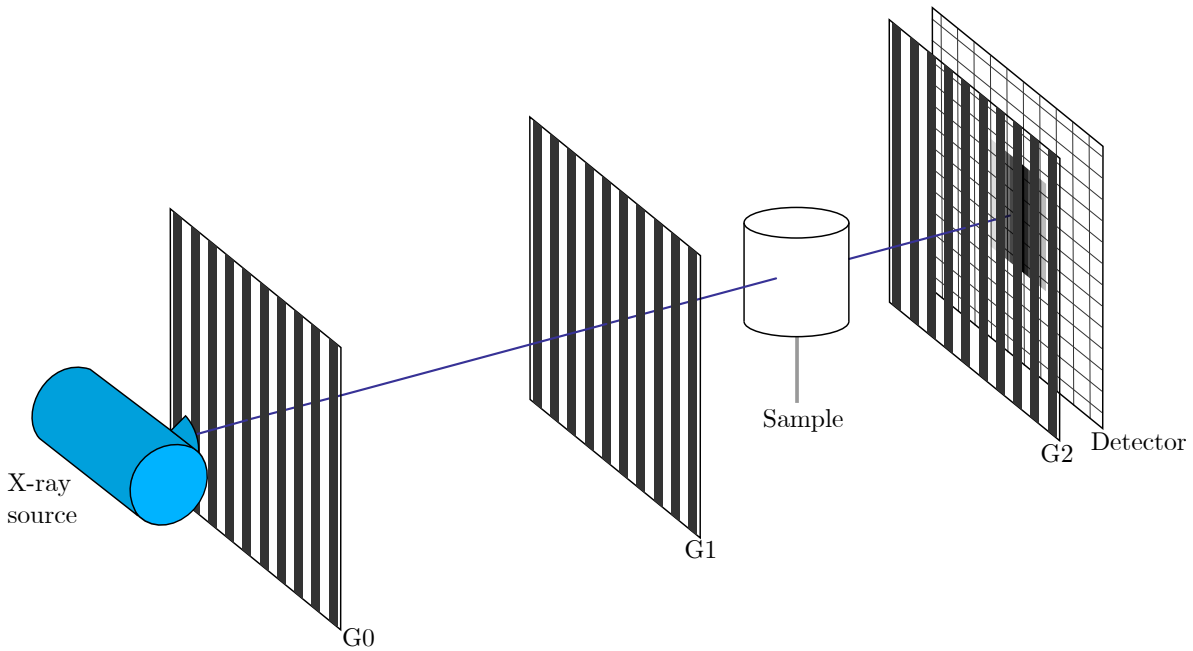


Figure 6.1: **Laboratory Talbot-Lau interferometer.** The interferometer is formed by two gratings G1 and G2, also known as phase- and analyser-grating. A periodic phase-modulation of the X-ray beam created by G1 is analysed by G2 prior detection. A third grating, G0, enables the interferometer to be used with conventional X-ray tubes. Objects can be imaged at any position between G0 and G2.

additional components, called gratings. Although two-dimensional grating designs have been realized before [Zanette, 2010; Modregger, 2014; Kagias, 2016], we will focus on the far more common case of one-dimensional gratings here. The Talbot-Lau interferometer consists of a source-grating G0 close to the X-ray source, an analyser-grating G2 right in front of the detector and a phase-grating G1 in between the other two. X-ray gratings consist of one-dimensional structures, typically arranged with periods of a few μm . An electron microscopy image of a silicon phase-grating G1 is given in figure 6.2. This particular grating consists of $5\ \mu\text{m}$ wide trenches with a repetition period of $10\ \mu\text{m}$, directly etched into a silicon wafer. Even though G1 typically consists of the lowest structures between all three gratings, the high aspect ratio, i.e. depth to width of the structures, required for X-rays is already evident here.

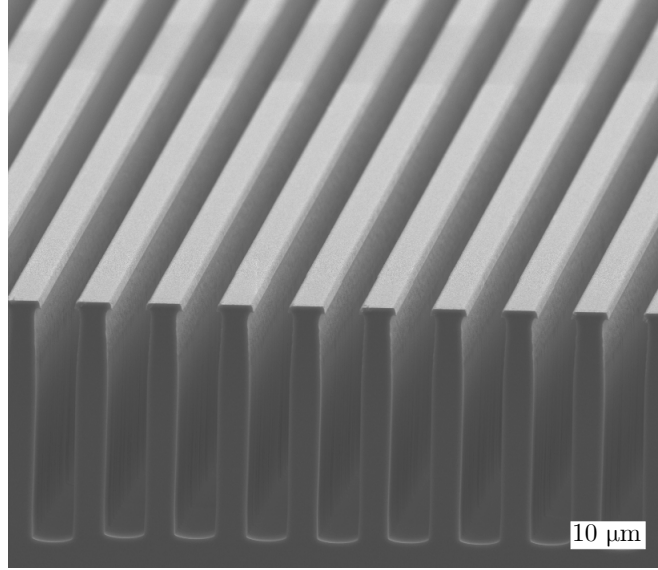


Figure 6.2: **Electron microscopy image of a grating.** A silicon phase-grating with a grating period of $10\ \mu\text{m}$ is shown. Image kindly provided by Markus Schüttler.

6.1.1 G1 & Talbot-effect

Every GBI system revolves around creating a structured illumination. In the case of a Talbot-Lau interferometer in the X-ray regime, this is done with the help of grating G1 and the Talbot-effect. Known from visible light, it states that a periodically modulated wave-front repeats itself after a certain distance d_T [Bech, 2009, p. 17][Jahns, 1979]:

$$d_T = \frac{2p^2}{\lambda}. \quad (6.1)$$

This Talbot-distance only depends on the period p of the modulation and the wavelength λ of the photons. Note that the Talbot-effect does not specify what kind of modulation of the wave-front is required. From this follows that the modulation can be either an amplitude or phase modulation. The latter is advantageous as no intensity of the beam is lost due to the grating. Given that only the intensity of X-rays can be detected, a phase modulation needs to be transformed into an intensity modulation prior detection. Figure 6.3 displays the intensity distribution behind a $\pi/2$ phase-shifting G1. At certain fractions of d_T the phase-modulation is transformed into an intensity modulation of the same period [Lohmann, 1990; Suleski, 1997; Cloetens, 1997]. This is hence also known as the fractional Talbot-effect. One such distance for a $\pi/2$ -shifting phase-grating can be found as $d_T/4$. Let us assume an X-ray energy of 50 kV, which corresponds to a wavelength $\lambda \approx 0.25 \times 10^{-10}$ m. The first fractional Talbot-distance behind a $\pi/2$ -shifting grating with period $p = 10\ \mu\text{m}$ then is found at $d_T/4 = 0.5$ m.

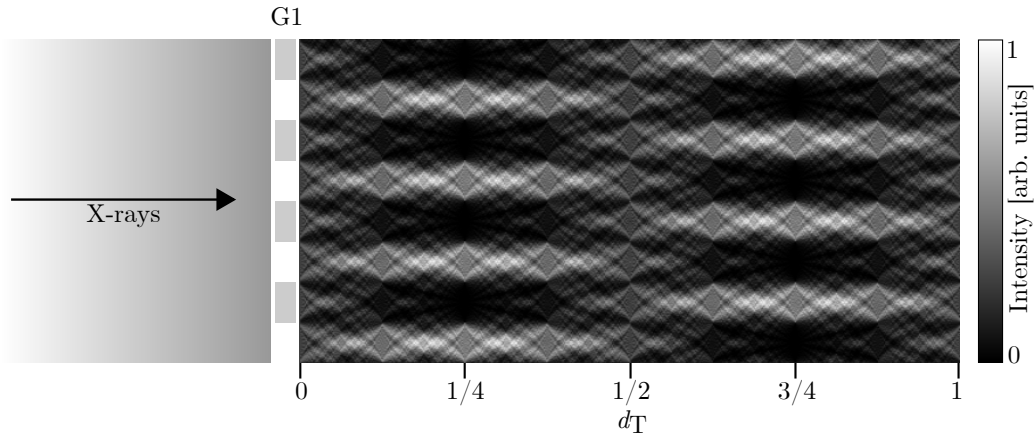


Figure 6.3: **Talbot effect.** A spatially periodic wave-front repeats itself after its Talbot-distance d_T . Such a periodic wave-front is created from a plane wave passing through G1. Additionally, phase-modulations of the wave-front transform into intensity modulations at fractions of the full Talbot-distance. The distances shown here are not true to scale.

6.1.2 G2 & phase-stepping

If the resolution of the X-ray detector is sufficient to resolve the interference pattern created behind G1, changes of this pattern can be directly used to create an image [Kagias, 2016]. Given that it has a period in the order of μm , most X-ray detectors are unable to resolve the intensity pattern created behind G1. This leads us to the second additional component in the interferometer, the analyser-grating G2. It is designed as a mask for the intensity pattern created by G1 in the plane of detection. Its period, p_2 , therefore is matched to that of the intensity pattern. G2 consists of strongly absorbing gold structures, often well over $100\ \mu\text{m}$ high. Combined with the necessary height of the structures, these extreme aspect ratios pose significant challenges to the manufacturing process [Schüttler, 2016].

During a measurement, the relative position of G2 with respect to the interference pattern is changed in discrete steps, as shown in figure 6.4. The offset of G2 is given as the phase difference between G2 and the static intensity pattern, ω . Depending on the relative position of G2 with respect to the interference pattern, a varying amount of intensity is transmitted. The value recorded by the much larger underlying pixel of the detector changes accordingly. Images are recorded at discrete steps to sample a phase-stepping curve for each pixel. The resulting intensity curve is well described by a cosine function [Weitkamp, 2005]:

$$I(\omega) = a_0 + a_1 \cos(\omega + \varphi). \quad (6.2)$$

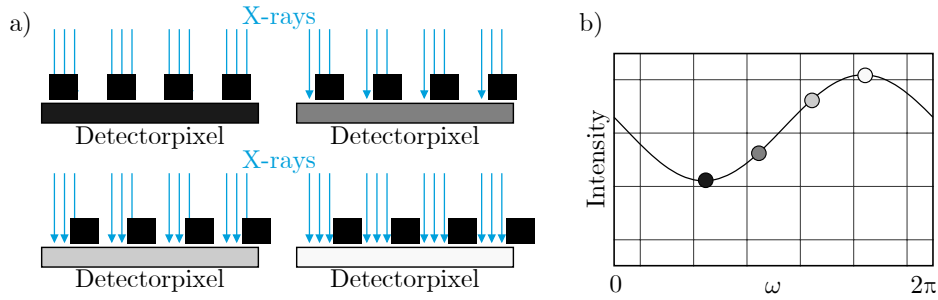


Figure 6.4: **Phase-stepping technique.** The period of the interference pattern created behind G1 in Talbot-interferometry typically is much smaller than the pixel-size of conventional X-ray detectors. Therefore, a second grating, G2, is used to retrieve information about the interference pattern without the need to directly resolve it on the detector. G2 consists of absorbing structures whose period is matched exactly to that of the interference pattern. a) During a phase-stepping scan, G2 is shifted laterally over one period of the interference pattern. b) A stepping curve of the transmitted intensity is sampled at discrete points, from which information about the structure of the unresolved interference pattern in each pixel can be obtained.

The three parameters a_0 , a_1 and φ correspond to the average, amplitude and phase¹ of the intensity oscillation, respectively. This allows to quantify the underlying interference pattern in each pixel without the need to directly resolve it. The use of an analyser-grating G2 allows for phase-contrast imaging without the need for high-resolution detectors [Momose, 2003; Weitkamp, 2005].

6.1.3 G0 & Lau-effect

Interference effects, such as those behind G1, only appear with sufficiently coherent illumination. Due to reasons of flux, imaging experiments with X-ray tubes are typically performed in close proximity to the source. According to equation 2.13, the only way to increase spatial coherence for a given λ therefore is by reducing the size of the source. This can be done by using microfocus X-ray tubes, which, however, also comes at the cost of intensity. Another possible solution was introduced for the Talbot-Lau interferometer in the form of a third grating, G0. Also called source-grating, G0 is an absorption grating that is placed in between the X-ray source and G1. It splits the incident illumination of the original source into an array of fine slit-sources, each of much higher spatial coherence than that of the extended original source [Pfeiffer, 2006]. Interference patterns are created behind G1 from each of these secondary sources, as displayed in figure 6.5. The

¹for reasons of consistency with previous publications, φ denotes the relative phase of the stepping curve in this context, rather than a rotation angle

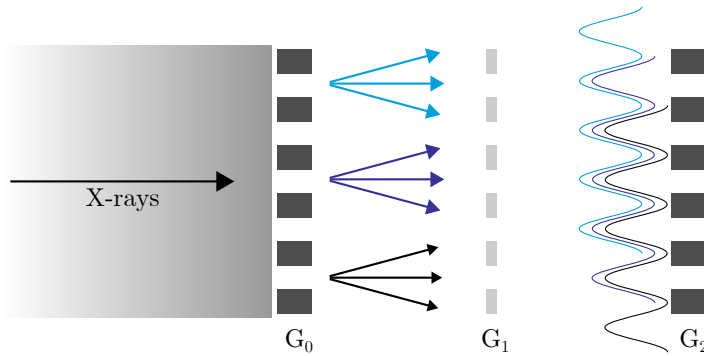


Figure 6.5: **Lau-effect.** The size of the X-ray source spot often times is too big to allow for interference effects to occur behind G_1 . The large source spot is split into an array of fine slit-sources by the so-called source-grating G_0 . Each of these sources provides sufficiently coherent radiation to produce an interference pattern at the position of G_2 . The period of G_0 has to be chosen so that the positions of highest intensity of the individual interference patterns coincide at the position of G_2 .

period and position of G_0 need to be matched to the rest of the interferometer so that the maxima of the interference patterns created by the individual slits coincide at the position of G_2 . This is also known as the Lau-effect, which renders grating interferometry with extended, polychromatic sources possible [Jahns, 1979].

To recap, the Talbot-Lau interferometer consists of three parts: A source-grating G_0 , which provides spatial coherence, a phase-grating G_1 , which creates an interference pattern, and finally an analyser-grating G_2 , which offers the possibility to use large detector-pixels. In case of a sufficiently coherent source, e.g. as is often the case at synchrotron facilities, G_0 can be omitted. Additionally, if direct detection of the intensity pattern is possible, G_2 is not required. Talbot interferometry under special conditions can, therefore, also be performed using only a G_1 [Kagias, 2016].

6.2 Image extraction

The focus shall now be on how to generate attenuation, phase-contrast and dark-field images in GBI. During data acquisition, two series of images are recorded using the phase-stepping technique. One series of the undisturbed imaging system that serves as a reference, and a second series with an object. In every pixel, the resulting intensity oscillations during the reference scan, $I^r(\omega)$, and the sample scan, $I^s(\omega)$, are recorded. They are described according to equation 6.2 as:

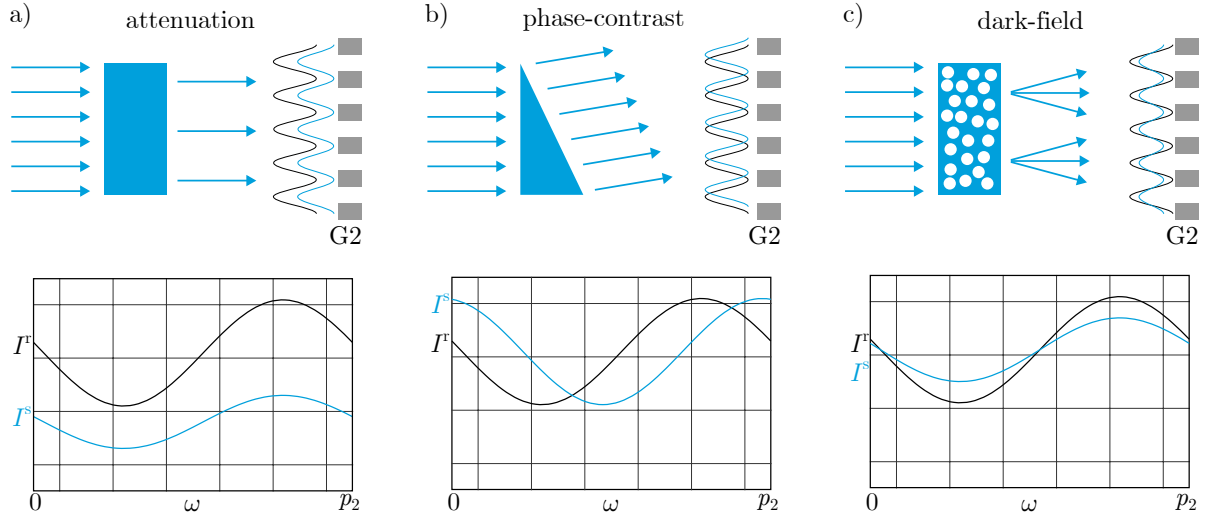


Figure 6.6: **The three imaging signals of a grating interferometer.** Images in grating interferometry are generated from changes of the stepping curve. a) Attenuation signal: A purely attenuating object causes an overall decrease of the intensity, which corresponds to the conventional attenuation image. b) Differential phase contrast: a phase-shifting object, i.e. an object with varying thickness or refractive index decrement δ refracts X-rays. The differential phase-contrast signal is derived from the lateral shift of the interference pattern. c) Dark-field signal: an object with a distinct microstructure gives rise to X-ray scattering, which causes the amplitude of the stepping-curve to be reduced.

$$I^r(\omega) = a_0^r + a_1^r \cos(\omega + \varphi_r), \quad (6.3)$$

$$I^s(\omega) = a_0^s + a_1^s \cos(\omega + \varphi_s). \quad (6.4)$$

An object inside the interferometer causes the stepping curve to change with respect to the reference. Images are created by quantifying these changes in every pixel individually. The parameters a_0 , a_1 and φ are linked to the three different types of images created with a grating interferometer. Figure 6.6 demonstrates the different possible changes of the stepping curve and their relation to specific properties of the object.

6.2.1 Attenuation signal

In a), the case of a purely attenuating object, which causes an overall loss of intensity of the stepping curve is depicted. Parameter a_0 quantifies the offset of the stepping curve, and therefore its average intensity. Consequently, the attenuation image of a grating interferometer, *att*, is defined as the ratio of a_0^s and a_0^r [Bech, 2009, p. 36]:

$$att = \frac{a_0^s}{a_0^r}. \quad (6.5)$$

This image corresponds to the conventional attenuation image. GBI therefore does not compromise the attenuation image in order to obtain additional information about an object. The fact that the attenuation image and the additional contrast modalities are not exclusive to one another holds several advantages in practice, such as e.g. using the attenuation data for image registration.

6.2.2 Differential phase-contrast signal

In section 2.3 we introduced equation 2.19 that links distortions of a wave-front $\Phi(x, y)$ to the refraction angle α . A simple case of an object that creates a distorted wave-front is a wedge, as depicted in figure 6.6 b). Owing to its shape, the integrated phase-shift relative to vacuum varies along the vertical axis. According to equation 2.19 the wave-front is therefore refracted by an angle α . This causes a lateral shift of the interference pattern at the position of detection. The exact position of the interference pattern is described by φ in equations 6.3 and 6.4. The differential phase-contrast image, dpc , is defined as the difference between φ_s and φ_r [Bech, 2009, p. 36]:

$$dpc = \varphi_s - \varphi_r. \quad (6.6)$$

Although it offers the possibility to access phase information about an object, the dpc image is not of relevance to the work of this thesis and will not be considered further.

6.2.3 Dark-field signal

The second additional contrast modality obtained with a grating interferometer is the so-called dark-field image, shown in figure 6.6 c). It corresponds to a reduction of the oscillation amplitude, a_1 . It is important to realize that attenuation caused by an object also affects a_1 to the same extend as a_0 , as is clear from figure 6.6 a). Therefore it is not sufficient to simply derive the dark-field signal from a reduction of a_1 . We define the visibility V of the stepping curve as [Pfeiffer, 2008]:

$$V = \frac{a_1}{a_0}. \quad (6.7)$$

The dark-field signal, df , is then defined as the reduction of visibility caused by an object [Pfeiffer, 2008]:

$$df = \frac{V^s}{V^r} = \frac{a_1^s a_0^r}{a_0^s a_1^r}. \quad (6.8)$$

This definition allows to remove the influence of attenuation on a_1 . The reduction of a_1 caused by other effects can therefore be isolated. This includes a reduction caused by

beam-hardening [Yashiro, 2015], strongly refracting objects [Yang, 2012; Wolf, 2015] or X-ray scattering [Pfeiffer, 2008; Yashiro, 2010]. We will see in the following section that the dark-field signal mainly arises from small-angle scattering at microscopic inhomogeneities inside an object.

6.3 Origin of the dark-field signal

This section shall give a more thorough introduction to the theory that describes the origin of the dark-field signal.

Whereas the attenuation- and differential-phase-contrast signals in GBI are well understood, the dark-field signal has seen various explanations since its introduction in 2008 [Pfeiffer, 2008; Yashiro, 2010; Lynch, 2011; Yashiro, 2011; Yang, 2012; Malecki, 2012; Strobl, 2014; Prade, 2015b; Wolf, 2015; Yashiro, 2015]. In the years ensuing its discovery, several papers were published that present mathematically rigorous analyses [Yashiro, 2010; Lynch, 2011; Yashiro, 2011] and simulations [Malecki, 2012] of the scattering-based dark-field signal. Later it was also shown that a dark-field signal can arise from beam-hardening [Yashiro, 2015], as well as strong refraction at edges [Yang, 2012; Wolf, 2015]. These effects are difficult to quantify and often times small compared to dark-field signals from scattering and will not be considered further. The most complete explanation to date was given by Strobl in 2014 [Strobl, 2014] and verified by Prade et al. the following year [Prade, 2015b]. The explanation of the dark-field signal given here is based upon these two papers.

Although the derivation is lengthy, it provides a deeper understanding of the fundamental physics behind the dark-field contrast in a grating interferometer. Interestingly, the theory originates from the field of spin-echo small-angle neutron scattering (SESANS), where it had been established for many years [Rekveldt, 1996; Bouwman, 1999]. SESANS allows for a detailed, quantitative analysis of scattering processes in real-space [Bouwman, 2002; Krouglov, 2003; Andersson, 2008]. The similarity with SESANS allows us to, in principle, translate much of the work already done for SESANS directly to GBI.

6.3.1 Small-angle scattering in a grating interferometer

Let us for now assume the origin of the dark-field signal as small-angle scattering. We recall from chapter 2.2 that two-dimensional diffraction patterns are measured in a SAXS experiment. This obviously is not the case for dark-field imaging, as the reduction of visibility is a single value. The task therefore is to understand the system response of a grating interferometer to small-angle scattering.

We introduced the scattering angle 2θ in chapter 2, which is of great importance in the description of SAXS experiments. According to figure 6.7, it can also be expressed in terms of geometrical parameters of the grating interferometer as:

6 Grating-based X-ray imaging

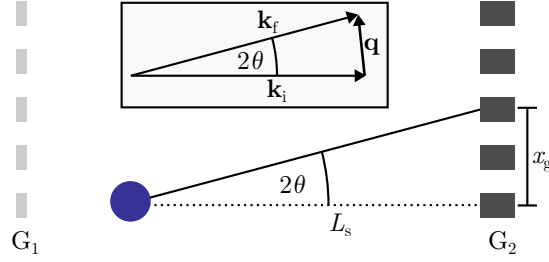


Figure 6.7: **Scattering angle in a grating interferometer.** In the small angle approximation, i.e. $k \gg q$, the scattering angle 2θ is given either in reciprocal space as q/k_i , or in real space as x_g/L_s .

$$\tan 2\theta = \frac{x_g}{L_s}. \quad (6.9)$$

The distance of the sample from G2 and the lateral shift of the scattered radiation at the position of G2 are denoted as L_s and x_g , respectively. The inset of figure 6.7 reminds us of the common definition of 2θ for SAXS in reciprocal space, according to equation 2.8. In the small-angle limit $\tan 2\theta \approx \sin 2\theta \approx 2\theta$ and we can therefore equate equations 6.9 and 2.8:

$$2\theta \approx q \frac{\lambda}{2\pi} \approx \frac{x_g}{L_s}. \quad (6.10)$$

This equation serves as the link between conventional SAXS theory and grating interferometry. We rearrange this result to arrive at a relation between the magnitude of the momentum transfer vector, q , and the offset of the interference pattern of a grating interferometer [Strobl, 2014]:

$$x_g = q \frac{\lambda L_s}{2\pi}. \quad (6.11)$$

Owing to the periodicity of the interference pattern with period p_2 , it is convenient to express the spatial offset of the interference pattern, x_g , as a phase shift $\Delta\omega$ of the modulation function:

$$\Delta\omega = \frac{2\pi x_g}{p_2}. \quad (6.12)$$

Substituting equation 6.11 leads to [Strobl, 2014]:

$$\Delta\omega = q \frac{\lambda L_s}{p_2} = q \xi_{\text{GI}}. \quad (6.13)$$

Here we introduced ξ_{GI} , the so-called autocorrelation length of a grating interferometer [Lynch, 2011; Strobl, 2014] as:

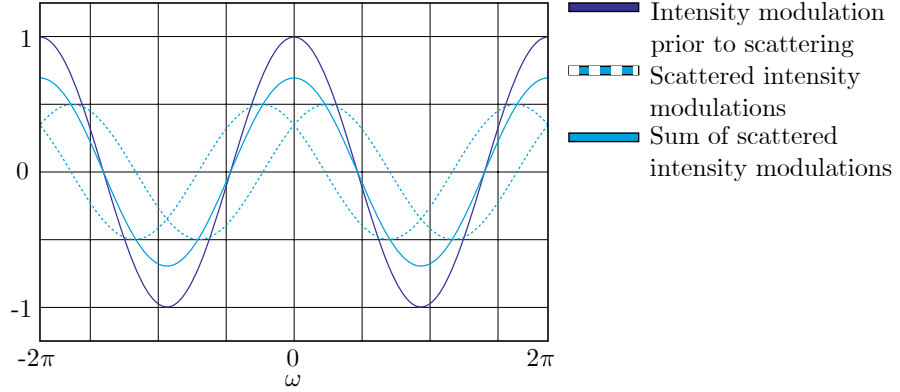


Figure 6.8: **Effect of scattering on the modulation curve of a grating interferometer.** Scattering causes a phase offset of the modulation curve measured in a grating interferometer. As scattering is symmetrical, half of the curve receives a positive phase offset, whereas the other half receives a negative offset. The sum translates into a reduction in amplitude. Figure adapted from Strobl [Strobl, 2014].

$$\xi_{\text{GI}} = \frac{\lambda L_s}{p_2}. \quad (6.14)$$

It is the characteristic length-scale on which structural correlations are probed by a grating interferometer experiment [Prade, 2015b]. Equation 6.13 is central to the following explanation of the dark-field signal, as it provides a link between the grating interferometer and the description of scattering in reciprocal space.

At this point we can now take a closer look on how scattering affects the intensity modulation of a grating interferometer. The general form of a stepping curve is $I(\omega) = a_0 + a_1 \cos(\omega + \varphi)$ (cf. equation 6.3). For simplicity, let us for now assume the stepping curve to be centred around ω , i.e. $\varphi = 0$. Equation 6.13 states that scattering inside a grating interferometer causes a lateral phase shift of the interference pattern. We recall from equation 2.12 that small-angle scattering is symmetric around the origin: $I_{\text{SAXS}}(\mathbf{q}) = I_{\text{SAXS}}(-\mathbf{q})$. For any pair of scattering vectors \mathbf{q} and $-\mathbf{q}$ an equal fraction of the interference pattern is therefore shifted by $\Delta\omega$ and $-\Delta\omega$, respectively. For now, let this fraction be equal to 1, i.e. all photons are scattered either by $-\mathbf{q}$ or \mathbf{q} . The resulting interference pattern of the scattered radiation for this pair of scattering vectors, $J_s(\omega)$, then is the sum of the shifted patterns:

$$J_s(\omega) = \frac{1}{2}I(\omega + \Delta\omega) + \frac{1}{2}I(\omega - \Delta\omega) = \frac{a_0}{2} + \frac{a_1}{2} \cos(\omega + \Delta\omega) + \frac{a_0}{2} + \frac{a_1}{2} \cos(\omega - \Delta\omega). \quad (6.15)$$

We can simplify this equation using the trigonometric identity for angle sums and

6 Grating-based X-ray imaging

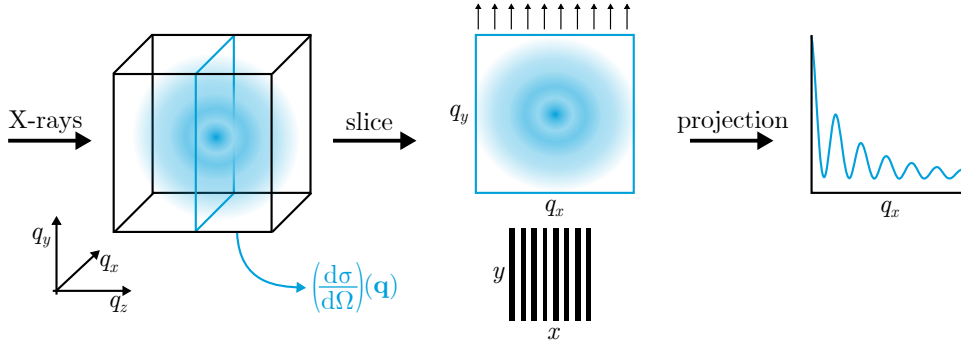


Figure 6.9: **Relevant \mathbf{q} -vectors for scattering in a grating interferometer.** Only scattering from \mathbf{q} -vectors in the slice perpendicular to the incident X-ray beam can be recorded, here shown in z -direction. Scattering in a grating interferometer is further restricted to the component perpendicular to the long axis of the grating bars. In the shown coordinate system this is equivalent to a projection of $I_{\text{SAXS}}(q_z = 0)$ along the q_y -axis.

differences $[\cos(a \pm b) = \cos(a)\cos(b) \pm \sin(a)\sin(b)]$. For $a = -b$ the sine terms cancel out and only an additional $\cos(\Delta\omega)$ term remains:

$$J_s(\omega) = a_0 + a_1 \cos(\omega) \cos(\Delta\omega) = a_0 + a_1 \cos(\omega) \cos(q\xi_{\text{GI}}). \quad (6.16)$$

This result is equal to the original function of the intensity modulation, $I(\omega)$, multiplied by an additional term that reduces the amplitude of the oscillation. Figure 6.8 illustrates the relation between scattering and the reduction of amplitude of the intensity modulation. A scaled version of the original function is reproduced from the sum of both shifted halves. This shows that scattering of X-rays is equivalent to a reduction of modulation amplitude in a grating interferometer. The response of a grating interferometer to scattering depends on the scattering vector \mathbf{q} . This can be understood intuitively by considering scattering under an angle that shifts the interference pattern by exactly one period. One would not be able to distinguish the scattered from an unscattered part of the pattern. Scattering under this angle therefore has no influence on the recorded dark-field signal. The other extreme case is scattering under an angle that causes a shift of exactly half a period. In this case, the interference pattern is completely lost.

6.3.2 Full description of the dark-field signal

We will now move on to a more realistic model of the dark-field signal. Let the propagation direction of the X-beam be along the z -axis as shown in figure 6.9. We know from chapter 2.2 that in the small-angle approximation only scattering vectors $\mathbf{q} = (q_x, q_y, 0)$ are relevant to the scattered intensity I_{SAXS} . From the theory presented in the previous section it is evident that only scattering perpendicular to the long axis of the grating

6.3 Origin of the dark-field signal

bars has an effect on the interference pattern, the x -axis here. This further restricts us to the q_x -component of the remaining scattering vectors. As we are only interested in the q_x -component, we can integrate I_{SAXS} along the q_y -axis. The distribution of the relevant scattered intensity then is a one-dimensional function $I_{\text{S,rel}}(q_x)$:

$$I_{\text{S,rel}}(q_x) = \int I_{\text{SAXS}}(q_x, q_y) dq_y. \quad (6.17)$$

Only a certain fraction of the X-ray beam is scattered. Let us denote this fraction as f . It is equal to the ratio of the integral of $I_{\text{S,rel}}(q_x)$ to the intensity of the incident radiation I_0 :

$$f = \frac{1}{I_0} \int I_{\text{S,rel}}(q_x) dq_x. \quad (6.18)$$

Accordingly, the unscattered part of the beam is equal to $1 - f$. Additionally, unlike in the previous section, not all photons are scattered under the same scattering vector \mathbf{q} . Let $S(q_x)$ be a normalised function that describes the relative distribution of the scattered intensity over all q_x :

$$S(q_x) = I_{\text{S,rel}}(q_x) \left(\int I_{\text{S,rel}}(q_x) dq_x \right)^{-1}. \quad (6.19)$$

In the previous section we derived that scattering in a grating interferometer reduces the amplitude of the modulation function by a factor of $\cos(q\xi_{\text{GI}})$, see equation 6.16. The resulting modulation function $I^s(\omega)$ is a superposition of the scattered and unscattered parts of the X-ray beam. As the response of the grating interferometer to scattering depends on the scattering vector \mathbf{q} , and the scattered intensity is not distributed uniformly in \mathbf{q} -space, we need to modulate the scattered intensity by $S(q_x)$. Altogether we can write $I^s(\omega)$ as:

$$\begin{aligned} I^s(\omega) &= \underbrace{(1-f)(a_0 + a_1 \cos(\omega))}_{\text{unscattered part}} + f \underbrace{\int S(q_x)(a_0 + a_1 \cos(\omega) \cos(\Delta\omega)) dq_x}_{\text{scattered part}} \\ &= (1-f)(a_0 + a_1 \cos(\omega)) + f a_0 \underbrace{\int S(q_x) dq_x}_{=1} + f a_1 \cos(\omega) \int S(q_x) \cos(q_x \xi_{\text{GI}}) dq_x \\ &= a_0 + a_1 \cos(\omega) (1-f + f \int S(q_x) \cos(q_x \xi_{\text{GI}}) dq_x). \end{aligned} \quad (6.20)$$

The resulting visibility after scattering is given as the ratio of the amplitude of the oscillating part to the amplitude of the offset:

6 Grating-based X-ray imaging

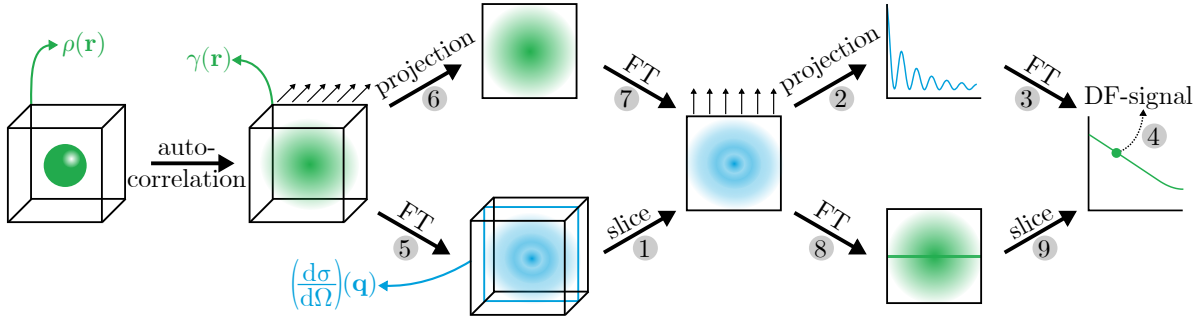


Figure 6.10: **The correlation term of the dark-field signal.** The different steps that lead to the correlation term of the dark-field signal. Blue and green corresponds to the Fourier- and real-space, respectively. See the text for a thorough explanation.

$$V^s(\xi_{\text{GI}}) = \frac{1}{a_0} \left(a_1 - f a_1 + f a_1 \int S(q_x) \cos(q_x \xi_{\text{GI}}) dq_x \right). \quad (6.21)$$

The dark-field signal was defined as the reduction of visibility relative to a reference (cf. equation 6.8). The initial visibility V^r simply is $V^r = a_1/a_0$, which leads us to:

$$df(\xi_{\text{GI}}) = \frac{V^s(\xi_{\text{GI}})}{V^r} = 1 - f + f \int S(q_x) \cos(\xi_{\text{GI}} q_x) dq_x. \quad (6.22)$$

The last term accommodates for the fact that the response of a grating interferometer to small-angle scattering depends on the scattering vector \mathbf{q} . This term also is reminiscent of the cosine term of a Fourier transform. From the definition of the Fourier transform using sine and cosine it follows that for an even function the sine terms vanish and only the cosine terms remain. This is exactly the case here. The cosine response of the grating interferometer therefore performs a Fourier transform of $S(q_x)$ from reciprocal space to a function of the real space variable ξ_{GI} , given that $S(q_x)$ is an even function.

Let us take a closer look on the relation of the last term to known parameters in scattering theory. A schematic overview is given in figure 6.10. We start from the natural description of scattering in three-dimensional reciprocal space, shown in blue. All steps are denoted by small numbers, which we will refer to in the following. The small-angle-approximation restricts the relevant \mathbf{q} -vectors to those of a two-dimensional slice (1). A further restriction to only the component perpendicular to the long axis of the grating bars is given by the grating interferometer. This resembles a projection onto this axis (2). As we have just derived, the last term then is the Fourier transformation to real space (3), shown in green, evaluated at ξ_{GI} (4). The autocorrelation of any function is defined as the convolution of the function with itself. From equations 2.10 and the convolution theorem² we see

² $\mathcal{F}(a \ast b) = \mathcal{F}(a)\mathcal{F}(b)$, where \ast denotes the convolution

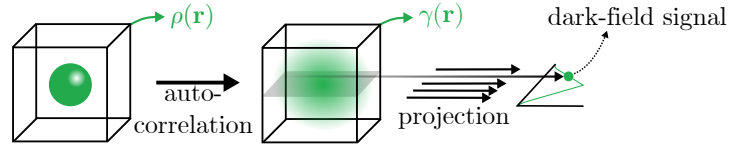


Figure 6.11: **The correlation term as a line integral.** For a given experimental geometry, the correlation term corresponds to a line integral through the three-dimensional autocorrelation function of the sample.

that the scattered intensity distribution in reciprocal space is proportional to the Fourier transform of the three-dimensional autocorrelation function, $\gamma(\mathbf{r})$, of the electron density, $\rho(\mathbf{r})$ (5):

$$I_{\text{SAXS}}(\mathbf{q}) \propto \mathcal{F}(\rho(\mathbf{r}) \ast \rho(\mathbf{r})) = \mathcal{F}\gamma(\mathbf{r}). \quad (6.23)$$

Using the Fourier slice theorem (cf. chapter 3), we can reformulate paths (5,1) and (2,3) as a real-space projection and slice, respectively. The former then turns into a projection of $\gamma(\mathbf{r})$ in real-space (6) and subsequent Fourier transform (7), whereas the latter turns into a slice (9) of a Fourier transform (8). It is clear that the results after steps (6) and (8) are the same, which allows us to fully eliminate the reciprocal space from our considerations. Owing to its connection to the autocorrelation function of the object, the last term in equation 6.22 is also known as correlation function $G(\xi_{\text{GI}}) = \int S(q_x) \cos(\xi_{\text{GI}} q_x) dq_x$. Note that this is not the three-dimensional autocorrelation function itself, but rather a two-dimensional projection of it. The resulting simplified derivation of the correlation term is given in figure 6.11. It is a line integral through $\gamma(\mathbf{r})$:

$$G(\xi_{\text{GI}}) = \int \gamma(x = \xi_{\text{GI}}, 0, z) dz. \quad (6.24)$$

In this convention, the X-ray beam and the long axis of the grating bars are along the z-axis and y-axis, respectively. The value of ξ_{GI} that is probed by the grating interferometer is defined by the geometry of a measurement (cf. equation 6.14). Different values for ξ_{GI} are most easily measured by changing the sample position inside the grating interferometer along the z-axis [Prade, 2015b].

If we account for strongly scattering, thick samples and multiple scattering, equation 6.22 turns into an exponential [Rekveltdt, 2003; Strobl, 2014]:

$$df(\xi_{\text{GI}}) = \exp \left(\int f(G(\xi_{\text{GI}}) - 1) dz \right), \quad (6.25)$$

where f and G are now position dependent functions within the sample [Strobl, 2014]. This result serves as the best description for the formation of small-angle scattering-based dark-field signal. To understand the implications of this result better, consider that df assumes values between 0 and 1, with $df = 1$ corresponding to no scattering. The latter

6 Grating-based X-ray imaging

is exactly the case for $G(\xi_{\text{GI}}) = 1$, i.e. perfect autocorrelation, or homogeneous material. The other extreme, $G(\xi_{\text{GI}}) = 0$ corresponds to a heterogeneous microscopic structure on the length ξ_{GI} , which leads to X-ray scattering.

Tomographic reconstruction of the three-dimensional, anisotropic dark-field signal is one of the more recent developments in grating-based X-ray imaging (GBI). Especially in the last few years it has seen plenty of attention. Various different methods and implementations have been developed [Malecki, 2014b; Bayer, 2014; Revol, 2013; Lauridsen, 2014; Vogel, 2015]. To date, a complete reconstruction has only been achieved by the use of complex reconstruction techniques [Malecki, 2014b; Malecki, 2013; Bayer, 2014; Vogel, 2015]. Moreover, the data acquisition as presented by Vogel et al. [Vogel, 2015] and Malecki et al. [Malecki, 2014b; Malecki, 2013] requires highly specialized, bulky, and expensive hardware. This need for dedicated, highly complex algorithms and specialized acquisition hardware severely hinders the possible application of directional dark-field tomography. This chapter presents a straight-forward implementation of directional dark-field tomography that provides results similar to the X-ray Tensor Tomography (XTT) method presented in [Malecki, 2014b; Malecki, 2013]. A brief introduction to XTT can be found in the next chapter.

7.1 Rotational invariance of the dark-field signal

The method presented in this chapter originates from the considerations on rotational invariance of the small-angle X-ray scattering (SAXS) signal discussed in chapter 4. Hence, rotational invariance of the dark-field signal is discussed in the following.

A central result for SAXS computed tomography (CT) was that scattering vectors \mathbf{q} parallel to a rotation axis \mathbf{a} can be reconstructed using standard techniques. Given the origins of the dark-field signal in SAXS, a similar concept for dark-field tomography suggests itself. Let \mathbf{s}' be the sensitivity direction of the grating interferometer, i.e. the direction perpendicular to the long axis of the grating structures in the plane of the gratings. The dark-field signal depends on \mathbf{s}' , as well as the direction of the incident radiation that we denoted as \mathbf{t}' . The dependency on \mathbf{s}' for a simple CT measurement is sketched in figure 7.1. Two different grating orientations are compared, which we will call vertical (a) and horizontal (c) in the following. We consider a rotation of the sample around a vertical rotation axis \mathbf{a} . Furthermore, we use a fixed autocorrelation length ξ_{GI} during the measurement, as is generally the case. Depending on the orientation of the sample with respect to \mathbf{s}' and \mathbf{t}' during a single dark-field image, different line integrals through the autocorrelation function $\gamma(\mathbf{r})$ then contribute to the dark-field signal. The relevant two-dimensional slices of $\gamma(\mathbf{r})$ for vertical and horizontal grating alignment are

7 Non-iterative directional dark-field tomography

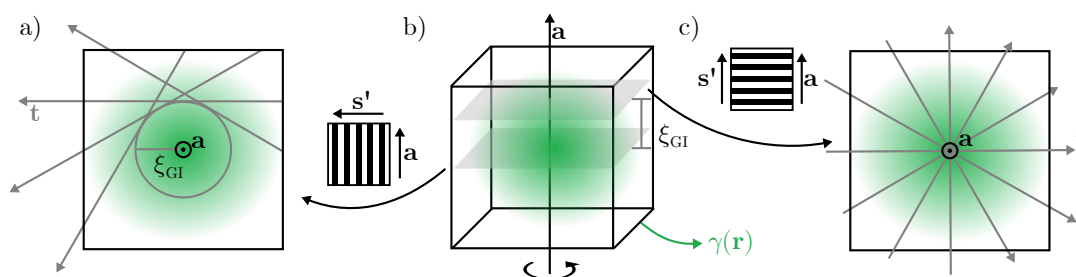


Figure 7.1: **The correlation integral for computed tomography.** a) Slice of the autocorrelation function for vertical grating alignment, $\mathbf{s}' \perp \mathbf{a}$. The measured dark-field signal for different rotations around the vertical axis, \mathbf{a} , corresponds to tangents of a circle with radius ξ_{GI} . b) The position of the slices shown in a) and c). c) Horizontal grating alignment, $\mathbf{s}' \parallel \mathbf{a}$. All line integrals include a single point of the correlation function along the vertical axis at distance ξ_{GI} from the origin.

sketched in b).

For vertical grating alignment the line integrals through $\gamma(\mathbf{r})$, recorded under different rotations of the sample, resemble the tangents of a circle with radius ξ_{GI} in the horizontal plane perpendicular to \mathbf{a} through the origin. The case of horizontal gratings is shown in c). Following equation 6.17, a grating interferometer with horizontal grating alignment is sensitive to the vertical component of the scattering vectors. Matters are slightly more complicated than in the SAXS case, owing to the system response of the grating interferometer. Even though \mathbf{s} is constant for all views of the sample, the line integrals through $\gamma(\mathbf{r})$ differ. A common feature is that they all include the same point in direction of \mathbf{s} at the correlation length ξ_{GI} . One trait of $\gamma(\mathbf{r})$ is that it often can be considered a monotonically decaying function. Therefore, the point contained in all line integrals contributes the most to the dark-field signal. This can also be understood in reciprocal space. Even though the main scattering contribution is from \mathbf{q} -vectors parallel to \mathbf{a} , a certain amount of the signal originates from off-axis scattering. The main contribution is the same for all views of the sample, but the off-axis contributions differ for the different views of the sample. Given that the scattered intensity typically is inversely proportional to $|\mathbf{q}|$, the off-axis contributions often are weaker than the primary sensitivity direction. With this in mind, even though no true rotational invariance is achievable in GBI, a horizontal grating alignment is the best approximation possible. Furthermore, a horizontal grating alignment allows to assign a unique sensitivity direction to a single CT measurement, in contrast to any other grating alignment.

So far we have used \mathbf{r} to describe $\gamma(\mathbf{r})$. However, as we plan to do tomography, \mathbf{r} is already reserved as the variable denoting spatial positions in the sample. To avoid confusion, we will use ϵ as the variable that describes the orientation of scattering information. Hence, ϵ can be seen as the dark-field equivalent to \mathbf{q} used in the SAXS-part of this thesis. It

7.1 Rotational invariance of the dark-field signal

should be noted that ϵ as we use it for the remainder of this thesis can only be defined on the two-sphere \mathbb{S}^2 , rather than in \mathbb{R}^3 . From this follows that the reconstructed quantity, $df_{\text{rec}}(\epsilon, \mathbf{r})$, is only five-dimensional, rather than six-dimensional as with SAXS.

7.1.1 Experimental parameters

In the following, several different CT scans are presented. All of them were generated the same way, described here. All relevant parameters of the used grating interferometer can be found under "conventional setup" in table 8.1 on page 106. Besides the grating interferometer, the imaging setup consisted of an *X-ray WorX 160-SE* microfocus X-ray tube and a *Varian PaxScan 2520DX* detector with CsI scintillator. The X-ray tube was operated at 60 kV acceleration voltage and 125 W anode power, and the detector was rebinned to an effective pixel size of 254 μm . Dark-field and attenuation images were created from seven equidistant grating steps with 0.5 second exposure time per step. The sample was measured between G1 and G2 with a geometric magnification $M = 1.14$. For an average photon energy of 45 keV, this corresponds to a correlation length of $\xi_{\text{GI}} \approx 0.55 \mu\text{m}$. Each individual CT measurement consisted of 205 projection images, equally spaced over 360° sample rotation. Filtered back-projection (FBP) was used to reconstruct the data.

7.1.2 Comparison of horizontal and vertical grating alignment

Let us experimentally showcase improved rotational invariance of the dark-field signal with horizontal gratings. An ideal sample needs to consist of anisotropic structures, such as fibres, preferably with varying orientation within the sample. For this reason we assembled a test sample consisting of several wooden toothpicks glued together to form the letters "TUM". Photographs of the sample inside a plastic sphere that was necessary for positioning can be seen in figure 7.4. Besides its anisotropic wooden structure, the sample is characterized by its easily recognizable geometrical shapes, which allows for a clear visualization of the results.

Two independent dark-field CT scans were recorded. The only difference between the scans was the alignment of the gratings, and therefore the orientation of \mathbf{s}' . Both datasets were reconstructed using filtered back-projection to obtain a volume with vertical, V_v , and a volume with horizontal grating alignment, V_h . Given that only the orientation of the gratings was adjusted between the measurements, V_v and V_h are perfectly registered. The results are compared in figure 7.2. Slices through V_h and V_v are shown in the top row [a)-b)] and the bottom row [d)-e)], respectively. Information from the exact same positions within the sample are compared in each column, i.e. [a), d)] and [b), e)]. Given that V_v and V_h are based on completely different scattering information, slices at the same position of the sample do not necessarily look alike. It is clear that V_v is corrupted by strong streak artefacts, whereas V_h is nearly free from them. The improved reconstruction result in V_h is a direct consequence of the improved rotational invariance of

7 Non-iterative directional dark-field tomography

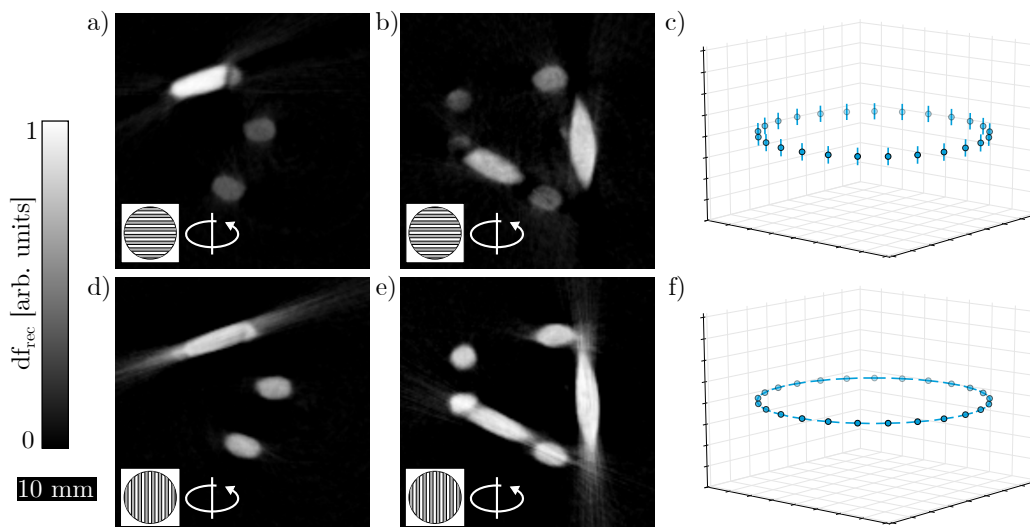


Figure 7.2: **Comparison of horizontal and vertical grating alignment.** Reconstruction results using filtered back-projection are compared for horizontal and vertical gratings in a), b) and d), e), respectively. Slices at the same position of the reconstructed volumes are shown in [a), d)] and [b), e)]. Evidently, the reconstruction results for vertical gratings [b), d)] are severely affected by streak artefacts. With horizontal alignment of the gratings [a), b)], these artefacts are substantially reduced. c), f) For all projections of the CT measurements, the beam direction \mathbf{t} is shown as dots, and the corresponding sensitivity vector direction \mathbf{s} is shown as lines. Horizontal and vertical gratings are compared in c) and f), respectively. Animation available at <https://www.youtube.com/watch?v=Zfbozv4hWbk>.



the dark-field signal when $\mathbf{s}' \parallel \mathbf{a}$. The relative beam direction \mathbf{t} in the sample coordinate system during a CT measurement is sketched in c) and f) for horizontal and vertical grating orientations, respectively. In addition to this, the relative orientation of \mathbf{s} is indicated for each measurement point by a small line. This is necessary, given that the grating interferometer records scattering information primarily along \mathbf{s}' , rather than in all directions as is the case for SAXS.

Although no true rotational invariance can be achieved, as derived in the previous section, the study presented here verifies that a substantially improved reconstruction result is achieved using a grating alignment for which $\mathbf{s}' \parallel \mathbf{a}$.

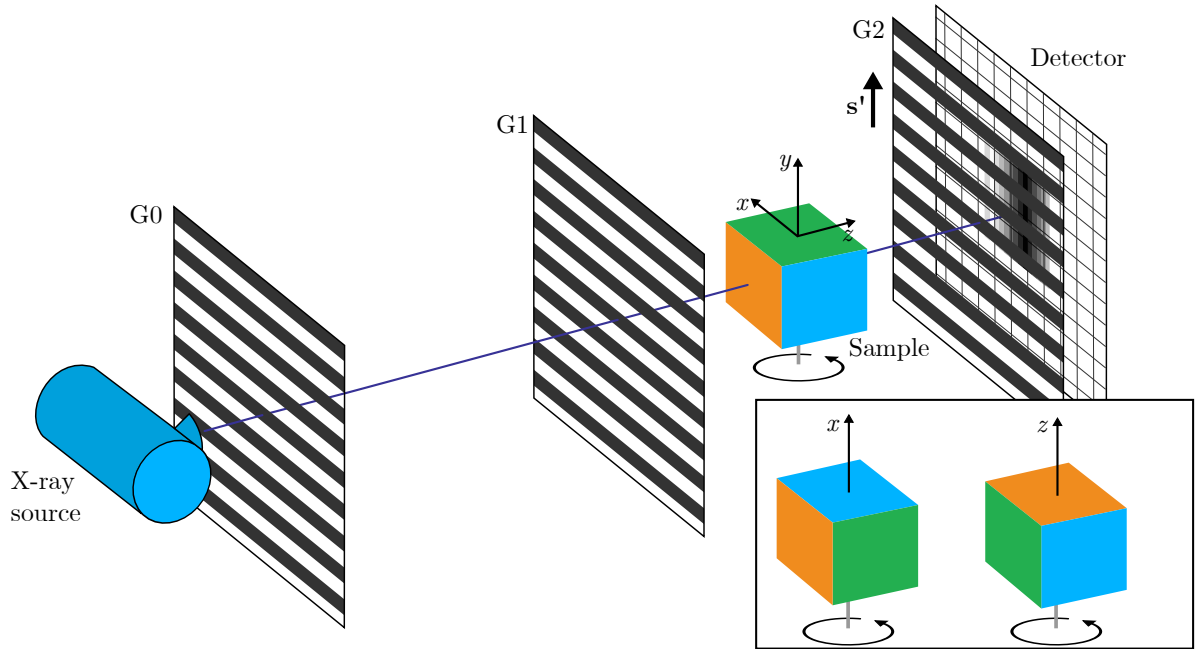


Figure 7.3: **Experimental realization of non-iterative directional dark-field tomography.** Multiple CT measurements of the same sample are recorded. Only the position of the sample on top of the rotation axis is adjusted, as shown in the inset. The sensitivity direction s' remains parallel to the axis of rotation for each CT measurement. A single scattering orientation is probed with each CT scan this way.

7.2 Piecewise reconstruction of the anisotropic dark-field signal

A grating alignment with $s' \parallel \mathbf{a}$ allows to reconstruct the anisotropic dark-field signal $df_{\text{rec}}(\epsilon, \mathbf{r})$ in direction of \mathbf{a} reasonably well. Based on this result, we can use the same argumentation as discussed for SAXS-CT in section 5.4.2 here: As a specific scattering orientation is probed with a single CT measurement, multiple CT measurements can be combined to fully reconstruct a three-dimensional function that describes the scattering behaviour in each voxel. For SAXS, this was ruled out as much of the data would be thrown away in the process. Contrary to SAXS, a single dark-field image can be measured relatively fast, albeit only for one single \mathbf{s} at a time. Due to this, a piecewise reconstruction of $df_{\text{rec}}(\epsilon, \mathbf{r})$ is possible in GBI. The limiting factor is the amount of scattering directions that can be measured. The basic idea of such an experiment is shown in figure 7.3. A GBI setup with s' parallel to the rotation axis has to be used to achieve quasi-rotational invariance of the dark-field signal for a single CT measurement. The entire experiment consists of several individual CT measurements. By changing the position



Figure 7.4: **Sample mounting for non-iterative directional dark-field tomography.** The sample is positioned inside a hollow sphere, which allows for an arbitrary positioning of the sample on top of the rotation stage.

of the sample on top of the rotation axis, as indicated in the inset, different orientations of \mathbf{s}' in terms of sample coordinates, and therefore scattering orientations ϵ_k are probed. A full reconstruction of $df_{\text{rec}}(\epsilon, \mathbf{r})$ is possible by combining the results for a larger number of ϵ_k .

7.2.1 Experimental realization

The main purpose of this project was to provide a straight-forward, easy to realize implementation of directional dark-field tomography. With this in mind, expensive additional hardware and complex reconstruction algorithms were avoided in the experimental realization. Filtered back-projection is the reconstruction algorithm of choice, as it is widely used and easy to implement. However, FBP comes with stringent sampling requirements. In particular, the algorithm relies on evenly sampled data without missing wedges. This requirement rules out static sample mounting, as for some ϵ_k , projections would have to be taken along the axis of the sample mount. To solve this issue, an auxiliary sample mounting in form of a hollow sphere was introduced. A photograph of the wooden "TUM" mounted inside the sphere is given in figure 7.4. Such a sample positioning holds several advantages. First of all, and most importantly, the sample can be positioned arbitrarily on top of the rotation stage, given the perfect symmetry of a sphere. Secondly, as the sphere is made of a thin shell of plastic it does not significantly attenuate X-rays. Lastly, owing to its smooth surface and homogeneous material the sphere does not contribute to the dark-field signal. Even though the last two effects do not play a role after CT, a strong background stemming from the sphere would reduce the dynamic range of a measurement noticeably.

In total, seven complete CT data sets of the wooden "TUM" sample were measured with

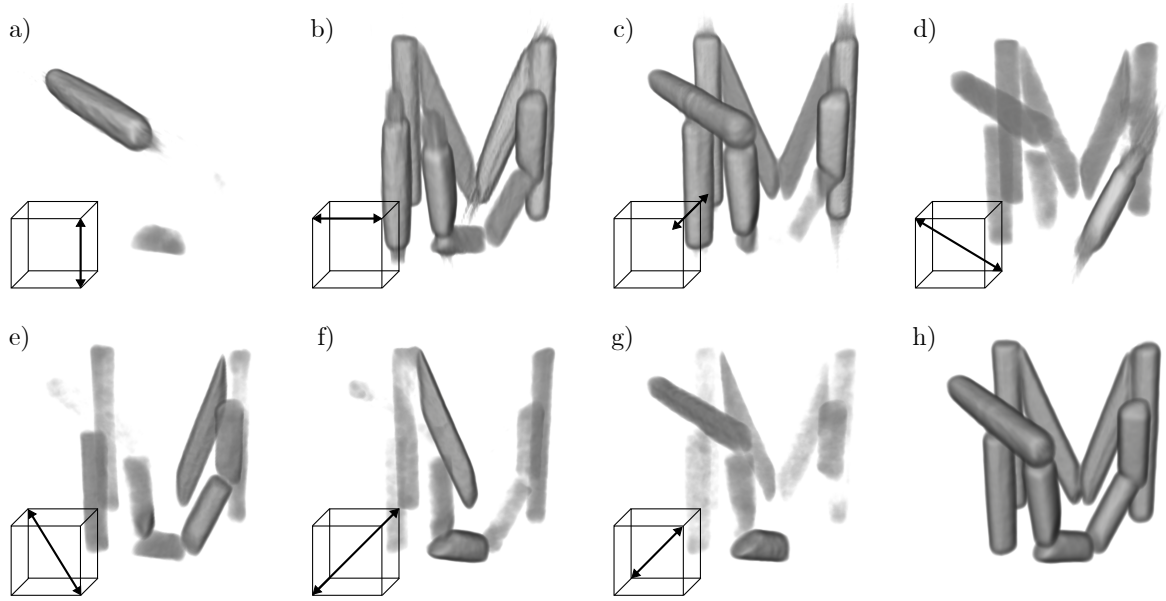


Figure 7.5: **3-D renderings of dark-field reconstructions with different sensitivity directions.** a)-g) Volume renderings of the seven reconstructed and registered dark-field volumes. The sensitivity direction during each measurement is indicated for each volume by the arrows. h) Volume rendering of the average scattering data derived from all seven registered dark-field reconstructions.

seven unique sensitivity orientations ϵ_k , $k = 1, \dots, 7$. As the sample rotation between each measurement was performed by hand, an exact positioning of the sample was not possible. We will see that a perfect distribution of ϵ_k is not required for a good reconstruction of the fibre orientations. The ϵ_k were chosen to approximately sample three orthogonal directions, i.e. the coordinate system axes, as well as the four corresponding space diagonals. Since all seven measurements probe a different scattering orientation, the resulting datasets are completely independent from one another. The attenuation and dark-field volumes, $V_{k,\text{att}}$ and $V_{k,\text{df}}$, were reconstructed using FBP for all seven datasets. Given that attenuation and dark-field data are acquired simultaneously in the GBI setup, $V_{k,\text{att}}$ and $V_{k,\text{df}}$ are intrinsically registered for a single measurement. However, the different measurements are rotated and translated with respect to each other. Let us define $V_{1,\text{att}}$ as the reference dataset. The remaining six datasets were registered to $V_{1,\text{att}}$ using the isotropic attenuation signal $V_{k,\text{att}}$; $k = 2, \dots, 7$. There exist several powerful commercially available softwares to perform volume registration in three dimensions. Here, this step was performed using *Avizo Fire 8.0.1 - FEI, Hillsboro, Oregon, USA*.

As the registration parameters obtained from attenuation data can directly be used for the dark-field data, all $V_{k,\text{df}}$ were aligned with the help of $V_{k,\text{att}}$. Volume renderings of the seven reconstructed and registered $V_{k,\text{df}}$ are shown in figure 7.5 a)-g). Within each panel, the approximate orientation of the probed sensitivity orientation ϵ_k is indicated by an

7 Non-iterative directional dark-field tomography

arrow. The complementarity of the information recorded in the individual volumes can be seen clearly. Depending on the relative orientation of the wooden fibres and reconstructed scattering component, different parts of the sample are visible in different volumes. Given that ϵ_k are distributed approximately evenly in space, a non-biased average volume, V_{df} , was calculated as:

$$V_{\text{df}} = \frac{1}{7} \sum_{k=1}^7 V_{k,\text{df}}. \quad (7.1)$$

This volume is shown in figure 7.5 h). A clean rendering of the dark-field signal of the sample is possible this way, even though it consists of highly anisotropically scattering fibres.

For a quantitative determination of the fibre orientation in each voxel of the sample it is vital to know the orientation of ϵ_k probed with every $V_{k,\text{df}}$ after registration. From the registration procedure a rotation matrix \mathbf{R}_k is obtained for each $V_{k,\text{df}}$. All of them describe the rotation of a single volume $V_{k,\text{df}}$ with respect to the reference volume. Let $\epsilon_1 = (0, 1, 0)^\top$ for the reference $V_{1,\text{df}}$. The probed orientation for each of the other six volumes can then be calculated as:

$$\epsilon_k = \mathbf{R}_k(0, 1, 0)^\top. \quad (7.2)$$

7.3 Comparison with X-ray tensor tomography

At this point, the data is very similar to the results obtained with XTT. The major difference between the two approaches is that in XTT several scattering components are reconstructed simultaneously into separate volumes while in the presented approach we independently measure and reconstruct the individual scattering components [Malecki, 2014b; Vogel, 2015]. A comparison of the results for both methods therefore suggests itself. On this account an XTT reconstruction as described in Vogel et al. [Vogel, 2015] was performed using all projection recorded for the FBP-based approach presented here. Given that arbitrary scattering directions can be reconstructed in XTT, exactly those ϵ_k probed with the FBP-based approach were chosen for reconstruction with XTT. The resulting reconstructed data structure is equivalent for both methods. Seven XTT-based volumes, $V_{k,\text{XTT}}$, and seven FBP-based volumes $V_{k,\text{FBP}} (\equiv V_{k,\text{df}})$ were reconstructed, albeit with completely different methods. Scattering information for all ϵ_k is contained within both data sets. A qualitative comparison is given in figure 7.6. Slices through $V_{k,\text{XTT}}$ and $V_{k,\text{FBP}}$ are shown side-by-side for all seven ϵ_k . Furthermore, the mean value of the XTT- and FBP-based data-sets is presented. Given the differences in the reconstruction methods, the absolute values of $V_{k,\text{XTT}}$ and $V_{k,\text{FBP}}$ differ significantly. For this reason, the XTT- and FBP-based datasets were normed to unity. This scaling is necessary in order to allow for a direct comparison. Similar to figure 7.5, different parts of the sample are

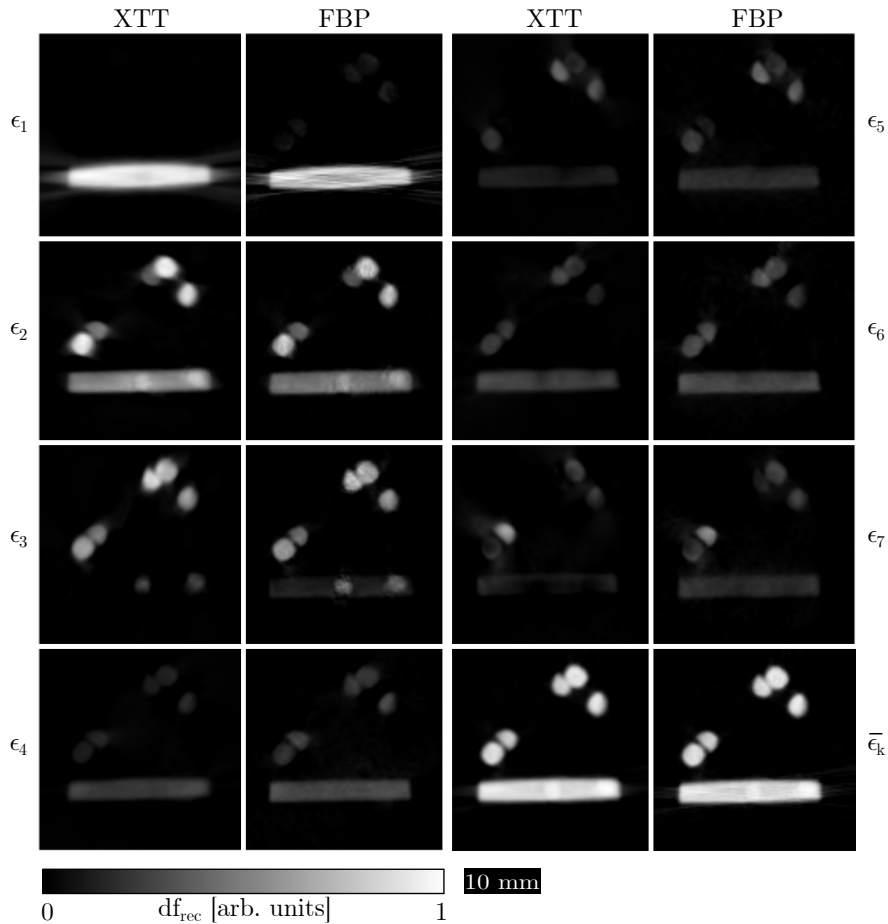


Figure 7.6: **Comparison of FBP-based anisotropic dark-field CT with XTT.**

Slice through the reconstructed volumes corresponding to the seven scattering orientations ϵ_k ; $k = 1, \dots, 7$ are shown for wooden "TUM" sample. Additionally, the the mean value of both data-sets in the same slice is given. The XTT and FBP data are normed to the maximal value found in $V_{k,XTT}$ and $V_{k,FBP}$, respectively. The two slices representing the mean value are normed to unity, in order to enhance contrast. Animation available at <https://www.youtube.com/watch?v=b27SVTG8ge8>.



easily distinguished in figure 7.6, owing to the strong dependence of the scattering signal on ϵ_k . Furthermore, differences between the XTT- and FBP-based reconstructions are minuscule and exist mostly in the form of the XTT results being noticeably smoother. This is not surprising, given that the result for each ϵ_k is influenced by all projections in XTT, whereas only a subset is used for each ϵ_k in the FBP-based approach. Besides this, the results are very similar. Subtle features of the reconstruction results can be discerned

in both reconstruction methods. This is remarkable, considering the substantial difference between the reconstruction methods. These results confirm that the presented method is able to reproduce the results obtained by XTT by means of a simplistic approach.

7.4 Extraction of fibre orientation

As the results are equivalent to those obtained with XTT, any post-processing and visualization can be adapted from XTT. Therefore an ellipsoid fit routine as described in Jud et al. [Jud, 2016] was used here to extract the orientation of the wooden fibres in each voxel. In each voxel an ellipsoid is fit to the unit vectors ϵ_k , scaled with the reconstructed values of the corresponding V_k . From the three resulting semi principal axes the smallest one is defined to be the structure orientation. This can be argued with the idea that a fibre scatters primarily in direction perpendicular to its long axis. Therefore, by taking the smallest semi-principle axis of the ellipsoid fit of the scattering distribution, the fibre orientation can be retrieved. A visualization of the fibre orientation within the wooden "TUM" sample is presented in figure 7.7. Every small bar indicates the local orientation of the underlying fibre structure of the wood. To further enhance the different orientations found within the sample, each bar is also coloured according to its orientation with respect to the vertical axis. At this point the special design of the sample shows its advantages. The easily understandable geometrical shape allows to recognize the individual toothpicks. From this, it is clear to see that the microscopic fibre orientation very closely matches that of the macroscopic wooden parts. The orientation of all reconstructed ϵ_k is shown in the inset, coloured the same way as the sample. Although selected by hand, the orientations of ϵ_k are well distributed. This is necessary to ensure a proper sampling of the scattering function in each voxel, given that only a limited number of ϵ_k can be probed during a measurement.

7.5 Discussion

A piecewise reconstruction of the anisotropic dark-field signal was presented here. Albeit conceptually very different, this new approach is able to reproduce the results obtained from the much more complex XTT reconstruction. Following this, data processing of the resulting multi-dimensional dataset is analogous to XTT, which allows for existing methods to be applied. All results were generated using only existing reconstruction and image processing software and minimal additional hardware in the form of a spherical sample holder. The complex reconstruction algorithms of XTT were substituted with several FBP reconstructions and subsequent registration. One major entry hurdle of conventional XTT is the complexity of the method, which demands the development of a dedicated hard- and software environment. Due to its greatly decreased demands in both of these areas, the presented alternative approach can be easily implemented into an exist-

ing grating interferometer. Registration software, as well as implementations of the FBP algorithm are commercially available. Based on this, the presented method holds great potential to advance orientation dependent dark-field tomography. The lightweight implementation makes this field more accessible for future applications. Preliminary studies can be conducted without the need to dedicate a lot of time and effort to implementation, as is the case for XTT.

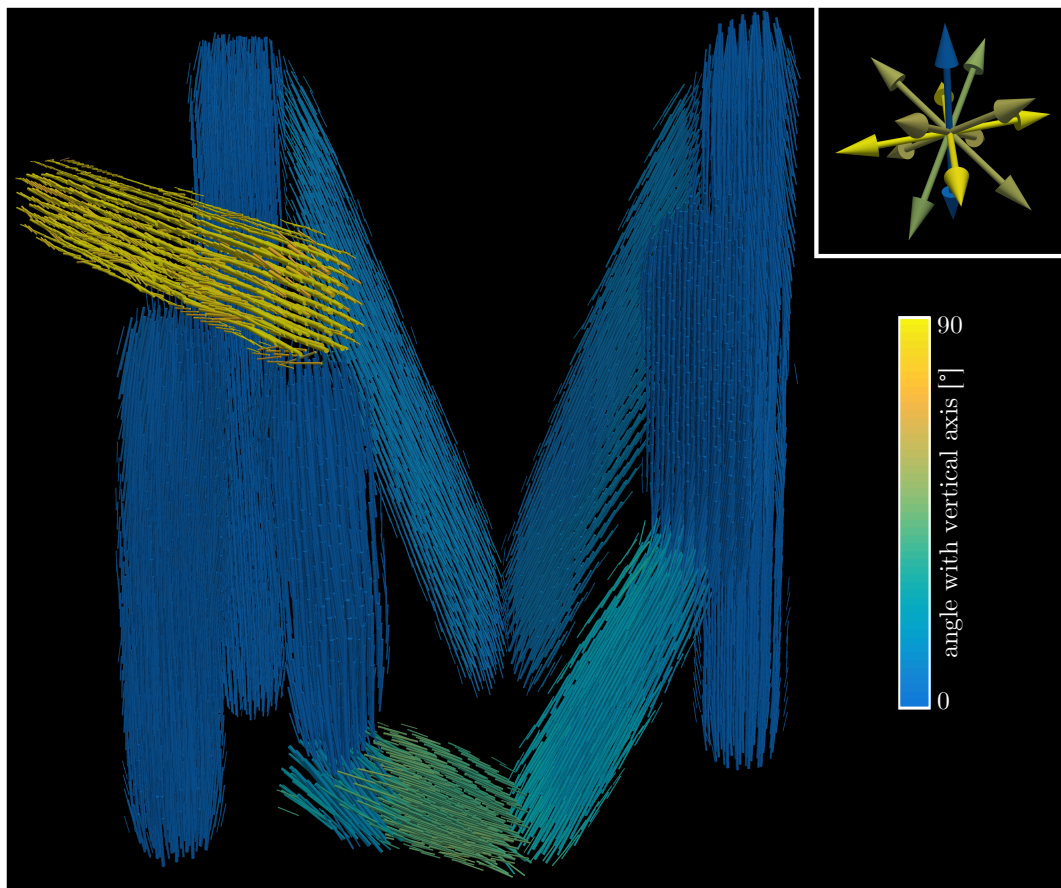


Figure 7.7: **Visualization of the fibre orientation inside the "TUM" sample.**

Just like for XTT, fibre orientation is extracted by fitting an ellipsoid to the scattering distribution in each voxel. The smallest semi-principal axis of the ellipsoids is defined as structure orientation and shown here. Structure orientation in each voxel is given by the small bars, whose colour corresponds to their direction with the vertical axis. The seven reconstructed scattering orientations ϵ_k are shown in the inset. Animation available at <https://www.youtube.com/watch?v=QH6NykA6Ns8>.



Iterative directional dark-field tomography

8

X-ray Tensor Tomography (XTT) is used as a comparison to the newly developed method presented in the previous chapter. Even though the results of XTT can be reproduced by simple means, the more complicated method offers greater flexibility in the reconstruction and potentially more sophisticated data acquisition. Next to six-dimensional small-angle X-ray scattering (SAXS) computed tomography (CT) and the non-iterative approach to XTT presented in chapters 5 and 7, respectively, further development of the early version of XTT proposed by Malecki et al. [Malecki, 2014b; Malecki, 2013] is the last major topic of this thesis. Therefore, a review of the initial state of XTT is given in this chapter. This is followed by a discussion of the advancements to the method developed over the course of this work. Lastly, select applications are presented.

Many of the ideas presented in this chapter were worked out in close collaboration with the Chair for Computer Aided Medical Procedures (CAMP / I-16) at the TUM Department of Informatics. The publications originating from this collaboration are mentioned at the appropriate positions in the following text.

8.1 Review of X-ray tensor tomography

As introduced in chapter 7, XTT was the first realization of a complete directional dark-field tomography. Essentially, in each voxel of an object, the effective scattering strength $df_{\text{rec}}(\epsilon, \mathbf{r})$ is reconstructed for a number of discrete scattering orientations ϵ_k , $k = 1, \dots, N$. In the XTT algorithm the contribution of a single voxel to the measured dark-field signal is considered to be the sum over all ϵ_k , individually weighted by w_{jk} . This weighting factor w_{jk} depends on ϵ_k , and on the orientation of the sample for a dark-field projection P_j . Let \mathbf{t}_j and \mathbf{s}_j be the directions of the incident radiation and sensitivity of the grating interferometer in sample coordinates, respectively. The weighting factors w_{jk} are calculated as:

$$w_{jk} = (|\mathbf{t}_j \times \hat{\epsilon}_k|)^2 (\mathbf{s}_j \cdot \hat{\epsilon}_k)^2. \quad (8.1)$$

Owing to a negligible cone-beam angle in all experiments presented here, w_{jk} is approximately constant for all pixels of a dark-field projection P_j [Malecki, 2014b]. This approximation does not necessarily hold for larger cone angles and a pixel-dependent $w_{jk}(x, y)$ would have to be used to account for this accordingly.

Evidently, it is not sufficient to reconstruct a single scalar volume in \mathbb{R}^3 in XTT. For N scattering directions ϵ_k , an equivalent amount of N volumes are required, each containing

8 Iterative directional dark-field tomography

the reconstructed information for a single ϵ_k . Vogel et al. have shown that the matrix-based description of CT, cf. equation 3.3, can be extended for XTT [Vogel, 2015]. Let $\mathbf{W}_k = \text{diag}(w_{1k}, w_{2k}, \dots)$ be diagonal scaling matrices that contain all w_{jk} . The complete system matrix then is composed of N parts $\mathbf{W}_k\mathbf{M}$ as:

$$(\mathbf{W}_1\mathbf{M}, \mathbf{W}_2\mathbf{M}, \dots)\mathbf{x} = \mathbf{p}. \quad (8.2)$$

Note that \mathbf{x} here does not only contain all voxels of a single volume, but rather N times that amount, i.e. all voxels of N reconstructed volumes. Although equation 8.2 is the correct mathematical description of the problem, it is very abstract and the more intuitive, equally valid view is that of several volumes that are reconstructed simultaneously. With the problem described as a system of linear equations, well-established methods to solve equation 8.2 for \mathbf{x} , e.g. simultaneous algebraic reconstruction technique (SART) or conjugate gradient (CG), can be applied [Vogel, 2015].

Structural orientation is retrieved in each voxel by fitting an ellipsoid to the point-cloud obtained from scaling all ϵ_k with the corresponding reconstructed values [Malecki, 2014b; Vogel, 2015; Jud, 2016].

8.1.1 Limitations of the XTT reconstruction

Several limitations exist for the XTT model as introduced by Malecki et al [Malecki, 2014b; Malecki, 2013]. First and foremost, the reconstruction results depend on the reconstructed scattering directions ϵ_k . While this is not a problem for an isotropic distributions of all ϵ_k on the unit sphere, an anisotropic distribution leads to a significant bias of the results, as demonstrated in figure 8.1. Three different distributions of ϵ_k are compared. A nearly isotropic distribution is shown in a), and distributions with a strong bias in y -, and x -direction are shown in b) and c), respectively. XTT reconstructions of the same data set were performed using the ϵ_k visualized in a)-c). The corresponding results for the same voxel are illustrated d) - f), where d) shows the results for distribution a), and so on. For visualizing the reconstructed three-dimensional dark-field signal, the distance of all ϵ_k from the origin is scaled and coloured with their reconstructed value within this single voxel. Furthermore, the outline of each distribution is marked as a guide to the eye. As the reconstructed sample consisted of carbon-fibres approximately along the y -axis in this voxel, the highest dark-field signal is expected to lie in the x - z -plane. The results for an isotropic ϵ_k distribution shown in d) clearly conform to this. Biased ϵ_k distributions distort the results, shown in e) and f). Given that a bias in y (e) coincides with the fibre-axis, only a minor change to the results can be observed. However, a bias in x (f) drastically alters the results up to a point where a correct statement of the underlying fibre-structures cannot be made. One could argue that XTT works as long as an isotropic distribution of ϵ_k is ensured. While this is true, the results of an XTT reconstruction should ideally be unaffected by which arbitrary ϵ_k are reconstructed.

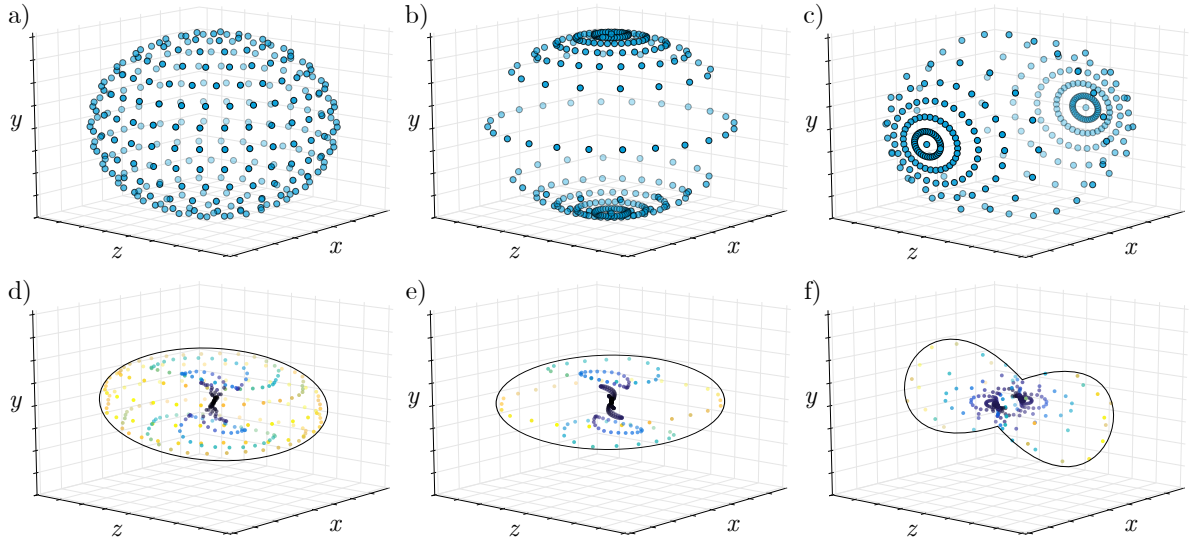


Figure 8.1: **Influence of reconstructed orientations in XTT.** Reconstruction using the same raw data are compared for three different ϵ_k distributions: a) Isotropic distribution, b) bias in y , and c) bias in x . d)-f) Resulting dark-field distributions in the same voxel using the ϵ_k shown in the panel above. The distance of each ϵ_k is scaled and coloured with the reconstructed values. The strong influence of the reconstructed ϵ_k is evident.

Secondly, given that the scattering signal is split into N different orientations, the reconstructed magnitude for each ϵ_k depends directly on N . Owing to this, quantitative comparisons between varying N are rendered impossible if this is not accounted for. However, a simple normalization with N resolves this issue, for an isotropic distribution of ϵ_k .

As stated in the previous section, structural orientation in XTT is retrieved from an ellipsoid fit [Malecki, 2014b; Vogel, 2015; Jud, 2016]. While the scattering distribution obtained from fibres can often be approximated reasonably well by an ellipsoid, several cases exist where this is not true. One prime example can be thought of as a voxel that contains fibres in multiple different directions [Wieczorek, 2016]. However, multiple fibre orientations within a single voxel can not be retrieved using a simple ellipsoid fit and a more sophisticated analysis is, therefore, required.

8.2 Anisotropic X-ray dark-field tomography

In order to overcome the main limitations of XTT, namely the insufficiency of an ellipsoid fit and the bias introduced by picking ϵ_k , anisotropic X-Ray dark-field tomography (AXDT) was developed as an advancement of XTT. A detailed description of AXDT was published as:

8 Iterative directional dark-field tomography

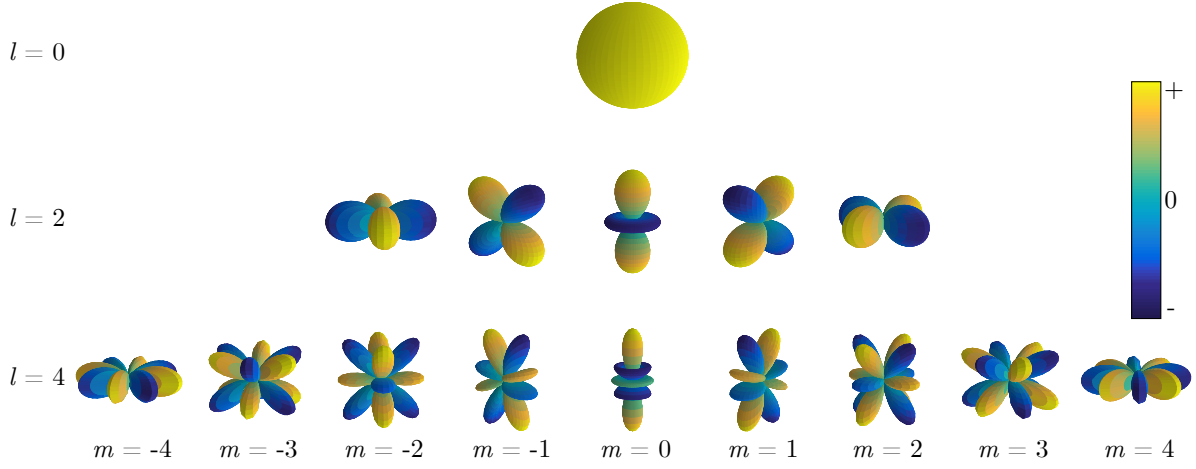


Figure 8.2: **Real valued spherical harmonics of even degree.** The magnitude of each Y_{lm} in different spatial directions is represented by the distance of the surface from the origin. Colour coding is used to indicate the correct sign of Y_{lm} .

Wieczorek, M., **Schaff, F.**, Pfeiffer, F. & Lasser, T. Anisotropic X-Ray Dark-Field Tomography: A Continuous Model and its Discretization. *Physical Review Letters* **117**, 158101 (2016)

Here, the basic principle of AXDT and the differences to XTT are outlined. For a thorough mathematical description of AXDT the reader is referred to the publication mentioned above [Wieczorek, 2016] and the PhD thesis by Matthias Wieczorek currently under preparation.

Rather than reconstructing the scattering magnitude for several distinct scattering orientations ϵ_k , AXDT uses a special set of k functions to model the scattering distribution within a single voxel. Given that they provide a complete basis for functions on \mathbb{S}^2 , we chose to use real-valued spherical harmonics Y_{lm} as the basis of modelling in AXDT [Wieczorek, 2016]. Spherical harmonics are defined by their degree $l = 0, 1, \dots$, and their order $-l \leq m \leq l$. As the dark-field signal is point symmetric about the origin, it is sufficient to restrict ourselves to Y_{lm} with even order $l = 0, 2, 4, \dots$. A visual representation of the first three even orders of real-valued Y_{lm} is given in figure 8.2.

During the AXDT reconstruction, coefficients c_{lm} for all Y_{lm} are reconstructed in each voxel. The scattering distribution $df_{\text{rec}}(\epsilon)$ in each voxel is then given as:

$$df_{\text{rec}}(\epsilon) = \sum_{l=0,2,\dots} \sum_{m=-l}^l c_{lm} Y_{lm}. \quad (8.3)$$

The series of Y_{lm} has to be truncated at a certain l , as it is impossible to reconstruct an infinite order $l = \infty$ of Y_{lm} . Owing to the system response of a grating interferometer, weighting functions similar to XTT have to be implemented in the reconstruction. For now we stick with the same cosine- and sine-based weighting as in XTT (cf. equation 8.1). It can be shown that in this instance $c_{lm} = 0$ for $l > 4$, and hence it is sufficient to restrict the reconstruction to $k = 15$ functions Y_{lm} , i.e. $l = 0, 2, 4$.

The advantages of AXDT over XTT are clear. Given that $df_{\text{rec}}(\epsilon, \mathbf{r})$ is directly modelled by the set of Y_{lm} using AXDT, all scattering orientations are intrinsically represented equally in the reconstruction. Therefore, the bias problem present in XTT is circumvented. Spherical harmonics are used in many different fields and their mathematical relations have been extensively investigated. Hence, a lot of different methods for data processing on spherical harmonics exist. One example is the Funk-Radon transform that allows for efficient extraction of structure orientations from $df_{\text{rec}}(\epsilon, \mathbf{r})$ [Funk, 1913]. Unlike the ellipsoid fit used in XTT, this more than one primary structure orientation can possibly be extracted this way.

All reconstruction results presented in this chapter were calculated using AXDT with Y_{lm} up to order $l = 4$.

8.3 Data acquisition with an Eulerian cradle

In chapter 5.1 we argued that an additional axis of rotation is required for 6-D SAXS-CT. Owing to the one-dimensional sensitivity of a grating interferometer, yet another rotation is required in order to access all possible scattering orientations in dark-field imaging. The experimental setup for XTT hence consists of a standard grating interferometer and a sample mounting that allows for three independent rotations of the sample.

The experimental implementation of these rotations was done with an *Eulerian Cradle 511* manufactured by *Huber Diffraktionstechnik GmbH & Co. KG*. A photograph of this device is shown in Figure 8.3. It allows to perform three rotations on a sample positioned in the centre of the cradle that correspond to the three Euler angles ψ, θ , and φ , introduced in chapter 3.3.2. The design of the device limits the ψ rotation to $|\psi| \lesssim 45^\circ$. For $|\psi| \gtrsim 45^\circ$ the outer ring of the Eulerian Cradle moves in between the sample and the X-ray source, effectively blocking all radiation. Besides this limitation, any combination of the three Euler angles can be used to position the sample.

Little attention has been paid so far to what exact combinations of the Euler angles to measure during an XTT measurement [Malecki, 2014b; Vogel, 2015; Jud, 2016]. Nested schemes of ψ, θ , and φ were used to cover as many different sample positions as possible. The sampling quality of these schemes, however, is by no means optimal. In fact, after taking a closer look at the data acquisition step, it turned out some of the nested schemes used so far even contained completely redundant sample orientations.

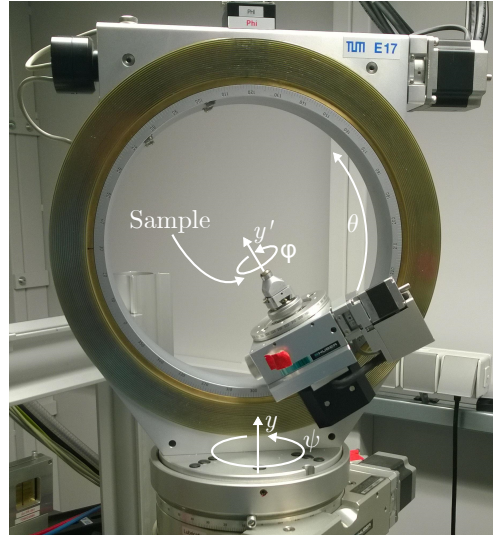


Figure 8.3: **Eulerian Cradle.** A sample placed at the centre of this device can be rotated around three independent axes, indicated by the respective Euler angles φ , θ , and ψ . A practical limitation of $|\psi| \lesssim 45^\circ$ exists, as the outer ring moves into the X-ray beam for $|\psi| \gtrsim 45^\circ$.

8.3.1 Scattering-orientation specific acquisition schemes

For this reason a more advanced data acquisition scheme was developed, aimed at optimizing the information content of a measurement. The goal in any directional dark-field tomography is to reconstruct the local scattering information in all directions ϵ on a hemisphere, given that $\epsilon \equiv -\epsilon$. Conversely, an ideal measurement should contain data that allows to reconstruct a sufficient number of ϵ_k , distributed evenly on a hemisphere.

The results presented in chapter 7 are based on the fact that sufficient data for a single scattering orientation ϵ is measured by rotating the sample around an axis $\mathbf{a} \parallel \epsilon$ and positioning the gratings so that the sensitivity vector \mathbf{s}_j is parallel to \mathbf{a} for all projections. Therefore we can state that a set of projections P_j around ϵ_k with $\mathbf{s}_j \parallel \epsilon_k$ provides sufficient information to reconstruct ϵ_k .

From these considerations follows that an optimized sampling scheme should consist of sets of projections that probe several ϵ_k , distributed evenly on a hemisphere. Such a sampling scheme is illustrated in figure 8.4 a) for three ϵ_k , whose orientation is shown in b) (mirrored at the origin for clarity). Owing to the one-dimensional sensitivity of the grating interferometer, the direction of \mathbf{s}_j is shown for each P_j in a) as little bars on each point that represents the beam direction \mathbf{t}_j . Evidently, a tomographic set of P_j with $\mathbf{s}_j \parallel \epsilon_k$ exists for every ϵ_k . This way, sufficient data is provided to reconstruct these three ϵ_k .

At this point we once more arrive at the question of finding an isotropic distribution of points the (hemi-)sphere. Even though spherical pixelation methods known from astro-

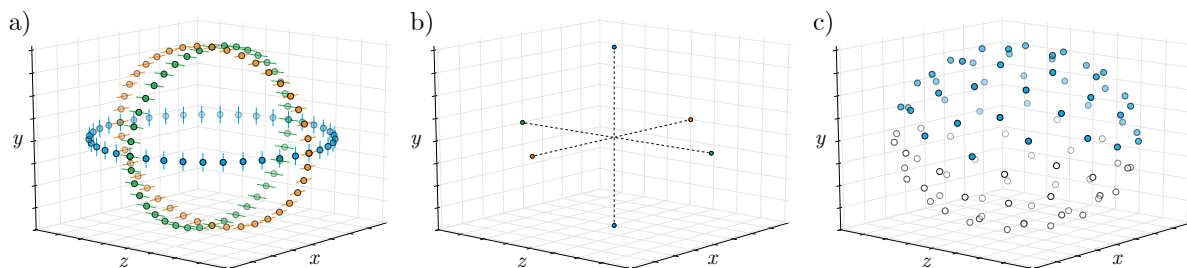


Figure 8.4: **Improved Acquisition Schemes.** a) Tomographic sampling of three ϵ_k . The measured projections are shown as dots. For each projection, the little bar indicates the orientation of the gratings \mathbf{s} . Every ϵ_k is sampled by projections with $\mathbf{s} \parallel \epsilon_k$. b) The orientation of the three corresponding ϵ_k , mirrored at the origin. c) Spherical-design with 94 points on the sphere. As the upper hemisphere exactly mirrors the lower hemisphere, only the upper 47 points are used as ϵ_k , shown with filled dots. Data from <http://neilsloane.com/sphdesigns/dim3/>.

physics were used to generate points for the SAXS case, shown in chapter 5, a different method has proven to be more fitting for the current problem.

Spherical designs, or t-designs, are a number of different distributions of points with very beneficial mathematical properties when dealing with functions defined on \mathbb{S}^2 , e.g. spherical harmonics. A large number of such designs has been proposed by Hardin and Sloane [Hardin, 1996]. A library of spherical designs in three dimensions can be found at <http://neilsloane.com/sphdesigns/dim3/>. All of them are defined on the full sphere. Given that $\epsilon \equiv -\epsilon$, we only focus on those symmetric with respect to the origin. Compared to the HEALpix method, this leaves us with plenty of different options for a small number of points $N < 100$. Owing to their scalability and connection with spherical harmonics, spherical designs provide a natural way to select ϵ_k .

As an example, a spherical design with 94 points, fully symmetric with respect to the origin that was used for the following measurements is shown in figure 8.4 c). Half of the points are filled, the mirrored other half is shown as empty points. Consequently, one hemisphere contains 47 points in total.

8.3.2 Limitations of the Eulerian cradle and rotated gratings

So far we have not considered the practical limitation of $|\psi| \lesssim 45^\circ$ when performing a measurement with the Eulerian cradle. While the orientation of the gratings with respect to the rotation axis of ψ does not play a role in the unrestricted case, as soon as ψ is limited to some degree, certain grating orientations are more favourable for a measurement than others. In this section, different grating orientations in the plane perpendicular to the illumination are investigated. Mathematically, this corresponds to changing the

8 Iterative directional dark-field tomography

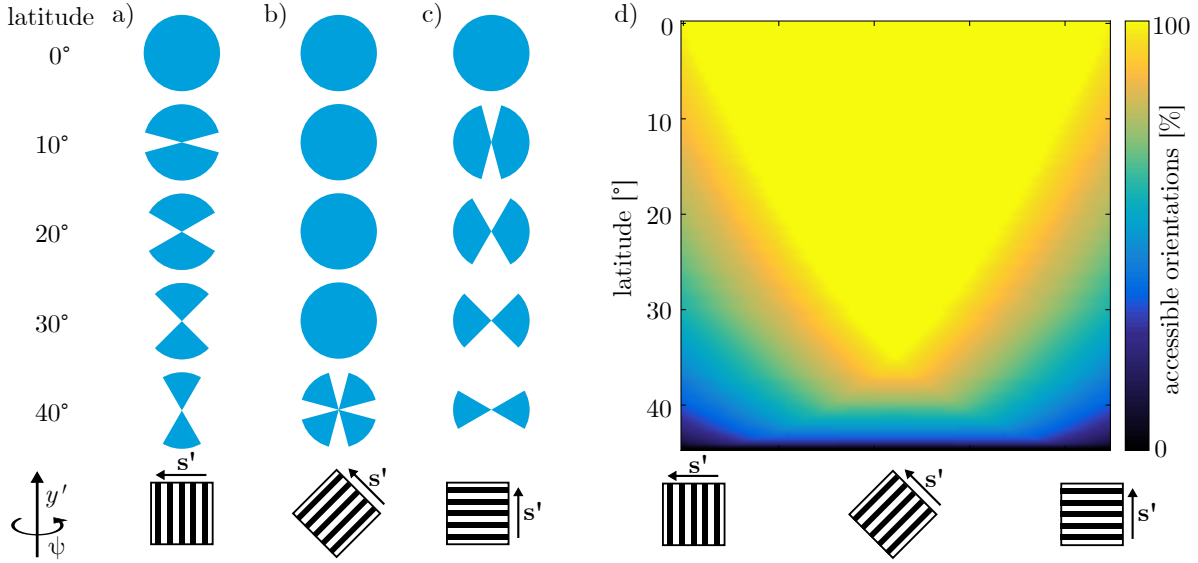


Figure 8.5: **Comparison of different grating sensitivity directions.** A realistic measurement using the Eulerian cradle is limited by $|\psi| \leq 45^\circ$. The fraction of measurable \mathbf{s} orientations at each latitude on the sphere of possible illumination directions \mathbf{t} depends on the grating orientation with respect to the vertical axis. The reachable orientations for three different grating orientations at five different latitudes are shown as circle segments in a)-c). The percentage of accessible scattering orientations for all possible grating sensitivity directions and latitudes up to 45° is given in d). It is clear to see that an angle of 45° between the grating sensitivity direction and rotation axis for ψ offers most accessible orientations overall.

orientation of \mathbf{s}' in the laboratory coordinate systems $x' - y'$ -plane.

Following from the definition of Euler angles used here, as well as the experimental implementation using the Eulerian cradle, the ψ rotation always is around the laboratory y' -axis, i.e. vertical axis. In sample coordinates $|\psi| \leq 45^\circ$ translates to a limitation of points within $\leq 45^\circ$ latitude on the sphere of possible illumination directions \mathbf{t} . Consider once more the representation in figure 8.4 a). If a $|\psi| \leq 45^\circ$ limit was imposed, sample orientations for which the angle between \mathbf{t} and the $x - z$ -plane is $> 45^\circ$ could not be measured.

This does not take the requirement on \mathbf{s} for a certain \mathbf{t} into account yet. Owing to the rotational symmetry of the problem, it is sufficient to limit ourselves to only comparing \mathbf{t} at different latitude at this point. As the distribution of ϵ_k is quasi-isotropic over the entire hemisphere, it is evident that for a complete measurement, many different orientations of \mathbf{s} are required for each latitude. Hence, we take a closer look at the percentage of accessible \mathbf{s} directions for each latitude as a function of grating orientation.

8.4 Imaging of large, strongly scattering objects

This is illustrated for three different grating orientations in figure 8.5 a)-c). The reachable orientations for \mathbf{s} are represented as circle segments. The orientation of the gratings with respect to the rotation axis of ψ is indicated in the bottom row. It is evident that for a higher latitude, less orientations for \mathbf{s} are accessible. However, this decline is more pronounced for grating orientations $\perp y'$ than for the intermediate angle of 45° . A comprehensive study is given in figure 8.5 d). Shown are the results of a simulation with $|\psi|_{\max} = 45^\circ$ for 90 different grating orientations from 0° to 90° and 90 different latitudes from 0° up to 45° . The accessibility of 180 different \mathbf{s} from 0° to 179° was tested, and the resulting percentage of accessible \mathbf{s} orientations is plotted as a function of latitude and grating rotation. This plot reveals an optimal angle between the grating sensitivity direction and rotation axis for ψ of 45° for the proposed acquisition scheme. A comprehensive study of different acquisition schemes confirms these results and is published in:

Sharma, Y., **Schaff, F.**, Wieczorek, M., Pfeiffer, F. & Lasser, T. Design of Acquisition Schemes and Setup Geometry for Anisotropic X-ray Dark-Field Tomography (AXDT). *Accepted for publication in Scientific Reports*

Consequently, all measurements were performed using the novel acquisition scheme based on spherical designs in combination with the optimized grating sensitivity direction.

8.4 Imaging of large, strongly scattering objects

Given its unique signal, dark-field-based imaging is most suited for characterizing microscopic structures in macroscopic objects. For this reason, several studies have used dark-field imaging to investigate e.g. fibrous materials, such as carbon-fibre composites [Revol, 2012; Revol, 2013; Lauridsen, 2014; Kagias, 2016], fibre reinforced polymers [Hanneschläger, 2015; Prade, 2017], or wooden structures [Malecki, 2014a], as well as non-fibrous materials such as concrete [Prade, 2015a; Prade, 2015b; Grumbein, 2016; Prade, 2016], or aluminium weld lines [Revol, 2011].

Likewise, the unique selling point for oriented dark-field tomography is the characterization of microstructural orientations in large objects, which is not possible in a non-destructive way using other methods, such as conventional attenuation-based CT. For a lot of applications, Talbot-Lau grating interferometers are designed to optimize their sensitivity to changes of the interference pattern [Donath, 2009; Modregger, 2011; Birnbacher, 2016]. However, as the size of an object in a grating interferometer increases, so does the integrated dark-field signal, up to a point at which saturation is reached. This is the dark-field equivalent to beam-starvation in attenuation-based CT caused by strongly attenuating objects, such as metals.

Hence, in order to perform directional dark-field tomography experiments on large, strongly

8 Iterative directional dark-field tomography

	conventional setup	low-sensitivity setup
p_0 [μm]	10	-
p_1 [μm]	10	62.5
p_2 [μm]	10	125
type G0	attenuation	microfocus X-ray tube
type G1	π -phaseshift	attenuation
type G2	attenuation	attenuation
distance G0-G1 [mm]	919	878
distance G1-G2 [mm]	919	985
design energy [keV]	45	-

Table 8.1: **Parameters of different grating setups.** The conventional setup is a Talbot-Lau interferometer with a design energy of 45 keV. In contrast, as p_1 is much larger, the low-sensitivity setup does not rely on the Talbot-effect. The intensity modulation in this specific design is directly caused by the alternating attenuation of G1.

scattering objects, the specific sensitivity of the interferometer has to be adjusted accordingly. For the dark-field signal, this is equivalent to a change of the probed autocorrelation length ξ_{GI} . Equation 6.14 shows that this is possible in three different ways, either by changing the wavelength λ of the X-rays, the position of the sample from G2, L_s , or the period of G2, p_2 . Owing to the space required by the Eulerian cradle, L_s can only be adjusted up to a certain point, which has proven to be insufficient for the samples discussed below. The other two parameters, λ and p_2 , cannot be easily changed, as all components in a Talbot-Lau interferometer need to be precisely matched to each other. Therefore, a redesign of the interferometer was required.

8.4.1 Low-Sensitivity setup for directional dark-field tomography

A low-sensitivity setup was designed specifically for the purpose of imaging large, strongly scattering objects. The most important characteristic parameters of this setup are compared to the conventional Talbot-Lau interferometer in table 8.1. In the low-sensitivity setup, a commercially available anti-scatter grid with a period of $p_2 = 125 \mu\text{m}$, as used in clinical CT machines, was used as G2. Just like specifically designed X-ray gratings, the anti-scatter grid consists of periodically spaced, highly attenuating, one-dimensional structures. A practical consequence of using an anti-scatter grid as G2 is an increased field-of-view, which for conventional X-ray gratings requires highly complex production processes [Meiser, 2016]. Rather than a phase-shifting G1, a second attenuation grating with a period of $p_1 = 62.5 \mu\text{m}$ was used here. The main reason for this the quadratic dependency of the Talbot-distance d_T on p_1 (cf. equation 6.1). For the design energy of the conventional setup (45 keV), a grating period of $62.5 \mu\text{m}$ leads to d_T of several hundred

8.4 Imaging of large, strongly scattering objects

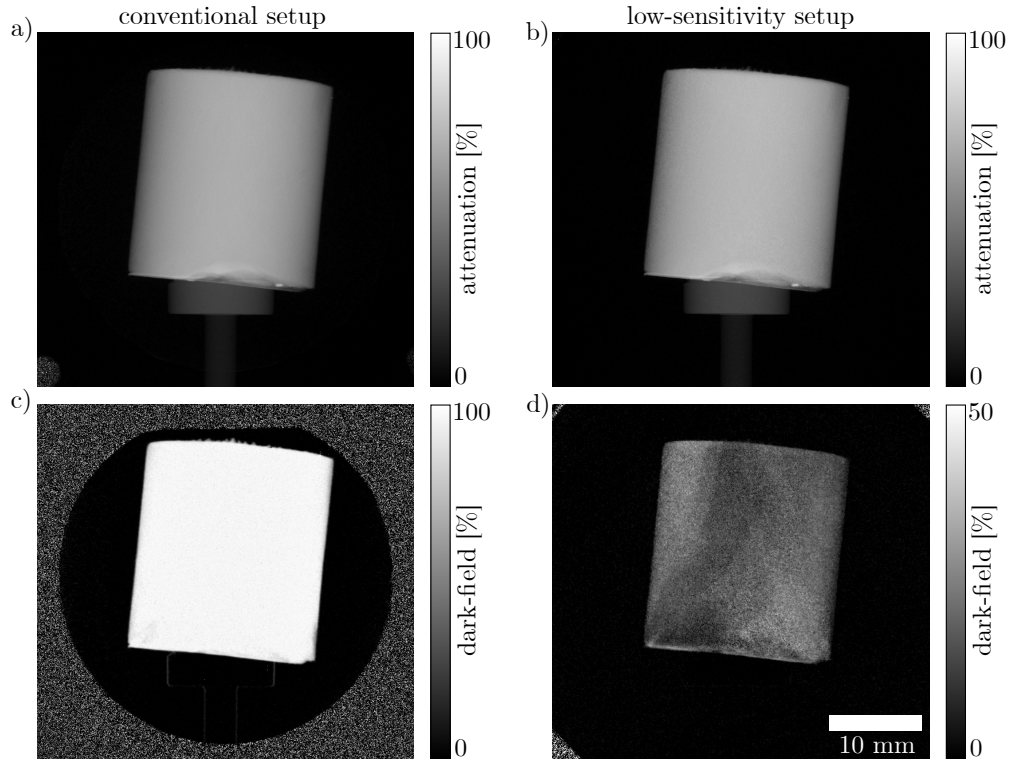


Figure 8.6: **Comparison of conventional and low-sensitivity grating setup.** While attenuation images generated with the conventional (a) and low-sensitivity setup (b) are nearly identical, the dark-field images differ substantially. In the normal setup (c), the dark-field signal is completely saturated. With the low-sensitivity setup (d), the much weaker overall dark-field signal reveals internal structure of the object. Note the different scaling in d).

meters. Hence, it is unrealistic to design the interferometer around the Talbot-effect. Instead, the required intensity modulation is created directly by the alternating attenuation of the X-ray beam behind the attenuation-based G1. In this configuration, the position of G2 has to be close enough to G1 before near-field diffraction effects become noticeable. This was ensured in the low-sensitivity setup by positioning G2 less than a meter behind G1. Another consequence of using an attenuation grating outside the Talbot-regime as G1 is the lack of a specific design energy of the setup. Therefore, much greater flexibility in selecting the wavelength λ of the X-ray radiation is offered by this design. The large periods of G1 and G2 also allowed to omit G0, as the source spot of a microfocus X-ray tube is small enough to not destroy the intensity pattern created behind G1.

With inter-grating distances comparable to those of the conventional setup, imaging experiments under similar geometric conditions, but with greatly reduced sensitivity can be performed with the low-sensitivity setup. A direct comparison of this is given in figure 8.6.

8 Iterative directional dark-field tomography

Attenuation and dark-field images of a highly porous alumina ceramic sample are shown, measured at the conventional setup [a),b)] and the low-sensitivity setup [c),d)]. The position of the X-ray source, the sample, as well as the detector are the same. Consequently, the attenuation images [a),c)] are nearly identical. The slightly lower apparent attenuation in the conventional setup can be accounted to a marginally different energy-spectrum of the illumination compared to that of the low-sensitivity setup. This is caused by the different gratings prior the sample, which also act as a filter to the spectrum of the X-ray tube. Significant differences are visible in the dark-field signal. As the sample is highly porous, the scattering signal is completely saturated in the conventional setup. Previously invisible structural differences within the sample are revealed only in the low-sensitivity setup, owing to the greatly reduced sensitivity.

Besides the clear advantage of lower sensitivity compared to the conventional setup, the previously mentioned increased field-of-view of the low-sensitivity setup¹ aids with recording directional dark-field tomography data of larger objects. For these reasons, all tomography results presented in this chapter were produced using this low-sensitivity, double attenuation grating setup.

8.4.2 Experimental parameters

All results presented in the following were produced using the low-sensitivity setup described here. The gratings were positioned with an angle of 45° between their sensitivity direction and the vertical axis. As demonstrated in the previous section, this allows for an optimized amount of projections to be recorded. Furthermore, an acquisition scheme based on a set of 47 ϵ_k was used for all samples. The exact distribution of the 47 ϵ_k follows a spherical design. For each ϵ_k , 40 measurement directions were distributed circularly around ϵ_k , as shown in figure 8.4. From the 2240 measurement orientations suggested this way, 1124 remain after imposing a practical limit of $|\psi| \leq 40^\circ$. Dark-field and attenuation projections were created from seven individual images using the phase-stepping technique. Each stepping position was exposed for two seconds and images were recorded on a CsI *Varian PaxScan 2520DX* detector with $127 \mu\text{m}$ pixel size. The raw images were binned prior processing by a factor of four in order to improve photon statistics, decrease reconstruction time and facilitate visualization of the results. X-rays were generated using an *X-ray Worx 160-SE* microfocus X-ray tube, run at an acceleration voltage of 60 kV and anode-power of 25 W. These parameters ensured a sufficiently small source spot for the grating experiments. All imaging experiments were conducted with a geometric magnification $M = 1.63$ of the sample. This position corresponds to an autocorrelation length $\xi_{\text{GI}} = 0.146 \mu\text{m}$ for a photon energy of 60 keV.

The reconstructions were calculated with AXDT up to order $l = 4$, i.e. the scattering distributions $df_{\text{rec}}(\epsilon)$ were modelled using 15 different Y_{lm} . Twenty iterations of the conjugate gradient method were used to reconstruct the data [Hestenes, 1952]. Primary structure

¹the low-sensitivity images in figure 8.6 were cropped to match those of the conventional setup

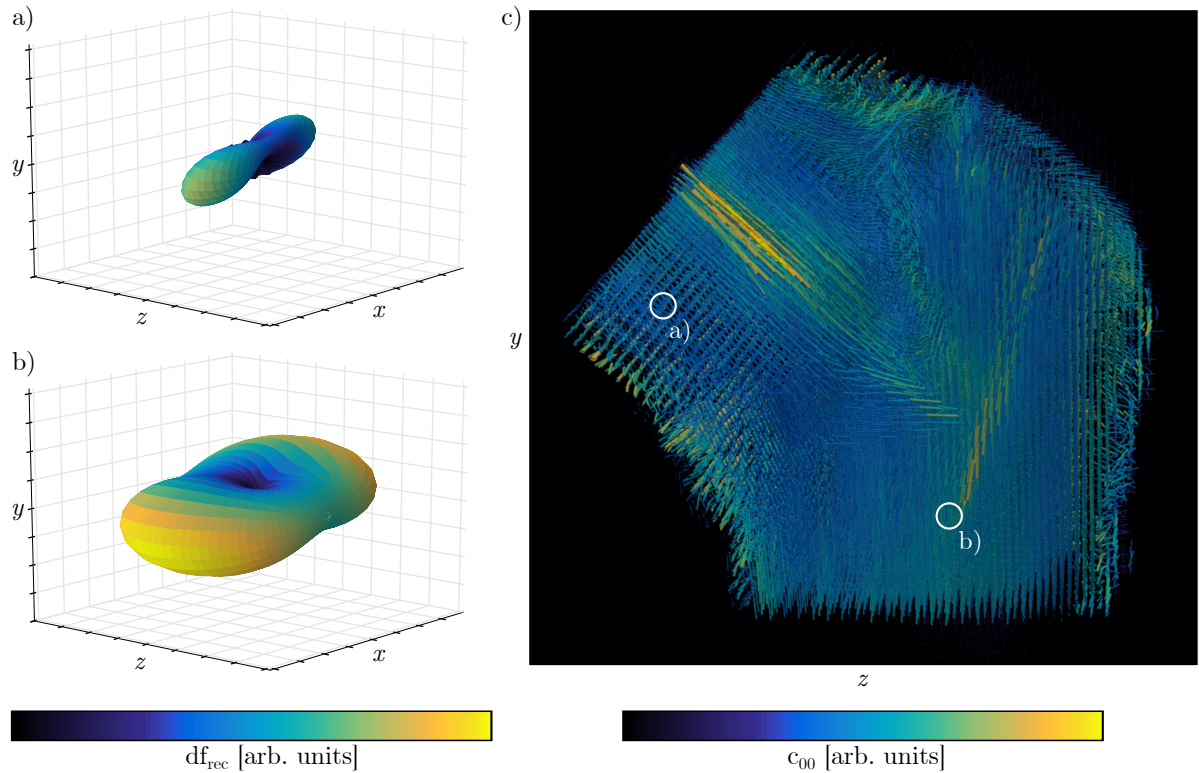


Figure 8.7: **AXDT reconstruction of wooden sample.** Results of a junction between two branches is shown. a) & b) Renderings of the locally reconstructed scattering distributions $df_{\text{rec}}(\epsilon)$ for two points of the sample. Both the magnitude and main orientation of $df_{\text{rec}}(\epsilon)$ differ between a) and b). A vector-field representation of the primary structure orientation is shown in c) half the sample. This way internal structure is visible. The position of points a) and b) is marked. Each vector is coloured by c_{00} . As expected, the wooden fibres follow the long axes of the branches.

orientations are defined in each voxel as the largest local maxima of the Funk-Radon transform of $df_{\text{rec}}(\epsilon)$ [Funk, 1913]. For each spatial direction, this transform calculates the line integral of $df_{\text{rec}}(\epsilon)$ along the great circles perpendicular to this direction. Based on the assumption that the dark-field signal is largest in directions perpendicular to oriented structures, maxima of the Funk-Radon transform coincide with structure orientation.

8.4.3 Wood

Wood consists of many microscopic fibres that give rise to a strong dark-field signal. An approximately $5 \text{ cm} \times 5 \text{ cm} \times 4 \text{ cm}$ large junction between two branches was measured and reconstructed with AXDT. The results are summarized in figure 8.7. Two examples of

8 Iterative directional dark-field tomography

the reconstructed scattering distributions, $df_{\text{rec}}(\epsilon)$, are given in a) and b), whose exact location inside the sample is marked in c). Owing to the use of spherical harmonics, $df_{\text{rec}}(\epsilon)$ is represented as a closed surface, compared to discrete points as e.g. shown in figure 8.1 or the SAXS reconstruction discussed in chapter 5. Just like in figure 8.2, the distance from the centre and colour resemble the magnitude of $df_{\text{rec}}(\epsilon)$. For comparison, $df_{\text{rec}}(\epsilon)$ is scaled to the same value in a) and b). It is clear to see that point b) gives rise to a stronger overall dark-field signal, compared to point a). Furthermore, the direction of least scattering is identified to fall roughly between the y - and z -axis for point a), and almost parallel to the y -axis for point b). Figure 8.7 c) shows the full vector-field of the primary structure orientation, calculated from the Funk-Radon transform. The front half of the sample is hidden to reveal its inner structure. Each bar is coloured and scaled in size according to c_{00} , i.e. the reconstructed magnitude of Y_{00} . This corresponds to the average value of $df_{\text{rec}}(\epsilon)$. With this visualization, the expected separation of wooden fibres into both sides of the junction is clear to see.

8.4.4 Freeze-cast ceramics

Freeze casting is an emerging technique used to create microstructured, porous materials by exploiting the self-assembly of colloids in a slurry during freezing [Deville, 2013]. An excellent overview of the topic is given in [Deville, 2013]. Here, only a brief summary is given. The method is most commonly used to structure alumina ceramics [Fukasawa, 2001; Chino, 2008; Deville, 2013; Lichtner, 2016], although recent studies have shown applicability to titanium foams [Chino, 2008] and bio-inspired materials [Bai, 2016]. Complex pore structures can be created using freeze casting by adjusting the processing parameters, e.g. temperature, or slurry concentration [Fukasawa, 2001]. Increasing understanding of the process lead to the creation of lammellar structures, which allows to enhance an objects mechanical properties along a specific axis while maintaining the highly porous structure [Lichtner, 2016; Bai, 2016]. Objects created via freeze casting way may well be several centimetres in size [Deville, 2013; Lichtner, 2016] and contain pores with typical sizes of up to a few ten micrometres [Fukasawa, 2001; Chino, 2008; Deville, 2013; Lichtner, 2016; Bai, 2016].

Controlling the process remains one of the main challenges of freeze casting [Deville, 2013]. Characterization of the microstructure inside freeze-cast objects poses a significant challenge to traditional non-destructive imaging, owing to the substantial size difference between the microstructures and an entire freeze-cast object. Given the high porosity and electron-density contrast between the bulk material and its pores, objects created from freeze casting give rise to a very strong scattering signal. This is evident from figure 8.6 in which a freeze-cast alumina sample fully saturates the dark-field signal in a conventional Talbot-Lau interferometer. Especially for orientated microstructures as recently created, the use of directional dark-field tomography may potentially assist with further development.

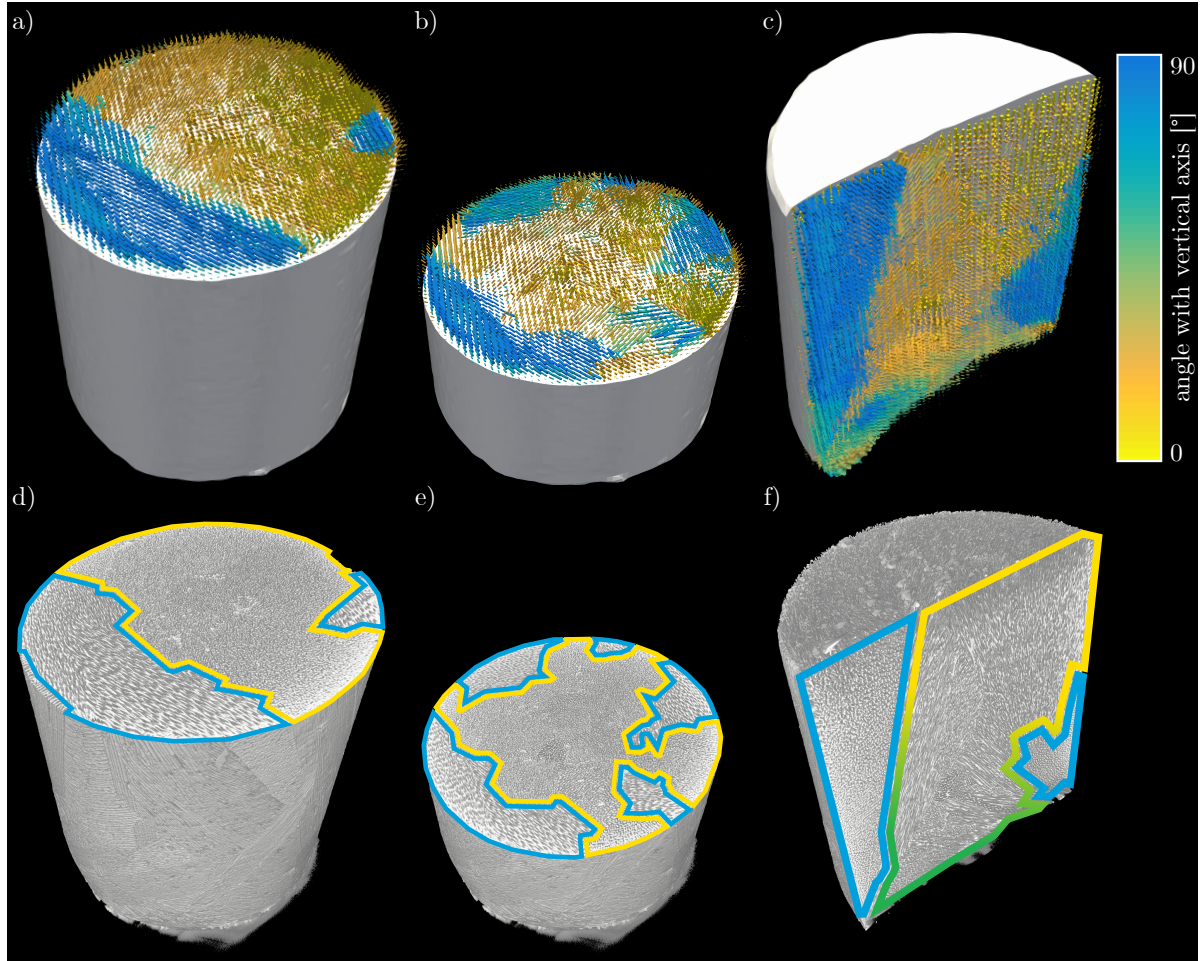


Figure 8.8: **AXDT and micro-CT reconstructions of freeze cast sample.** a)-c) Vectorfield visualization of the AXDT results, overlaid onto a volume rendering of the attenuation reconstruction. Single slices are shown. The angle of each bar with the vertical axis is indicated by its colour. From this, several areas of different structure orientation are visible. d)-f) Volume renderings based on micro-CT data of the same sample. Coloured outlines are added to highlight areas of differently oriented pores in the microstructure. Strong similarity to the AXDT results can be seen. Animations available at <https://www.youtube.com/watch?v=YZWcYjzzCwk> and https://www.youtube.com/watch?v=_7keSaEttDQ.

8 Iterative directional dark-field tomography

A highly porous alumina sample produced by freeze casting was investigated at the low-sensitivity imaging setup with the experimental parameters described above. The sample has a cylindrical shape, with height and diameter of approximately 2 cm and 2 cm, respectively. From the reconstructed scattering distribution in each voxel, a vector field was created using the Funk-Radon transform, analogue to the wooden sample. The top half of figure 8.8 [a)-c)] shows visualizations of this vector field with different parts cropped out. For this, slices through the vectorfield are overlaid onto accordingly sliced volume renderings of the attenuation data. Note that here the colour of each bar indicates its angle with the vertical axis, rather than c_{00} , as was the case in the visualization of the wooden sample. As it is very homogeneous throughout the sample, a colour scaling with c_{00} would not benefit the visualization. Scaling of the vertical angle, however, reveals that there exist large clusters of similarly oriented structures. In order to fully confirm these findings and that the derived structure orientation is valid for this type of sample, an attenuation-based high resolution micro-CT was recorded at a *VersaXRM-500* X-ray microscope by *Xradia*². The three-dimensional resolution of this state-of-the-art machine was sufficient to image the microstructure for this particular sample. Resulting volume renderings are shown in figure 8.8 d)-f). Parts of the sample are cut away at positions that match the AXDT visualizations in a)-c). Areas of similar structural orientation to that revealed by AXDT are visible, marked by borders of the respective colour. Although the resolution of AXDT is more than two orders of magnitude worse than that of the micro-CT reconstruction, the overall structural orientation matches well between the two methods.

Given that the micro-CT directly reveals the microstructure inside the sample, one might be asking whether there is a need for AXDT after all. In that regard it is important to remind ourselves of the relation between resolution and object size once again. A larger sample would lead to a decrease in resolution, which consequently prevents investigation of the microstructure. Although the sample was relatively small compared to e.g. the wooden sample, the settings used during the microCT were close to the feasible limits of the machine. A sample of, say, twice the size could not be imaged using micro-CT. However, as resolution and structure information is uncoupled in dark-field imaging and the sensitivity can be tuned via the grating-period and X-ray energy, the sample size can be scaled up relatively easy in AXDT.

8.5 Discussion

Several improvements in key areas of directional dark-field tomography were covered in this chapter. The replacement of XTT by AXDT offers a much more general approach to the reconstruction, solving the major problem of arbitrarily chosen scattering orientations for reconstruction. As AXDT is developed further, the data acquisition time will have to

²now *Zeiss*

eventually be optimized. The data acquisition schemes presented here can be used as a starting point for future research in this direction, e.g. if there exists a relation between optimal sampling and image resolution as for standard CT. Additionally, the possibility to image strongly scattering, large objects was demonstrated. This is important for the future of AXDT, as the most promising area of application is the characterization of microscopic structures in macroscopic objects, i.e. the area that is out of reach for conventional imaging methods.

It should be noted that orientation-dependent dark-field tomography thus far results in a five-dimensional reconstruction. We set out to model the scattering distribution $df_{\text{rec}}(\epsilon, \mathbf{r})$ in each voxel using spherical harmonics. Given that spherical harmonics are defined on \mathbb{S}^2 , i.e. described by two independent variables, the whole reconstruction can be seen as a five-dimensional function, $\mathbb{S}^2 \times \mathbb{R}^3 \mapsto \mathbb{R}$. However, the dark-field signal depends on a six-dimensional function - the three-dimensional autocorrelation function, as shown in chapter 6.3.2 - inside each voxel of a three-dimensional object. Consider now that in an XTT measurements, the sample is rotated around three independent angles φ, θ , and ψ and dark-field images with two spatial coordinates are recorded. In total, this amounts to only five dimensions, as well. Here, this discrepancy was accounted for by introducing the sine-based weighting function. Although this works reasonably well, one should keep this in mind when dealing with orientation-dependent dark-field CT. A possible way to access the sixth dimensions also for dark-field imaging is given in the final chapter of this thesis.

As already mentioned in the introduction to this chapter, the ongoing development of XTT was done in close collaboration with the CAMP chair at the TUM Department of Informatics. Hence, further discussions on AXDT and acquisition schemes will be published in the upcoming doctoral theses by Matthias Wiczorek and Yash Sharma, respectively.

In conclusion, orientation-dependent computed tomography (CT) of small-angle X-ray scattering (SAXS) and dark-field imaging was covered in this thesis. Theoretical considerations, as well as experimental realization and results were presented.

SAXS imaging at synchrotron sources was treated in the first half of the thesis. After an introduction to fundamental small-angle scattering theory in chapter 2, an overview of different SAXS-imaging techniques was given in chapter 4. The goal of a six-dimensional reconstruction of $\left(\frac{d\sigma}{d\Omega}\right)(\mathbf{q}, \mathbf{r})$ and the need for a new reconstruction method was stated. In the small-angle scattering approximation, the concept of rotational invariance was identified as a fundamental requirement for the direct reconstruction of scattering data parallel to a rotation axis. Based on this, six-dimensional SAXS-CT was presented in chapter 5 as a method to reconstruct $\left(\frac{d\sigma}{d\Omega}\right)(\mathbf{q}, \mathbf{r})$ as a combination of three reciprocal- and three real-space dimensions. A highly efficient way of utilizing most of the recorded data was presented in the concept of virtual tomography axes. Following this theoretical introduction, the method was demonstrated using a dental sample consisting of highly oriented collagen fibres. The required data-processing steps for 6-D SAXS-CT were discussed briefly, and a method to quantify the rotational invariance of the data was extended to the concept of virtual tomography axes. Given the complexity of the reconstructed data, a large section was dedicated to subsequent data analysis of the results. Several different methods to visualize $\left(\frac{d\sigma}{d\Omega}\right)(\mathbf{q}, \mathbf{r})$ were discussed, and, for the first time, the characteristic peak of collagen fibres was visualized in three dimensions. Macroscopic changes of the underlying collagen structure over the entire tooth sample were visualized by extracting the main collagen fibre orientation in each voxel.

Grating-based dark-field imaging with conventional X-ray tubes was covered in the second part of this thesis. The dark-field signal and the system response of grating-based imaging to SAXS was discussed thoroughly in chapter 6. Following this, the concepts derived for 6-D SAXS-CT were, with some preservations and adjustments, applied to directional dark-field tomography in chapter 7. A method without the need of dedicated hardware and highly specialized reconstruction algorithms that is able to provide reconstruction results equivalent to X-ray tensor tomography (XTT) was presented. The common problem of arbitrary sample positioning was rendered possible with the help of an auxiliary spherical sample holder. This approach substantially lowers the entry hurdle to directional dark-field tomography, given that it relies solely on commercially available image processing software and minimal additional hardware. As a last topic, the ongoing development of XTT was covered in chapter 8. First of all, the XTT reconstruction was successfully

9 Conclusion

replaced by spherical harmonics-based anisotropic X-ray dark-field tomography (AXDT). Several issues encountered with reconstructing arbitrarily chosen scattering orientations in XTT are avoided in AXDT. Furthermore, the data acquisition step for AXDT was investigated. A reconstruction scheme aimed at optimizing the measured data, as well as subsequent adjustment to the orientation of the utilized gratings were presented. These enhancements were used in combination with an experimental setup characterized by substantially reduced sensitivity to demonstrate the potential of AXDT to investigate large, strongly scattering objects. Imaging results of a scientifically relevant freeze-cast sample were presented. As one of the most promising areas of application for directional dark-field tomography is the investigation of oriented microstructures inside comparatively much larger objects, this is an important first step into that direction.

Besides the technical differences between SAXS and dark-field imaging, the length scales covered by the different methods are complementary. Six-dimensional SAXS-CT excels at characterizing the nanomorphology in up millimetre sized objects. In contrast, dark-field imaging methods are more suited for the characterization of micrometre sized structures in objects several centimetre in size. Both methods, therefore, bridge many orders of magnitude between structure and object size. Future developments may be able to increase the field of view for both methods, in particular for dark-field imaging. Unless a better way is found, increasing the resolution and field of view in SAXS imaging will ultimately be limited by the slow process of raster scanning. This restriction is not nearly as prominent in dark-field imaging, given that it is a full-field technique.

Outlook

Although the methods presented for SAXS imaging and dark-field imaging are conceptually different, there exist many similar recurring problems. One of them is the task of designing an optimal way to acquire data. Although the rotational invariance of individual scattering orientations is a strong argument for the data acquisition schemes used here, no attention was paid to the total number of measured projections, scattering orientations, and their distribution in three-dimensional space. Answers to these questions will be important on the way to optimized acquisition times. Another common denominator is the problem of data analysis and visualization. Owing to the high dimensionality of the reconstructions, data analysis is a crucial part of extracting meaningful results from the vast amounts of information contained in the reconstructed data. Likewise, a clear visualization is essential to understanding the reconstruction results. New concepts in this area will certainly help improve the understandability of orientation-dependant computed tomography.

For SAXS in particular, a spherical-harmonics based reconstruction method was developed by Liebi et al. simultaneously to 6-D SAXS-CT [Liebi, 2015]. A comparison between the two methods definitely is of interest, especially with respect to the required raw data. Similarly, owing to its generality, the potential application of the AXDT framework with

an adjusted weighting function to SAXS data could be subject to future investigations. A fundamental issue found in dark-field imaging is the fact that there is a missing degree of freedom in the measured data. This discrepancy thus far was handled by a sine-based weighting function, which works sufficiently well most of the times. However, different weighting functions might prove to be more successful in the future if one accepts the fact of a five-dimensional reconstruction. A complete six-dimensional reconstruction could be achieved in the future by adding a sixth independent measurement variable. This can be done as a translation of the sample along the X-ray beam-axis, or by combining measurements at different X-ray energies. Subsequent adjustments of the reconstruction algorithm would have to be done.

Given that research in the field of oriented scattering tomography is in a very early stage, plenty of potential for optimization exists throughout the different methods. Nonetheless, the combination of scattering information with computed tomography provides a unique tool for the study of hierarchically structured materials. First demonstrations on collagen and freeze cast samples have shown promising results so far. One of the next steps is to establish these methods and potentially answer specific scientific questions with the help of this new type of imaging.

Bibliography

- [AlsNielsen, 2011] Als-Nielsen, J. & McMorrow, D. *Elements of Modern X-ray Physics* (Wiley, 2011) (Cited on pages [5](#), [7](#), [8](#), [10–13](#), [15](#), [17](#), [20](#)).
- [Andersson, 2008] Andersson, R., van Heijkamp, L. F., de Schepper, I. M. & Bouwman, W. G. Analysis of spin-echo small-angle neutron scattering measurements. *Journal of Applied Crystallography* **41**, 868–885 (2008) (Cited on page [77](#)).
- [Bai, 2016] Bai, H. *et al.* Bioinspired Hydroxyapatite/Poly(methyl methacrylate) Composite with a Nacre-Mimetic Architecture by a Bidirectional Freezing Method. *Advanced Materials* **28**, 50–56 (2016) (Cited on page [110](#)).
- [BasilJones, 2010] Basil-Jones, M. M. *et al.* Leather Structure Determination by Small-Angle X-ray Scattering (SAXS): Cross Sections of Ovine and Bovine Leather. *Journal of Agricultural and Food Chemistry* **58**, 5286–5291 (2010) (Cited on page [31](#)).
- [Bates, 2016] Bates, A. P., Khalid, Z. & Kennedy, R. A. An Optimal Dimensionality Sampling Scheme on the Sphere with Accurate and Efficient Spherical Harmonic Transform for Diffusion MRI. *IEEE Signal Processing Letters* **23**, 15–19 (2016) (Cited on page [58](#)).
- [Bayer, 2014] Bayer, F. L. *et al.* Reconstruction of scalar and vectorial components in X-ray dark-field tomography. *Proceedings of the National Academy of Sciences* **111**, 12699–12704 (2014) (Cited on page [85](#)).
- [Bech, 2009] Bech, M. *X-Ray imaging with a grating interferometer* (PhD Thesis, 2009) (Cited on pages [14](#), [71](#), [75](#), [76](#)).
- [Bech, 2010] Bech, M. *et al.* Quantitative x-ray dark-field computed tomography. *Physics in Medicine and Biology* **55**, 5529–5539 (2010) (Cited on page [2](#)).
- [Birnbacher, 2016] Birnbacher, L. *et al.* Experimental Realisation of High-sensitivity Laboratory X-ray Grating-based Phase-contrast Computed Tomography. *Scientific Reports* **6**, 24022 (2016) (Cited on pages [69](#), [105](#)).

BIBLIOGRAPHY

- [Boote, 2004] Boote, C., Dennis, S. & Meek, K. Spatial mapping of collagen fibril organisation in primate cornea -an X-ray diffraction investigation. *Journal of Structural Biology* **146**, 359–367 (2004) (Cited on page 31).
- [Bouwman, 2002] Bouwman, W. *et al.* First quantitative test of spin-echo small-angle neutron scattering. *Applied Physics A: Materials Science & Processing* **74**, s115–s117 (2002) (Cited on page 77).
- [Bouwman, 1999] Bouwman, W. G., Kraan, W. & Rekveldt, M. Spin echo small angle neutron scattering experiment. *Physica B: Condensed Matter* **267-268**, 79–83 (1999) (Cited on page 77).
- [Bunk, 2009] Bunk, O. *et al.* Multimodal x-ray scatter imaging. *New Journal of Physics* **11**, 123016 (2009) (Cited on pages 2, 31, 32, 39).
- [Chino, 2008] Chino, Y. & Dunand, D. C. Directionally freeze-cast titanium foam with aligned, elongated pores. *Acta Materialia* **56**, 105–113 (2008) (Cited on page 110).
- [Cloetens, 1997] Cloetens, P., Guigay, J. P., De Martino, C., Baruchel, J. & Schlenker, M. Fractional Talbot imaging of phase gratings with hard x rays. *Optics Letters* **22**, 1059 (1997) (Cited on page 71).
- [David, 2002] David, C., Nöhammer, B., Solak, H. H. & Ziegler, E. Differential x-ray phase contrast imaging using a shearing interferometer. *Applied Physics Letters* **81**, 3287–3289 (2002) (Cited on page 69).
- [Deville, 2013] Deville, S. Ice-templating, freeze casting: Beyond materials processing. *Journal of Materials Research* **28**, 2202–2219 (2013) (Cited on page 110).
- [Dinapoli, 2011] Dinapoli, R. *et al.* EIGER: Next generation single photon counting detector for X-ray applications. *Nuclear Instruments and Methods in Physics Research Section A: Accelerators, Spectrometers, Detectors and Associated Equipment* **650**, 79–83 (2011) (Cited on page 66).
- [Donath, 2009] Donath, T. *et al.* Inverse geometry for grating-based x-ray phase-contrast imaging. *Journal of Applied Physics* **106**, 054703 (2009) (Cited on page 105).
- [Dumont, 2006] Dumont, M., Steuwer, A., Deschamps, A., Peel, M. & Withers, P. Microstructure mapping in friction stir welds of 7449 aluminium alloy using SAXS. *Acta Materialia* **54**, 4793–4801 (2006) (Cited on page 31).

- [Eikenberry, 2003] Eikenberry, E. *et al.* PILATUS: a two-dimensional X-ray detector for macromolecular crystallography. *Nuclear Instruments and Methods in Physics Research Section A: Accelerators, Spectrometers, Detectors and Associated Equipment* **501**, 260–266 (2003) (Cited on page 46).
- [Feigin, 1987] Feigin, L. & Svergun, D. *Structure Analysis by Small-Angle X-Ray and Neutron Scattering* (Springer, 1987) (Cited on pages 5, 10).
- [Feldkamp, 2009] Feldkamp, J. M. *et al.* Recent developments in tomographic small-angle X-ray scattering. *physica status solidi (a)* **206**, 1723–1726 (2009) (Cited on pages 2, 36, 37, 39).
- [Feldkamp, 2011] Feldkamp, J. *Scanning Small-Angle X-Ray Scattering Tomography* (PhD Thesis, 2011) (Cited on pages 10, 12, 13, 28, 41, 52, 53).
- [Fischer, 2005] Fischer, G. *Lineare Algebra, 15. Auflage* (vieweg, 2005) (Cited on page 26).
- [Fratzl, 1997] Fratzl, P., Jakob, H. F., Rinnerthaler, S., Roschger, P. & Klaushofer, K. Position-Resolved Small-Angle X-ray Scattering of Complex Biological Materials. *Journal of Applied Crystallography* **30**, 765–769 (1997) (Cited on pages 1, 2, 30–32, 39, 43, 44).
- [Fratzl, 2003] Fratzl, P. Small-angle scattering in materials science - a short review of applications in alloys, ceramics and composite materials. *Journal of Applied Crystallography* **36**, 397–404 (2003) (Cited on page 31).
- [Fratzl, 2007] Fratzl, P. & Weinkamer, R. Nature's hierarchical materials. *Progress in Materials Science* **52**, 1263–1334 (2007) (Cited on page 44).
- [Fukasawa, 2001] Fukasawa, T., Ando, M., Ohji, T. & Kanzaki, S. Synthesis of Porous Ceramics with Complex Pore Structure by Freeze-Dry Processing. *Journal of the American Ceramic Society* **84**, 230–232 (2001) (Cited on page 110).
- [Funk, 1913] Funk, P. Über Flächen mit lauter geschlossenen geodätischen Linien. *Mathematische Annalen* **74**, 278–300 (1913) (Cited on pages 101, 109).
- [Gaiser, 2012] Gaiser, S., Deyhle, H., Bunk, O., White, S. N. & Müller, B. Understanding Nano-Anatomy of Healthy and Carious Human Teeth: a Prerequisite for Nanodentistry. *Biointerphases* **7**, 4 (2012) (Cited on pages 43, 44, 64).

BIBLIOGRAPHY

- [Georgiadis, 2015] Georgiadis, M. *et al.* 3D scanning SAXS: A novel method for the assessment of bone ultrastructure orientation. *Bone* **71**, 42–52 (2015) (Cited on pages 32, 39).
- [Giannini, 2012] Giannini, C. *et al.* Correlative Light and Scanning X-Ray Scattering Microscopy of Healthy and Pathologic Human Bone Sections. *Scientific Reports* **2**, 435 (2012) (Cited on page 31).
- [Glatter, 1982] Glatter, O. & Kratky, O. *Small Angle X-Ray Scattering* (Academic Press, 1982) (Cited on pages 5, 7, 9, 11, 27, 28).
- [Gorski, 2005] Gorski, K. M. *et al.* HEALPix: A Framework for High-Resolution Discretization and Fast Analysis of Data Distributed on the Sphere. *The Astrophysical Journal* **622**, 759–771 (2005) (Cited on page 58).
- [Grumbein, 2016] Grumbein, S. *et al.* Hydrophobic Properties of Biofilm-Enriched Hybrid Mortar. *Advanced Materials* **28**, 8138–8143 (2016) (Cited on page 105).
- [Guinier, 1955] Guinier, A. & Fournet, G. *Small-angle scattering of X-rays* (Wiley, 1955) (Cited on pages 5, 10, 27, 39).
- [GuizarSicairos, 2015] Guizar-Sicairos, M. *et al.* Quantitative interior x-ray nanotomography by a hybrid imaging technique. *Optica* **2**, 259 (2015) (Cited on page 52).
- [Hanneschläger, 2015] Hanneschläger, C., Revol, V., Plank, B., Salaberger, D. & Kastner, J. Fibre structure characterisation of injection moulded short fibre-reinforced polymers by X-ray scatter dark field tomography. *Case Studies in Nondestructive Testing and Evaluation* **3**, 34–41 (2015) (Cited on pages 2, 105).
- [Hardin, 1996] Hardin, R. H. & Sloane, N. J. A. McLaren’s improved snub cube and other new spherical designs in three dimensions. *Discrete & Computational Geometry* **15**, 429–441 (1996) (Cited on page 103).
- [Hestenes, 1952] Hestenes, M. & Stiefel, E. Methods of conjugate gradients for solving linear systems. *Journal of Research of the National Bureau of Standards* **49**, 409 (1952) (Cited on page 108).
- [Jahns, 1979] Jahns, J. & Lohmann, A. The Lau effect (a diffraction experiment with incoherent illumination). *Optics Communications* **28**, 263–267 (1979) (Cited on pages 71, 74).
- [Jensen, 2011a] Jensen, T. *et al.* Molecular X-ray computed tomography of myelin in a rat brain. *NeuroImage* **57**, 124–129 (2011) (Cited on pages 2, 36, 39).

- [Jensen, 2010a] Jensen, T. H. *et al.* Directional x-ray dark-field imaging of strongly ordered systems. *Physical Review B* **82**, 214103 (2010) (Cited on pages 2, 69).
- [Jensen, 2011b] Jensen, T. H. *et al.* Brain tumor imaging using small-angle x-ray scattering tomography. *Physics in Medicine and Biology* **56**, 1717–1726 (2011) (Cited on pages 2, 36, 38, 39).
- [Jensen, 2010b] Jensen, T. H. *et al.* Directional x-ray dark-field imaging. *Physics in Medicine and Biology* **55**, 3317–3323 (2010) (Cited on pages 2, 69).
- [Jud, 2016] Jud, C. *et al.* Dentinal tubules revealed with X-ray tensor tomography. *Dental Materials* **32**, 1189–1195 (2016) (Cited on pages 94, 98, 99, 101).
- [Kagias, 2016] Kagias, M., Wang, Z., Villanueva-Perez, P., Jefimovs, K. & Stamparoni, M. 2D-Omnidirectional Hard-X-Ray Scattering Sensitivity in a Single Shot. *Physical Review Letters* **116**, 093902 (2016) (Cited on pages 70, 72, 74, 105).
- [Kieffer, 2013] Kieffer, J. & Karkoulis, D. PyFAI, a versatile library for azimuthal regrouping. *Journal of Physics: Conference Series* **425**, 202012 (2013) (Cited on page 49).
- [Kinney, 2001] Kinney, J., Pople, J., Marshall, G. & Marshall, S. Collagen Orientation and Crystallite Size in Human Dentin: A Small Angle X-ray Scattering Study. *Calcified Tissue International* **69**, 31–37 (2001) (Cited on pages 1, 31, 43, 44).
- [Krouglov, 2003] Krouglov, T., de Schepper, I. M., Bouwman, W. G. & Rekveldt, M. T. Real-space interpretation of spin-echo small-angle neutron scattering. *Journal of Applied Crystallography* **36**, 117–124 (2003) (Cited on page 77).
- [Lauridsen, 2014] Lauridsen, T., Lauridsen, E. M. & Feidenhans'l, R. Mapping misoriented fibers using X-ray dark field tomography. *Applied Physics A* **115**, 741–745 (2014) (Cited on pages 2, 85, 105).
- [Lichtner, 2016] Lichtner, A., Roussel, D., Jauffrès, D., Martin, C. L. & Bordia, R. K. Effect of Macropore Anisotropy on the Mechanical Response of Hierarchically Porous Ceramics. *Journal of the American Ceramic Society* **99** (ed Franks, G.) 979–987 (2016) (Cited on page 110).
- [Liebi, 2015] Liebi, M. *et al.* Nanostructure surveys of macroscopic specimens by small-angle scattering tensor tomography. *Nature* **527**, 349–352 (2015) (Cited on page 116).

BIBLIOGRAPHY

- [Liu, 2010] Liu, Y. *et al.* Mineral crystal alignment in mineralized fracture callus determined by 3D small-angle X-ray scattering. *Journal of Physics: Conference Series* **247**, 012031 (2010) (Cited on pages [32](#), [39](#)).
- [Livet, 2007] Livet, F. Diffraction with a coherent X-ray beam: dynamics and imaging. *Acta Crystallographica Section A Foundations of Crystallography* **63**, 87–107 (2007) (Cited on page [13](#)).
- [Lohmann, 1990] Lohmann, A. W. & Thomas, J. A. Making an array illuminator based on the Talbot effect. *Applied Optics* **29**, 4337 (1990) (Cited on page [71](#)).
- [Loidl, 2005] Loidl, D. *et al.* Structure and mechanical properties of carbon fibres: a review of recent microbeam diffraction studies with synchrotron radiation. *Journal of Synchrotron Radiation* **12**, 758–764 (2005) (Cited on page [31](#)).
- [LorenzHaas, 2003] Lorenz-Haas, C. *et al.* Scanning Microfocus Small-Angle X-ray Scattering: A New Tool To Investigate Defects at Polymer-Polymer Interfaces. *Langmuir* **19**, 3056–3061 (2003) (Cited on pages [31](#), [39](#)).
- [LutzBueno, 2016] Lutz-Bueno, V. *et al.* Scanning-SAXS of microfluidic flows: nanostructural mapping of soft matter. *Lab Chip* **16**, 4028–4035 (2016) (Cited on pages [31](#), [39](#)).
- [Lynch, 2011] Lynch, S. K. *et al.* Interpretation of dark-field contrast and particle-size selectivity in grating interferometers. *Applied Optics* **50**, 4310 (2011) (Cited on pages [77](#), [78](#)).
- [Malecki, 2012] Malecki, A., Potdevin, G. & Pfeiffer, F. Quantitative wave-optical numerical analysis of the dark-field signal in grating-based X-ray interferometry. *EPL (Europhysics Letters)* **99**, 48001 (2012) (Cited on page [77](#)).
- [Malecki, 2013] Malecki, A. *X-Ray Tensor Tomography* (PhD Thesis, 2013) (Cited on pages [3](#), [13](#), [85](#), [97](#), [98](#)).
- [Malecki, 2014a] Malecki, A. *et al.* Correlation of X-Ray Dark-Field Radiography to Mechanical Sample Properties. *Microscopy and Microanalysis* **20**, 1528–1533 (2014) (Cited on page [105](#)).
- [Malecki, 2014b] Malecki, A. *et al.* X-ray tensor tomography. *EPL (Europhysics Letters)* **105**, 38002 (2014) (Cited on pages [3](#), [85](#), [92](#), [97–99](#), [101](#)).

- [Märten, 2010] Märten, A., Fratzl, P., Paris, O. & Zaslansky, P. On the mineral in collagen of human crown dentine. *Biomaterials* **31**, 5479–5490 (2010) (Cited on pages 31, 43, 44).
- [Martin, 2016] Martin, H. P. *et al.* Microfluidic processing of concentrated surfactant mixtures: online SAXS, microscopy and rheology. *Soft Matter* **12**, 1750–1758 (2016) (Cited on pages 31, 39).
- [Martinez, 2007] Martinez, J. L., Reina, A. & Mandow, A. *Spherical Laser Point Sampling with Application to 3D Scene Genetic Registration in Proceedings 2007 IEEE International Conference on Robotics and Automation* (IEEE, 2007), 1104–1109 (Cited on page 58).
- [Meek, 2009] Meek, K. M. & Boote, C. The use of X-ray scattering techniques to quantify the orientation and distribution of collagen in the corneal stroma. *Progress in Retinal and Eye Research* **28**, 369–392 (2009) (Cited on page 31).
- [Meiser, 2016] Meiser, J. *et al.* Increasing the field of view in grating based X-ray phase contrast imaging using stitched gratings. *Journal of X-Ray Science and Technology* **24**, 379–388 (2016) (Cited on page 106).
- [Modregger, 2014] Modregger, P., Rutishauser, S., Meiser, J., David, C. & Stampf, M. Two-dimensional ultra-small angle X-ray scattering with grating interferometry. *Applied Physics Letters* **105**, 024102 (2014) (Cited on page 70).
- [Modregger, 2011] Modregger, P. *et al.* Sensitivity of X-ray grating interferometry. *Optics Express* **19**, 18324 (2011) (Cited on page 105).
- [Momose, 2003] Momose, A. Phase-sensitive imaging and phase tomography using X-ray interferometers. *Optics Express* **11**, 2303 (2003) (Cited on page 69).
- [Momose, 2003] Momose, A. *et al.* Demonstration of X-Ray Talbot Interferometry. *Japanese Journal of Applied Physics* **42**, L866–L868 (2003) (Cited on pages 69, 73).
- [Morris, 2005] Morris, R. J., Najmanovich, R. J., Kahraman, A. & Thornton, J. M. Real spherical harmonic expansion coefficients as 3D shape descriptors for protein binding pocket and ligand comparisons. *Bioinformatics* **21**, 2347–2355 (2005) (Cited on page 58).
- [Nobel Prize, 1901] Nobelprize.org. Nobel Media AB 2014. *The Nobel Prize in Physics 1901* http://www.nobelprize.org/nobel_prizes/physics/laureates/1901/ (2017) (Cited on page 1).

BIBLIOGRAPHY

- [Nobel Prize, 1979] Nobelprize.org. Nobel Media AB 2014. *The Nobel Prize in Physiology or Medicine 1979* http://www.nobelprize.org/nobel_prizes/medicine/laureates/1979/ (2017) (Cited on page 1).
- [Paganin, 2006] Paganin, D. *Coherent X-Ray Optics* (Oxford University Press (OUP), 2006) (Cited on page 12).
- [Pauw, 2013] Pauw, B. R. Everything SAXS: small-angle scattering pattern collection and correction. *Journal of Physics: Condensed Matter* **25**, 383201 (2013) (Cited on page 28).
- [Pfeiffer, 2006] Pfeiffer, F., Weitkamp, T., Bunk, O. & David, C. Phase retrieval and differential phase-contrast imaging with low-brilliance X-ray sources. *Nature Physics* **2**, 258–261 (2006) (Cited on pages 14, 69, 73).
- [Pfeiffer, 2008] Pfeiffer, F. *et al.* Hard-X-ray dark-field imaging using a grating interferometer. *Nature Materials* **7**, 134–137 (2008) (Cited on pages 2, 69, 76, 77).
- [Prade, 2015a] Prade, F., Chabior, M., Malm, F., Grosse, C. & Pfeiffer, F. Observing the setting and hardening of cementitious materials by X-ray dark-field radiography. *Cement and Concrete Research* **74**, 19–25 (2015) (Cited on page 105).
- [Prade, 2015b] Prade, F., Yaroshenko, A., Herzen, J. & Pfeiffer, F. Short-range order in mesoscale systems probed by X-ray grating interferometry. *EPL (Europhysics Letters)* **112**, 68002 (2015) (Cited on pages 2, 69, 77, 79, 83, 105).
- [Prade, 2017] Prade, F. *et al.* Nondestructive characterization of fiber orientation in short fiber reinforced polymer composites with X-ray vector radiography. *NDT & E International* **86**, 65–72 (2017) (Cited on page 105).
- [Prade, 2016] Prade, F. *et al.* Time resolved X-ray Dark-Field Tomography Revealing Water Transport in a Fresh Cement Sample. *Scientific Reports* **6**, 29108 (2016) (Cited on page 105).
- [Qingde Li, 2004] Qingde Li & Griffiths, J. *Least squares ellipsoid specific fitting in Geometric Modeling and Processing, 2004. Proceedings 2004* (IEEE, 2004), 335–340 (Cited on page 64).
- [Rekveltdt, 2003] Rekveltdt, M. T. *et al.* in *Neutron Spin Echo Spectroscopy: Basics, Trends and Applications* (eds Mezei, F., Pappas, C. & Gutberlet, T.) 87–99 (Springer Berlin Heidelberg, Berlin, Heidelberg, 2003) (Cited on page 83).

- [Rekvelدت, 1996] Rekvelدت, M. Novel SANS instrument using Neutron Spin Echo. *Nuclear Instruments and Methods in Physics Research Section B: Beam Interactions with Materials and Atoms* **114**, 366–370 (1996) (Cited on page 77).
- [Revol, 2012] Revol, V., Kottler, C., Kaufmann, R., Neels, A. & Dommann, A. Orientation-selective X-ray dark field imaging of ordered systems. *Journal of Applied Physics* **112**, 114903 (2012) (Cited on page 105).
- [Revol, 2011] Revol, V. *et al.* Sub-pixel porosity revealed by x-ray scatter dark field imaging. *Journal of Applied Physics* **110**, 044912 (2011) (Cited on pages 2, 105).
- [Revol, 2013] Revol, V. *et al.* Laminate fibre structure characterisation of carbon fibre-reinforced polymers by X-ray scatter dark field imaging with a grating interferometer. *NDT & E International* **58**, 64–71 (2013) (Cited on pages 85, 105).
- [Rinnerthaler, 1999] Rinnerthaler, S. *et al.* Scanning Small Angle X-ray Scattering Analysis of Human Bone Sections. *Calcified Tissue International* **64**, 422–429 (1999) (Cited on pages 1, 31, 39, 43, 44).
- [Rudin, 1992] Rudin, L. I., Osher, S. & Fatemi, E. Nonlinear total variation based noise removal algorithms. *Physica D: Nonlinear Phenomena* **60**, 259–268 (1992) (Cited on page 60).
- [Scholkmann, 2014] Scholkmann, F., Revol, V., Kaufmann, R., Baronowski, H. & Kottler, C. A new method for fusion, denoising and enhancement of x-ray images retrieved from Talbot-Lau grating interferometry. *Physics in Medicine and Biology* **59**, 1425–1440 (2014) (Cited on page 2).
- [Schroer, 2006] Schroer, C. G. *et al.* Mapping the local nanostructure inside a specimen by tomographic small-angle x-ray scattering. *Applied Physics Letters* **88**, 164102 (2006) (Cited on pages 2, 39).
- [Schüttler, 2016] Schüttler, M. *et al.* Height control for small periodic structures using x-ray radiography. *Measurement Science and Technology* **27**, 025015 (2016) (Cited on page 72).
- [Shao, 1996] Shao, M.-z. & Badler, N. I. Spherical Sampling by Archimedes' Theorem. *Technical Reports (CIS)*, Univ. of Pennsylvania, 11 (1996) (Cited on page 58).
- [Sidky, 2009] Sidky, E. Y., Kao, C.-M. & Pan, X. Accurate image reconstruction from few-views and limited-angle data in divergent-beam CT. *Journal of X-ray Science and Technology*, 119–139 (2009) (Cited on page 60).

BIBLIOGRAPHY

- [Sivia, 2011] Sivia, D. *Elementary Scattering Theory: For X-ray and Neutron Users* (Oxford University Press, 2011) (Cited on pages 5, 7).
- [Stribeck, 2006] Stribeck, N. *et al.* Volume-Resolved Nanostructure Survey of a Polymer Part by Means of SAXS Microtomography. *Macromolecular Chemistry and Physics* **207**, 1139–1149 (2006) (Cited on pages 2, 39).
- [Strobl, 2014] Strobl, M. General solution for quantitative dark-field contrast imaging with grating interferometers. *Scientific Reports* **4**, 7243 (2014) (Cited on pages 2, 69, 77–79, 83).
- [Su, 2014] Su, H.-N. *et al.* The ultrastructure of type I collagen at nanoscale: large or small D-spacing distribution? *Nanoscale* **6**, 8134–8139 (2014) (Cited on page 44).
- [Suleski, 1997] Suleski, T. J. Generation of Lohmann images from binary-phase Talbot array illuminators. *Applied Optics* **36**, 4686 (1997) (Cited on page 71).
- [Tegmark, 1996] Tegmark, M. An Icosahedron-based Method for Pixelizing the Celestial Sphere. *The Astrophysical Journal* **470**, L81–L84 (1996) (Cited on page 58).
- [Vogel, 2015] Vogel, J. *et al.* Constrained X-ray tensor tomography reconstruction. *Optics Express* **23**, 15134 (2015) (Cited on pages 85, 92, 98, 99, 101).
- [Wagermaier, 2007] Wagermaier, W. *et al.* Scanning texture analysis of lamellar bone using microbeam synchrotron X-ray radiation. *Journal of Applied Crystallography* **40**, 115–120 (2007) (Cited on pages 32, 39).
- [Wang, 2009] Wang, Z.-T., Kang, K.-J., Huang, Z.-F. & Chen, Z.-Q. Quantitative grating-based x-ray dark-field computed tomography. *Applied Physics Letters* **95**, 094105 (2009) (Cited on page 2).
- [Warren, 1990] Warren, B. E. *X-Ray Diffraction (Dover Books on Physics)* (Dover Publications, 1990) (Cited on pages 5, 8).
- [Weitkamp, 2005] Weitkamp, T. *et al.* X-ray phase imaging with a grating interferometer. *Optics Express* **13**, 6296 (2005) (Cited on pages 69, 72, 73).
- [Wieczorek, 2016] Wieczorek, M., Schaff, F., Pfeiffer, F. & Lasser, T. Anisotropic X-Ray Dark-Field Tomography: A Continuous Model and its Discretization. *Physical Review Letters* **117**, 158101 (2016) (Cited on pages 99, 100).

- [Wolf, 2015] Wolf, J. *et al.* Lens-term- and edge-effect in X-ray grating interferometry. *Biomedical Optics Express* **6**, 4812 (2015) (Cited on page 77).
- [Yang, 2012] Yang, Y. & Tang, X. The second-order differential phase contrast and its retrieval for imaging with x-ray Talbot interferometry. *Medical Physics* **39**, 7237–7253 (2012) (Cited on page 77).
- [Yashiro, 2010] Yashiro, W., Terui, Y., Kawabata, K. & Momose, A. On the origin of visibility contrast in x-ray Talbot interferometry. *Optics Express* **18**, 16890 (2010) (Cited on page 77).
- [Yashiro, 2015] Yashiro, W., Vagovič, P. & Momose, A. Effect of beam hardening on a visibility-contrast image obtained by X-ray grating interferometry. *Optics Express* **23**, 23462 (2015) (Cited on page 77).
- [Yashiro, 2011] Yashiro, W. *et al.* Distribution of unresolvable anisotropic microstructures revealed in visibility-contrast images using x-ray Talbot interferometry. *Physical Review B* **84**, 094106 (2011) (Cited on page 77).
- [Zanette, 2010] Zanette, I., Weitkamp, T., Donath, T., Rutishauser, S. & David, C. Two-Dimensional X-Ray Grating Interferometer. *Physical Review Letters* **105**, 248102 (2010) (Cited on page 70).
- [Žižak, 2000] Žižak, I. *et al.* Investigation of bone and cartilage by synchrotron scanning-SAXS and -WAXD with micrometer spatial resolution. *Journal of Applied Crystallography* **33**, 820–823 (2000) (Cited on pages 1, 31).

List of Figures

2.1	X-rays in the electromagnetic spectrum.	5
2.2	The different interactions of X-rays with electrons.	6
2.3	Thomson scattering of X-rays by a single electron.	7
2.4	Scattering and momentum transfer vector	9
2.5	Small-angle approximation	11
2.6	Spatial coherence	12
2.7	X-ray refraction	14
2.8	X-ray tube	16
2.9	Undulator at a synchrotron	17
3.1	X-ray projection	19
3.2	Filtered backprojection	20
3.3	Iterative reconstruction	22
3.4	Sample rotation in two dimensions	23
3.5	Sample rotation in three dimensions using Euler angles	25
4.1	Small-angle X-ray scattering experiment	27
4.2	Local differential cross section	29
4.3	Scanning small-angle X-ray scattering	31
4.4	Anisotropic scattering intensity distribution	32
4.5	3-D scanning SAXS	33
4.6	Sketch of a SAXS-CT experiment	34
4.7	Scattering vectors probed with SAXS-CT	35
4.8	Rotational invariance of the scattering signal	36
4.9	Attenuation in scattering experiments	38
5.1	Experimental setup for 6-D SAXS-CT	42
5.2	Effect of an additional axis of rotation	43
5.3	Tooth sample	44
5.4	Micro-CT slice of the tooth sample	45
5.5	Sample orientations measured for 6-D SAXS-CT	46
5.6	Raw PILATUS 2M image	48
5.7	Azimuthal integration	49
5.8	Combination of data from opposing \mathbf{q} -vectors	50
5.9	Determination of beam intensity	51

List of Figures

5.10	Rotational invariance for conventional SAXS-CT	53
5.11	Concept of virtual tomography axes	55
5.12	Data selection for virtual tomography axes	56
5.13	Quantification of rotational invariance for virtual tomography axes	58
5.14	HEALpix pixelation schemes	59
5.15	Consistency between reconstructed and measured data	61
5.16	Virtual extraction of SAXS patterns	62
5.17	Extraction of collagen fibre orientation	63
5.18	Radial plot of cross sections	64
5.19	Three dimensional visualization of collagen fibre orientation	65
6.1	Laboratory Talbot-Lau interferometer	70
6.2	Electron microscopy image of a grating	71
6.3	Talbot effect	72
6.4	Phase-stepping technique	73
6.5	Lau-effect	74
6.6	The three imaging signals of a grating interferometer	75
6.7	Scattering angle in a grating interferometer	78
6.8	Effect of scattering on the modulation curve of a grating interferometer	79
6.9	Relevant \mathbf{q} -vectors for scattering in a grating interferometer	80
6.10	The correlation term of the dark-field signal	82
6.11	The correlation term as a line integral	83
7.1	The correlation integral during computed tomography	86
7.2	Comparison of horizontal and vertical grating alignment	88
7.3	Experimental realization of non-iterative directional dark-field tomography	89
7.4	Sample mounting for non-iterative directional dark-field tomography	90
7.5	3-D renderings of dark-field reconstructions with different sensitivity directions.	91
7.6	Comparison of FBP-based anisotropic dark-field CT with XTT	93
7.7	Visualization of the fibre orientation inside the "TUM" sample	95
8.1	Influence of reconstructed orientations in XTT	99
8.2	Real valued spherical harmonics of even degree	100
8.3	Eulerian Cradle	102
8.4	Improved Acquisition Schemes	103
8.5	Comparison of different grating sensitivity directions	104
8.6	Comparison of conventional and low-sensitivity grating setup	107
8.7	AXDT reconstruction of wooden sample	109
8.8	AXDT and micro-CT reconstructions of freeze cast sample	111

List of Tables

4.1	Overview of different SAXS-imaging techniques	39
5.1	Combinations of the measured rotations	47
8.1	Parameters of different grating setups	106

Abbreviations

AXDT	anisotropic X-ray dark-field tomography
CG	conjugate gradient
CT	computed tomography
FBP	filtered back-projection
GBI	grating-based imaging
HEALpix	hierarchical equal area iso latitude pixelation
SART	simultaneous algebraic reconstruction technique
SAXS	small-angle X-ray scattering
SESANS	spin-echo small-angle neutron scattering
TV	total variation
XTT	X-ray tensor tomography

Constants

\AA	10^{-10} m	Ångström
c	$2.998 \times 10^8 \text{ m/s}$	speed of light
h	$4.136 \times 10^{-15} \text{ eV s}$	Planck's constant
r_e	$2.818 \times 10^{-15} \text{ m}$	classical electron radius
σ_e	$0.665 \times 10^{-24} \text{ cm}^2$	Thomson cross section
e	$1.602 \times 10^{-19} \text{ C}$	elementary charge
m_e	$9.109 \times 10^{-31} \text{ kg}$	electron mass
ϵ_0	$8.854 \times 10^{-12} \text{ A s/(V m)}$	electric constant

Publications and scientific presentations

Publications as first author

Schaff, F., Malecki, A., Potdevin, G., Ettl, E., Noël, P. B., Baum, T., Garcia, E. G., Bauer, J. S. & Pfeiffer, F. Correlation of X-Ray Vector Radiography to Bone Micro-Architecture. *Scientific Reports* **4**, 3695 (2014)

Schaff, F., Bech, M., Zaslansky, P., Jud, C., Liebi, M., Guizar-Sicairos, M. & Pfeiffer, F. Six-dimensional real and reciprocal space small-angle X-ray scattering tomography. *Nature* **527**, 353-356 (2015)

Schaff, F., Prade, F., Sharma, Y., Bech, M., & Pfeiffer, F. Non-iterative Directional Dark-field Tomography. *Scientific Reports* **7**, 3307 (2017)

Schaff, F., Bachmann, A., Zens, A., Zaeh, M. F., Pfeiffer, F., Herzen, J. X-ray dark-field computed tomography for the characterization of Friction Stir Welds: a feasibility study. *Materials Characterization* **129C**, 143-148 (2017)

Publications as co-author

Liebl, H., Baum, T., Karampinos, D. C., Patsch, J., Malecki, A., **Schaff, F.**, Ettl, E., Rummeny, E. J., Pfeiffer, F. & Bauer, J. S. Emerging Research on Bone Health Using High-Resolution CT and MRI. *Current Radiology Reports* **2**, 31 (2013)

Malecki, A., Ettl, E., **Schaff, F.**, Potdevin, G., Baum, T., Garcia, E. G., Bauer, J. S. & Pfeiffer, F. Correlation of X-Ray Dark-Field Radiography to Mechanical Sample Properties. *Microscopy and Microanalysis* **20**, 1528-1533 (2014)

Baum, T., Ettl, E., Malecki, A., **Schaff, F.**, Potdevin, G., Gordijenko, O., Garcia, E. G., Burgkart, R., Rummeny, E. J., Noël, P. B., Bauer, J. S. & Pfeiffer, F. X-ray Dark-Field Vector Radiography - A Novel Technique for Osteoporosis Imaging. *Journal of Computer Assisted Tomography* **39**, 286-289 (2015)

Publications and scientific presentations

Eggl, E., Malecki, A., **Schaff, F.**, Potdevin, G., Noël, P. B., Bauer, J. S., Gordijenko, O., Grande García, E., Burgkart, R., Rummeny, E. J., Baum, T. & Pfeiffer, F. Prediction of Vertebral Failure Load by Using X-Ray Vector Radiographic Imaging. *Radiology* **275**, 553-561 (2015)

Vogel, J., **Schaff, F.**, Fehringer, A., Jud, C., Wieczorek, M., Pfeiffer, F. & Lasser, T. Constrained X-ray tensor tomography reconstruction. *Optics Express* **23**, 15134 (2015)

Wolf, J., Sperl, J. I., **Schaff, F.**, Schüttler, M., Yaroshenko, A., Zanette, I., Herzen, J. & Pfeiffer, F. Lens-term- and edge-effect in X-ray grating interferometry. *Biomedical Optics Express* **6**, 4812 (2015)

Jud, C., **Schaff, F.**, Zanette, I., Wolf, J., Fehringer, A. & Pfeiffer, F. Dentinal tubules revealed with X-ray tensor tomography. *Dental Materials* **32**, 1189-1195 (2016)

Sharma, Y., Wieczorek, M., **Schaff, F.**, Seyyedi, S., Prade, F., Pfeiffer, F. & Lasser, T. Six dimensional X-ray Tensor Tomography with a compact laboratory setup. *Applied Physics Letters* **109**, 134102 (2016)

Turunen, M. J., Kaspersen, J. D., Olsson, U., Guizar-Sicairos, M., Bech, M., **Schaff, F.**, Tägil, M., Jurvelin, J. S. & Isaksson, H. Bone mineral crystal size and organization vary across mature rat bone cortex. *Journal of Structural Biology* **195**, 337-344 (2016)

Wieczorek, M., **Schaff, F.**, Pfeiffer, F. & Lasser, T. Anisotropic X-Ray Dark-Field Tomography: A Continuous Model and its Discretization. *Physical Review Letters* **117**, 158101 (2016)

Schüttler, M., Meyer, P., **Schaff, F.**, Yaroshenko, A., Kunka, D., Besser, H., Pfeiffer, F. & Mohr, J. Height control for small periodic structures using x-ray radiography. *Measurement Science and Technology* **27**, 025015 (2016)

Prade, F., **Schaff, F.**, Senck, S., Meyer, P., Mohr, J., Kastner, J., & Pfeiffer, F. Nondestructive characterization of fiber orientation in short fiber reinforced polymer composites with X-ray vector radiography. *NDT & E International* **86**, 65-72 (2017)

Sharma, Y., **Schaff, F.**, Wieczorek, M., Pfeiffer, F. & Lasser, T. Design of Acquisition Schemes and Setup Geometry for Anisotropic X-ray Dark-Field Tomography (AXDT). *Scientific Reports* **7**, 3195 (2017)

Braig, E-M., Birnbacher, L., **Schaff, F.**, Gromann, L., Fingerle, A., Herzen, J., Rummeny, E., Noël, P. B., Pfeiffer, F. & Muenzel, D. Improved Foreign Body Detection with X-ray Dark-Field Radiography. *European Radiology Experimental* **2**, 1 (2018)

Mathavan, N., Turunen, M. J., Guizar-Sicairos, M., Bech, M., **Schaff, F.**, Tgil, M., & Isaksson, H. The compositional and nano-structural basis of fracture healing in healthy and osteoporotic bone. *Scientific Reports* **8**, 1591 (2018)

Oral presentations

X-Ray Tensor Tomography, *X-ray and Neutron Phase Imaging with Gratings (XNPIG)*, Garmisch-Partenkirchen, January 2014

X-Ray Tensor Tomography, *TUM Reconstruction Workshop*, Munich, June 2014

X-Ray Tensor Tomography, *X-ray Microscopy (XRM)*, Melbourne, Australia, October 2014

Recent advances in dark-field tomography, *X-ray and Neutron Phase Imaging with Gratings (XNPIG)*, Bethesda, USA, September 2015

Characterizing the microscale in macroscale objects: Dark-Field Tensor Tomography, *Workshop on X-ray Imaging Applications in Materials Science*, Munich, February 2016

Large-scale nanostructure investigations: Six-dimensional SAXS-CT, *NLSL-II & CFN Users' Meeting*, Upton, USA, May 2016 (invited)

Poster presentations

Large-scale nanostructure investigations: Six-dimensional SAXS-CT, *X-ray Microscopy (XRM)*, Oxford, UK, August 2016

Characterization of Friction Stir Welds with X-ray Dark-Field Computed Tomography, *KNMF User Meeting*, Karlsruhe, February 2017

Acknowledgements

Looking back at the last couple of years, this work certainly would not have been possible without the help of many people.

At first, I would like to express my sincere gratitude to Franz Pfeiffer. Your lecture on Biomedical Physics initially sparked my interest in X-ray imaging during my master's studies, and I am very thankful for providing me with the opportunity, guidance and also freedom to explore this field in your group. It has been a great honour working for you during the last couple of years, in which I have learned a lot from you. Although your schedule is of course very packed, you would always find the time for a meeting when needed.

Thank you Martin Bech and Irene Zanette for introducing me to the life at a synchrotron. I enjoyed the beamtimes we spent together and benefited a great deal from your experience. Furthermore, thank you Martin for providing me with additional insights during the many discussions we had in the past years and co-supervising this thesis.

I was first introduced to laboratory X-ray imaging by Elena Eggl, Guillaume Potdevin and Andreas Malecki. Thank you for providing me with the foundations that I could build on.

It was a pleasure sharing the experimental grating setup and office island with Friedrich Prade. Furthermore, I want to thank Christoph Jud for his valuable help, especially in creating the first user-friendly implementation of our XTT algorithms. I am grateful to Yash Sharma for our countless discussions on dark-field imaging - although perhaps we should not start them on Friday afternoons in our next lives. Your working morales were truly inspiring and supportive.

Thank you to Tobias Lasser and Matthias Wiczorek of the CAMP chair at TUM Informatics for our very close collaboration. Every other week I was looking forward to discussing new developments of the AXDT/XTT reconstruction during our bi-weekly meetings. Being surrounded by physicists most of the time, your non-physicist view on the topic was always very refreshing to see.

Many thanks to Kaye Morgan, who had to experience the drawbacks of being a native English speaker, but never got tired of answering my questions on English writing.

Acknowledgements

Thank you Julia Herzen maintaining excellent connections to other chairs and obtaining many different types of samples.

The productive working environment at the Chair of Biomedical Physics can not be taken for granted. Therefore I would like to thank especially Nelly de Leiris, Brunhilde Vogt and Klaus Achterhold, who were always there throughout the years to help with administrative questions. Additionally, the efforts of the E17 IT-department to provide a working IT-infrastructure are greatly appreciated. In particular, thank you Martin Dierolf for resolving my several IT issues in record time. The projector framework developed and maintained by Andreas Fehringer was immensely helpful for this work, thank you for the effort you put into this project. Thank you also to all my other colleagues at the E17 chair for creating an enjoyable atmosphere during the last couple of years. Many of the people I have shared my office with also helped proofread this thesis.

Our laboratory equipment heavily depends on the excellent gratings and support provided by Joachim Schulz from microworks GmbH, Dr. Jürgen Mohr and their colleagues from the Institute of Microstructure Technology at the Karlsruhe Institute of Technology, for which I am very grateful. Thank you also to Andre Yaroshenko for assisting me with the implementation of the low-sensitivity setup.

Thank you Dr. Marianne Liebi and Dr. Manuel Guizar-Sicairos for providing us with excellent support at the cSAXS beamline during our measurements.

As the focus of this chair is on developing imaging methods, we naturally need objects to take images from. Hence, I am thankful to the many collaborations that provided us with samples and feedback on our results. In particular, thank you Dr. Paul Zaslansky (Charité) for the tooth sample for the SAXS experiment and Dr. Sylvain Deville (CNRS) for the freeze cast sample. Furthermore, thank you to Andreas Bachmann (*iwb* - TUM Mechanical Engineering), and Prof. Johann Kastner (FH Oberösterreich) and his group for providing interesting material science samples, even though no results of them were shown in this thesis. Equally, thanks to Dr. Jan Krischke and Dr. Thomas Baum of the Klinikum Rechts der Isar for the long collaboration on imaging the microstructure in bone.

In this day and age I feel obliged to thank the internet, especially everyone that provides openly accessible services; and Google to find them. The possibility to find existing solutions to every-day problems within minutes allows to focus on the *real* problems.

I would not be writing these lines without the encouragement and support of my family throughout my life. Thank you for this. Lastly, thank you Geerte for your never-ending support and taking care of Lukas when I needed the time to finish this thesis.